Numerical and experimental hemodynamic studies
of stenotic coronary arteries

Violeta Meneses Carvalho

UMinho | 2020

Universidade do Minho
Escola de Engenharia

Violeta Meneses Carvalho

Numerical and experimental hemodynamic studies of stenotic coronary arteries

junho de 2020

Universidade do Minho
Escola de Engenharia

Violeta Meneses Carvalho

Numerical and experimental haemodynamic studies of stenotic coronary arteries

Dissertação de Mestrado
Mestrado Integrado em Engenharia Biomédica
Biomateriais, Reabilitação e Biomecânica

Trabalho efetuado sob a orientação do(a)
Professor Doutora Senhorinha F.C.F Teixeira
Professor Doutor Rui Alberto Lima

junho de 2020

Acknowledgments

In the development of this dissertation, several people contributed in one way or another to its success.

First of all, I would like to thank my supervisors, Professor Senhorinha Teixeira and Professor Rui Lima, whose guidance, help, supervision, effort and knowledge were fundamental to the success of this work. Thank you both, for your motivation, advice and friendship.

To Professor Rui Lima, my sincere and humble thank for his constant support, patience, enthusiasm, and friendship. I am sincerely grateful to have had the opportunity of working with him.

To Professor Senhorinha Teixeira, I would like to express my deepest gratitude for accompanying me, not only in the development of this dissertation, but also during my academic career, since my second year at the University of Minho. I am very grateful for the constant support, time, and attention, personal and professional.

To Doctor Pedro Costa, I gratefully acknowledge the time dispended, motivation and the opportunity to work in partnership with Biofabics. Without the models provided, much of this work would not have been possible.

To professor Helder Puga, I would like to thank his kindness, time and dedication to provide the models by using his own 3D printer.

I also want to thank Doctor Ana Cristina Ferreira, João Silva, Daniela Martins and Doctor Nelson Rodrigues, for welcoming me so well and for all the indispensable and valuable help that they provided me throughout this journey. Especially, Doctor Nelson Rodrigues' help in the implementation of computational models and discussions on numerical topics was indispensable for the accomplishment of this dissertation.

I would like to express my gratitude to my family. In particular, my parents and brother, my godparents and cousins, all the other close relatives, and my boyfriend and his parents for making everything possible and being patient and supportive throughout the work developed.

To all my friends who accompanied me during the university years, of which I keep countless good memories.

To everyone who helped, supported and contributed in some way to the work developed, my greatest thank you.

STATEMENT OF INTEGRITY

I hereby declare having conducted this academic work with integrity. I confirm that I have not used plagiarism or any form of undue use of information or falsification of results along the process leading to its elaboration.

I further declare that I have fully acknowledged the Code of Ethical Conduct of the University of Minho.

Resumo

As doenças cardiovasculares continuam a ser a causa mais frequente de mortalidade em todo o mundo e constituem um grande desafio para a saúde. Entre elas, a doença arterial coronariana causa quase metade das mortes e, portanto, é de enorme interesse entender melhor o seu desenvolvimento e efeitos. Esta doença é caracterizada pelo estreitamento (estenose) das artérias coronárias devido à deposição de placas na parede arterial, um processo patológico conhecido como aterosclerose.

Esta dissertação teve como objetivo estudar a hemodinâmica nas artérias coronárias estenóticas, a fim de obter uma compreensão mais profunda dos efeitos desta patologia no comportamento do fluxo sanguíneo. Para tal, foram realizados estudos numéricos e experimentais, utilizando modelos idealizados. A investigação numérica foi realizada no software Ansys®, através da dinâmica computacional dos fluidos, que aplica o método dos volumes finitos. A abordagem experimental foi realizada utilizando um sistema de microscopia de vídeo de alta velocidade, para visualizar e investigar o fluxo sanguíneo nos biomodelos estenóticos *in vitro*.

Inicialmente, estudou-se a influência da rugosidade nas visualizações do escoamento, e o melhor biomodelo foi o impresso com menor resolução tendo sido, portanto, o selecionado para a realização dos estudos hemodinâmicos. Para comparar esses resultados com dados numéricos, o escoamento foi definido como laminar e estacionário e o fluído foi considerado Newtoniano. Em geral, os resultados numéricos e experimentais foram concordantes, não só na previsão do comportamento do fluxo com aparecimento de zonas de recirculação na zona pós-estenótica, mas também nos perfis de velocidade.

Numa fase posterior, foi aplicada uma condição de entrada pulsátil para comparar o uso de simulações de natureza laminar e turbulenta, usando o modelo SST k-ω. Os resultados obtidos permitiram concluir que a segunda é mais apropriado para simular o fluxo sanguíneo. Posteriormente, foram examinadas as principais diferenças hemodinâmicas, considerando o sangue como fluído Newtoniano e não-Newtoniano (modelo de Carreau). Para estes modelos, as diferenças foram muito pequenas nos perfis de velocidade, mas mais significativas nas tensões de corte na parede medidas, com o modelo Newtoniano a prever valores mais baixos. As restantes simulações foram realizadas usando o modelo de Carreau e um escoamento de entrada transiente, tendo-se observado um aumento dos valores das velocidades e da tensão de corte na parede com o grau de estenose, o que está associado a um maior risco de trombose.

Palavras-chave: Artérias coronárias estenóticas, Biomodelos *in vitro*, CFD, Hemodinâmica, Impressão 3D.

Abstract

Cardiovascular diseases remain the most frequent cause of mortality worldwide and constitute a major healthcare challenge. Among them, coronary artery disease causes nearly half of the deaths and, thus it is of great interest to better understand its development and effects. This disease is characterized by the narrowing (stenosis) of coronary arteries due to plaque deposition at the arterial wall, a pathological process known as atherosclerosis.

This dissertation aimed to study the hemodynamics in stenotic coronary arteries, in order to get a deeper understanding of the effects of this pathology on the blood flow behavior. For this purpose, both numerical and experimental studies were conducted using idealized models. The numerical research was carried out using Ansys® software by means of computational fluid dynamics which applies the finite volume method. The experimental approach was performed using a high-speed video microscopy system, to visualize and investigate the blood flow in the *in vitro* stenotic biomodels.

Initially, the influence of roughness in flow visualizations was studied, and the best biomodel was the one printed with the lowest resolution having been, therefore, the selected to perform the hemodynamic studies. To compare those results with numerical data, the flow was set to be laminar and stationary and the fluid was considered Newtonian. In general, the numerical and experimental results were in good agreement, not only in the prediction of the flow behavior with the appearance of recirculation zones in the post-stenotic section, but also in the velocity profiles.

In a posterior phase, a pulsatile inlet condition was applied to compare the use of laminar and turbulent assumptions, using the SST $k-\omega$ model. The results obtained allowed to conclude that the second one is more appropriate to simulate the blood flow. Subsequently, the main differences in hemodynamics were examined considering blood as a Newtonian and non-Newtonian fluid (Carreau model). For these models, the differences were very slight in terms of velocity fields, but more significant for the wall shear stress measurements, with the Newtonian model predicting lower values. The remaining simulations were performed using the Carreau model and a transient inlet flow, having observed an increase in the velocities and wall shear stress values with the degree of stenosis, which is associated with a greater risk of thrombosis.

Keywords: CFD, Hemodynamics, *In vitro biomodels*, Stenotic coronary arteries, 3D printing.

Table of Contents

List of Figures

List of Tables

List of Abbreviations

ABS	Acrylonitrile Butadiene Styrene
CAD	Coronary Artery Disease
CFD	Computational Fluid Dynamics
CT	Computed Tomography
CVDs	Cardiovascular diseases
DLP	Digital Light Processing
DMLS	Direct Metal Laser Sintering
DMSO	Dimethyl Sulfoxide
EBM	Electron Beam Melting
FDM	Fused Deposition Modeling
FSI	Fluid-Structure Interaction
FVM	Finite Volume Method
LCA	Left Coronary Artery
LMPM	Low Melting Point Metal
LOM	Laminated Object Manufacturing
MJM	Multijet Modeling
PDMS	Polydimethylsiloxane
PIV	Particle Image Velocimetry
PLA	Polylactic Acid
PMMA	Polymethyl Methacrylate
PTV	Particle Tracking Velocimetry
RANS	Reynolds Average Navier-Stokes
RBCs	Red Blood Cells
RCA	Right Coronary Artery
SIMPLE	Semi-Implicit Method for Pressure Linked Equations
SLA	Stereolithography
SLS	Selective Laser Sintering
SST	Shear Stress Transport
STL	Stereolithographic Format

UDF	User Defined Function
UV	Ultraviolet
WBCs	White Blood Cells
WHO	World Health Organization
WSS	Wall Shear Stress

List of Symbols

Symbols:

d	Diameter	m
k	Kinetic energy of turbulence	m^2/s^2
L	Sampling length	µm
n	Power law index	–
p	Static pressure	Pa
Ra	Arithmetic mean roughness	µm
Re	Reynolds number	–
t	Time	s
U	Average velocity	m/s
u	Component of the velocity vector in the x-direction	m/s
$\vec{u}$	Velocity vector	m/s
$\overline{V_m}$	Average velocity	m/s
y	Direction perpendicular to the wall	m
z(x)	Absolute ordinate	µm

Greek symbols:

$\dot{\gamma}$	Shear rate	s^{-1}
μ	Dynamic viscosity	$Pa \cdot s$
μ_0	Viscosity at zero shear rate	$Pa \cdot s$
μ_∞	Viscosity at infinite shear rate	$Pa \cdot s$
ρ	Volumetric mass density	kg/m^3
τ	Shear stress	Pa
ω	Specific dissipation rate of kinetic energy	s^{-1}
ω	Angular frequency	m/s

Chapter 1

Introduction

Cardiovascular diseases (CVDs) are the leading cause of death worldwide, affecting both developed and deprived countries. According to the World Health Organization (WHO) data, an estimated 17.9 million people have died from CVDs in 2016, representing 31% of all global deaths [1]. From these deaths, 85% are due to heart attack and stroke. Moreover, it is expected that by 2030 the number of deaths will increase to 22 million per year [2,3]. Numerous pathologies are contributing to the high mortality rate by CVDs, such as cerebrovascular disease, rheumatic heart disease, hypertensive heart disease, coronary artery disease (CAD), among others. Nevertheless, in this work, the focus will be on CAD since it is the most common type of CVD and the major cause of heart attack [4]. Given its clinical impact, extended knowledge of blood flow in these physiological conditions is essential [5].

The area of fluid mechanics that studies blood flow is known as hemodynamics, in which numerical simulations, in particular Computational Fluid Dynamics (CFD), has played an important role. It has been widely used in the assessment of blood flow behavior in arteries and, consequently, in the development of CVDs, providing insight into the disease condition, disease progression, and therapeutic optimization [6–8]. Additionally, the computational results are particularly important to compare and complement studies *in vitro* or, in some cases, when it is difficult or impossible to perform studies *in vivo*, providing a cost-effective method to simulate realistic fluid flows [9].

Although significant improvements have been made to the application of CFD models to resolve patient-specific geometries, it is important to ensure its accuracy and reliability comparing the numerical results with clinical and experimental data (Figure 1). Understanding flow fields under *in vivo* biological environment is crucial, however, the non-invasive measurement techniques used to obtain that information have technical deficiencies and thus, making them unfeasible for quantitative CFD assessments. In turn, *in vitro* measurements, where higher resolution flow fields are assessable, can be performed to complement the shortcomings of *in vivo* measurements and are, therefore, vital for thorough CFD cross-validations [10]. By combining the knowledge of clinicians, *in vitro* results and the information extracted from accurate CFD computational models, it can be obtained a reliable procedure for medical diagnosis and treatment [11]. For this reason, both areas should be applied in a complementary way to achieve optimal solutions for different requirements.

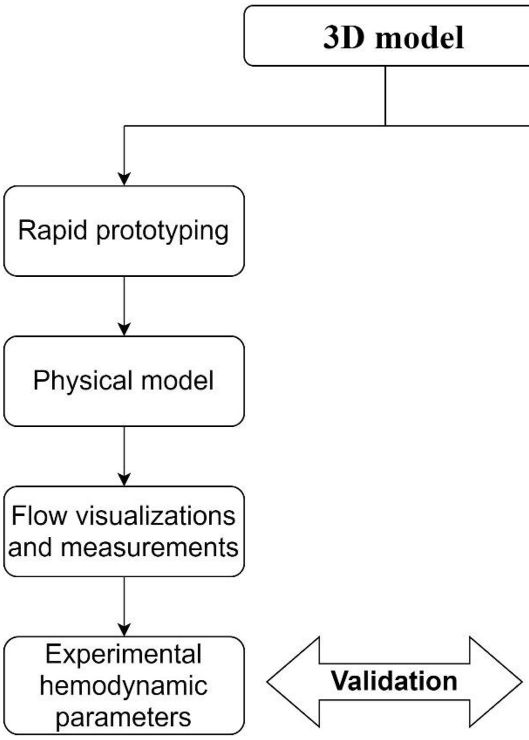

Figure 1. Procedural diagram for experimental and numerical studies.

1.1. Motivation and Objectives

The primary motivation of this dissertation is the prevalence of CVDs, the single largest cause of death worldwide. Despite the great progress achieved in the atherosclerosis research, the nature of the disease is not fully understood. Therefore, the need to understand this disease persists, making it necessary to carry out more hemodynamic studies, both numerically and experimentally. By exploring both methods as a research tool, a wide-ranging understanding of the mechanisms responsible for the pathology's development and progression can be obtained. Moreover, through the characterization of the blood flow, a relationship between the hemodynamic behavior and the occurrence of CVDs, such as atherosclerosis can be established.

The main objectives of the present research are summarized as follows:

- Perform a detailed numerical and experimental study of the blood flow behavior in the presence of stenotic coronary arteries, considering different geometric and physiological parameters.
- Investigate the hemodynamic effect of lumen reduction in coronary arteries, based on idealized models, both numerically and experimentally. Various degrees of stenosis are simulated at coronary arteries to identify their effect on the subsequent hemodynamic changes.

- Compare two different techniques of three-dimensional printing (fused deposition modeling and stereolithography) and evaluate the influence of different printing parameters on the results.
- Investigate the roughness of the printed models and study its influence on the experimental flow visualization tests.

1.2. Dissertation Outline

This dissertation is divided into eleven chapters. In the following, a brief overview of the distinct dissertation chapters is given.

Chapter 1 shows the importance of combining computer simulation and experimental studies, while **Chapter 2** provides a theoretical framework about the cardiovascular system and fluid mechanics principles needed for a better understanding of all the concepts used in the blood flow studies. In **Chapter 3** a review of *in vitro* stenotic arteries to perform blood analogues flow visualizations and measurements is shown. This chapter is currently under review at the Open Journal of Biomedical Engineering. **Chapter 4** describes the experimental techniques and setups used to perform blood flow visualizations, as well as, the image analysis process. In **Chapter 5,** the literature review regarding numerical blood flow studies is presented. This chapter also includes the mathematical modeling of fluid flow, where the CFD fundamentals, the governing equations, the description of the turbulence models, the discretization approaches, and the solution algorithm are addressed.

The case of the present study is described in **Chapter 6**, giving details of its implementation in the computer simulations (geometry dimensions, mesh developed, and boundary conditions applied to solve the problem under study), as well as the printing parameters used to create the physical model.

Chapter 7 - 9 present papers accepted and under review. **Chapter 7** presents the experimental results obtained for the biomodels provided by the company Biofabics. In this study, the influence of roughness on flow visualizations was studied and the models with different constrictions were used to investigate their effect on blood flow by measuring the particles' velocity for each degree of stenosis. This chapter was accepted for presentation in International Conference Innovation in Engineering (ICIE), 2021, Guimarães, Portugal. **Chapter 8** presents a similar study to the previous one, however, combining experimental and numerical results. This chapter is under review for publication in the Micromachines journal. **Chapter 9** exhibits different numerical studies implemented in a new stenotic artery model, also developed in the present work. This chapter studies not only the effect of using turbulence models, but also non-Newtonian models to simulate the blood flow behavior. This chapter was accepted for presentation and publication in the International Conference on Applied Mathematics and Computer Science, 2020, Athens, Greece.

Chapter 10 includes the numerical validation of the results as well as, comparisons of the numerical results in the two different stenotic models used in the present work. The numerical simulation results of the pulsatile nature of the blood flow are also presented and discussed.

Finally, **Chapter 11** indicates the main conclusions of the present dissertation and also some important points to take into account in future research.

Chapter 2

Cardiovascular System and Hemodynamics

This chapter presents important theoretical fundamentals for a better understanding of this work including the cardiovascular system and hemodynamics.

2.1. Cardiovascular System

The cardiovascular system is often associated with the heart, nevertheless, this consists of the heart, blood vessels, and blood, being responsible for providing oxygen and nutrients to the body tissues, as well as the removal of carbon dioxide and waste products via blood. Without its proper functioning, wastes accumulate in tissues and body organs fail to function appropriately [12].

2.1.1. Morphology and Physiology of the Human Heart

The heart, whose anatomy is shown in Figure 2, is one of the most vital organs in the human body, which contracts rhythmically and forcefully to pump blood throughout the body in blood vessels [4,13,14]. It is located in the thoracic cavity between the lungs and its main functions are route blood, generate blood pressure, ensure one-way blood flow, and regulate blood supply [13].

The heart cavity is divided down the middle into a right and a left heart, which in turn are subdivided into two chambers, an atrium, and a ventricle. The atria and ventricles are separated by the interatrial and interventricular septum, respectively [4]. Although it is a single organ, the heart acts as a double pump, with arteries carrying blood away from the heart and veins carrying blood toward the heart.

To prevent the backflow of blood, the heart has different valves, the atrioventricular (AV), and the semilunar valves. The AV valves are located between the right and left atrium and their ventricles. The mitral or bicuspid valve is located between the left atrium and left ventricle and the tricuspid valve is located between the right atrium and the right ventricle. Both valves prevent backflow into the atrium during systole. The semilunar valves (pulmonary and aortic valves) are located at the point where the pulmonary artery and aorta leave the ventricles. The pulmonary valve is located between the right ventricle and the pulmonary artery. While the aortic valve is located between the right ventricle and the pulmonary artery. These valves prevent backflow into the ventricle during diastole [12,15].

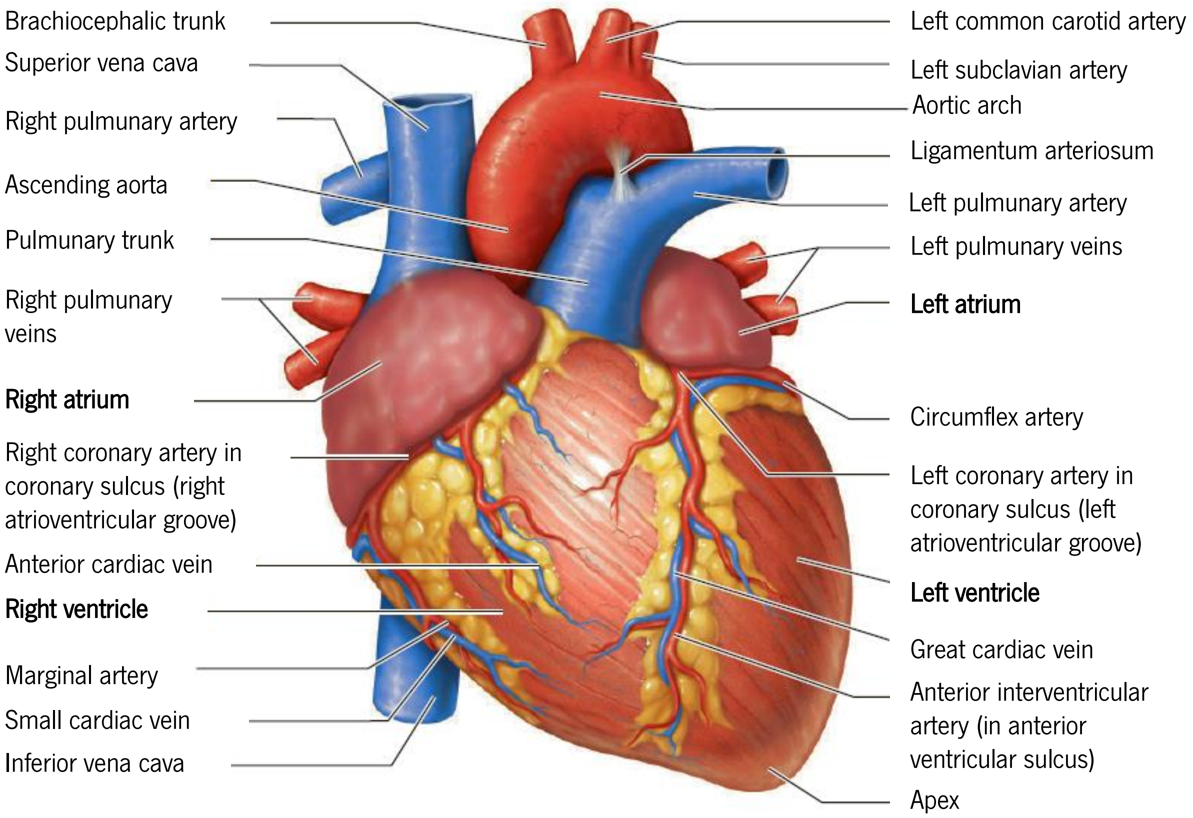

Figure 2. Anterior view of the heart showing major vessels. Adapted from [12].

2.1.2. Blood Flow Through the Heart

The heart and its delivery system have two separate circuits, the pulmonary circuit, which is supplied by the right side of the heart, and the systemic circuit which is supplied by the left side of the heart (Figure 3). In both circuits, the blood is pressurized in the heart and then travels through blood vessels to the capillaries for gas exchanges with cells and, it is then returned to the heart. Another aspect that must be highlighted is that both ventricles contract at the same time, and both atria contract at the same time, even though the blood flow is defined for the right and then the left side of the heart.

The right side of the heart works as the pulmonary circuit pump. In this case, the oxygen-poor blood enters the right atrium through the superior and inferior venae cavae. Then, the blood is pumped out from the right ventricle to the lungs through the pulmonary trunk (right and left pulmonary arteries), where gas exchange occurs, and oxygen is picked up.

The left side of the heart pumps oxygen-rich blood returning from the lungs. The blood enters through the pulmonary veins in the left atrium and is then delivered to the entire body through the aorta artery and back to the right side of the heart. This second phase is known as systemic circulation [4,12,13,15–17].

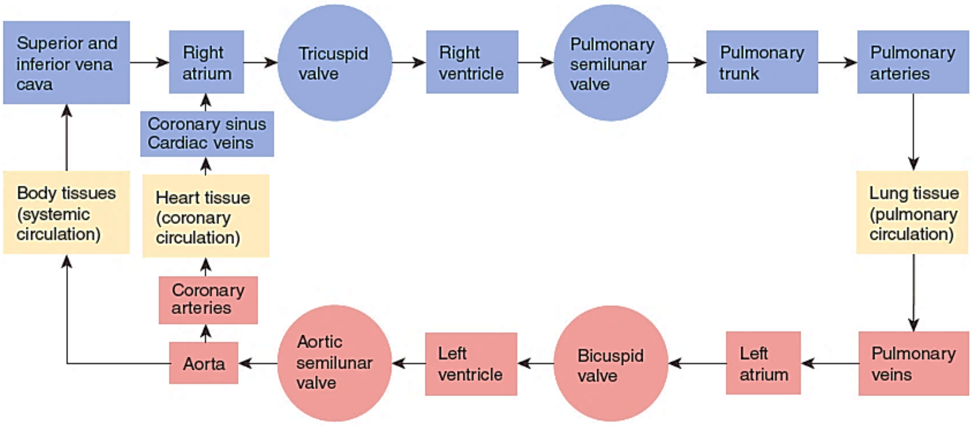

Figure 3. Diagram listing in order the structures through which blood flows in the systemic and pulmonary circulations. The heart valves are indicated by circles, deoxygenated blood by blue and oxygenated blood by red. Adapted from [13].

2.1.3. Cardiac Cycle

The term cardiac cycle refers to the repetitive pumping process that begins with the contraction of the heart muscle and ends with the beginning of the next contraction. This is divided into systole, the period of ventricular contraction, and diastole, the period of ventricular relaxation (Figure 4). Systole is important for generating the pressures necessary for moving blood, while diastole is important to ensure that there is enough relaxation time for the chambers to refill with blood before the next contraction [16,18].

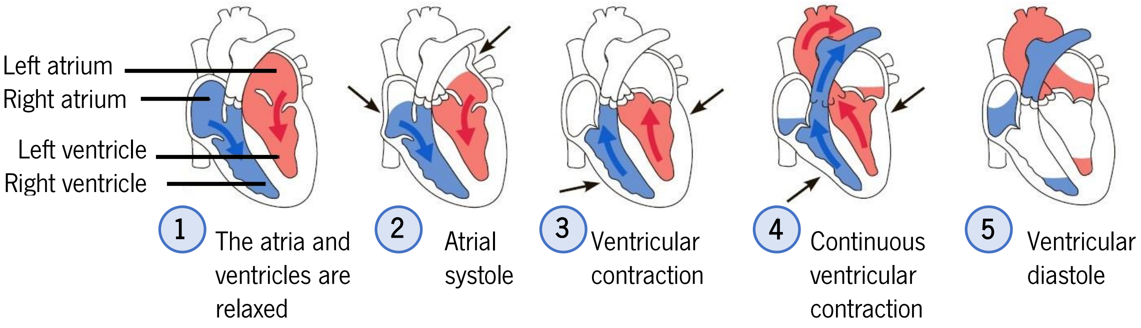

Figure 4. Summary of events occurring during the cardiac cycle. Adapted from [12].

Firstly, both atria and ventricles are relaxed. Blood fills the atria from the body and the lungs, and when the pressure is high enough, the AV valves open and the semilunar valves remain closed. After that, blood begins to passively fill the ventricles to approximately 70% of their volume. Only when atrial contraction (atrial systole) occurs, the last of the atrial blood is emptied into the ventricles completing its filling. Subsequently, the ventricles contract increasing the pressure of the blood within them. Almost instantly, the AV valves close and the pressure in the ventricles continues to increase. This continuous ventricular contraction causes the pressure in the ventricles to exceed the pressure in the pulmonary trunk and aorta. Consequently, the semilunar valves are forced open, and blood is ejected out into the systemic and pulmonary circulations via the aorta and pulmonary artery, respectively. At the onset of ventricular diastole, pressure in the ventricles decreases below the pressure in the pulmonary and aortic trunk and the semilunar valves close, preventing blood backflow into the ventricles. Once this phase is completed, the cycle begins again [13,15,16,18].

2.1.4. Blood Vessels

The blood vessels of the body form a network extremely complex. Essentially, these are divided into five different types: arteries, arterioles, capillaries, venules, and veins. They vary slightly in their structures but share the same general features. Its main function is to carry blood from the heart to the tissues and organs, and vice versa.

Arteries carry oxygenated blood from the heart to all body tissues, except for the pulmonary artery, that carries deoxygenated blood to the lungs. These vessels transport blood to body tissues under high pressure caused by the pumping action of the heart. Because of this, they must have thick, strong, and elastic walls, that can resist the large changes in blood pressure, allowing the efficient transport of blood away from the heart. Notice also that, arteries have smaller lumens than veins, helping pressure maintenance of blood while moving through the system [4].

The wall of an artery consists of three layers, which are the same for veins: the tunica intima (innermost layer), the tunica media (middle layer), and the tunica adventitia (outermost layer) (Figure 5). The first one consists of an inner surface of smooth endothelium covered by a layer of elastic tissues. The second one is thicker, particularly in the large or medium arteries, and consists essentially of smooth muscle cells combined with elastic fibers arranged circularly around the blood vessel. The tunica media in larger vessels is composed primarily of elastic fibers. However, when arteries become smaller the number of elastic fibers reduces, and the number of smooth muscle fibers rises. The third one is the strongest. It is composed of dense connective tissue (collagenous and elastic fibers) and provides a limiting barrier, protecting the vessel from excessive expansion [13,16,18].

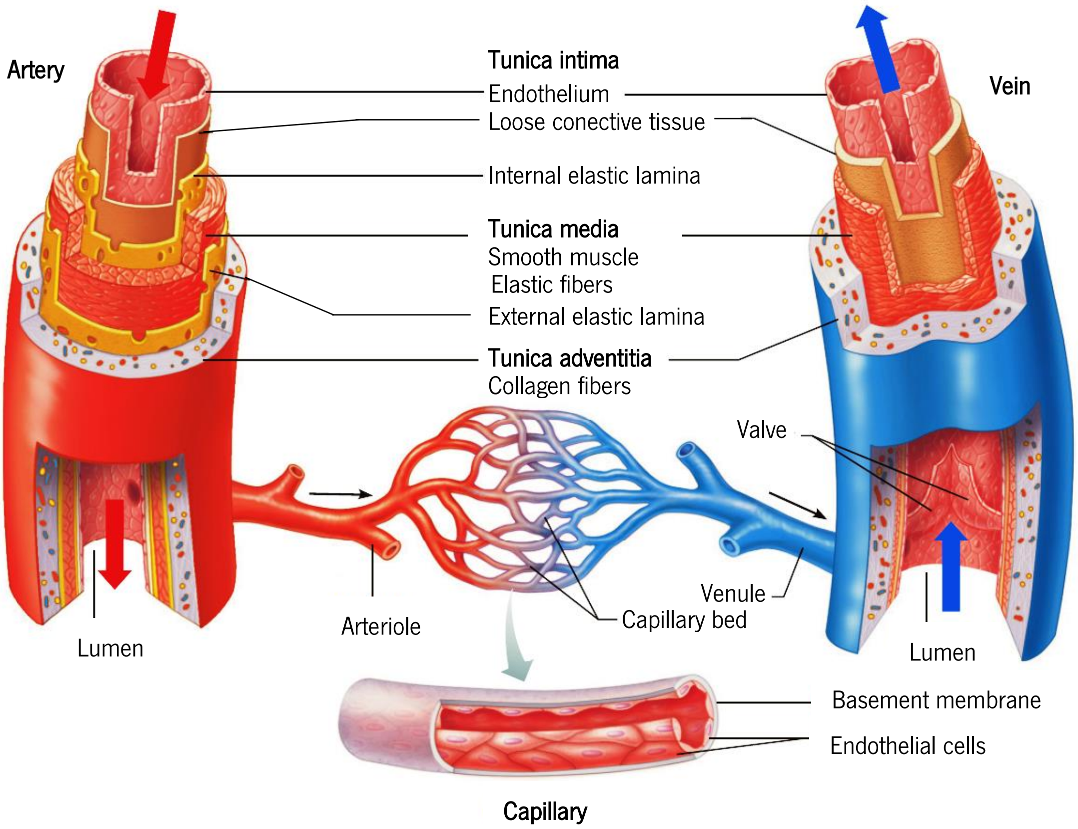

Figure 5. Structure of blood vessels. Adapted from [12].

Arteries are usually classified as elastic arteries, muscle arteries, and arterioles. Elastic arteries have a larger diameter and thicker wall, such as the aorta and pulmonary trunk. These arteries have a larger portion of elastic tissue and a thinner layer of smooth muscle. Moreover, the elastic capacity of these vessels prevents the rapid fall of blood pressure and maintains blood flow while the ventricles are relaxed. Muscle arteries include arteries of medium and small diameter and their wall thickness consists essentially of smooth muscle cells of the tunica media, which allows the regulation of blood flow [13,16,19]. These vessels are responsible for delivering blood to different parts of the body. Arterioles carry blood from the small arteries to the capillary network.

As can be seen, the transition from the artery to arteriole is a gradual process, where a progressive thinning of the vessel wall and a decrease in the size of the lumen occurs. The walls have a greater amount of smooth muscle and less elastic tissue. The arterioles further branch into tiny capillaries where the exchange between the blood and tissues occurs. As the capillaries converge, the formation of small venules starts and they continue to increase their size, starting to exhibit the same wall structure of arteries and later fuse into veins. Compared to arteries, veins have thinner walls, contain less elastic tissue, less smooth muscle cells and the lumens are larger [4,13,16].

2.1.5. Coronary Arteries and its Physiology

The coronary arteries are responsible for the transport of oxygenated blood to the entire heart muscle, so any disorder or disease in these arteries can have serious implications. If the blood flow to a region of the heart is interrupted for a few minutes, the oxygenated blood is unable to be supplied adequately and the ability of the cardiac muscle to function is reduced. Moreover, the portion of the heart muscle supplied by that vessel possibly will be permanently damaged [14].

The typical coronary anatomy (Figure 6) has been thoroughly studied and is described extensively in the literature [16]. Two major coronary arteries branch off from the base of the ascending aorta, just above the aortic semilunar valves. They are called the right coronary artery (RCA) and the left coronary artery (LCA). The RCA provides blood flow to the right side of the heart and continues posteriorly along the atrioventricular sulcus and bifurcates into the posterior interventricular artery and right marginal artery [16]. The LCA supplies much of the anterior wall of the heart and most of the left ventricle and it has three major branches: the left anterior interventricular artery, circumflex artery, and the left marginal artery [13,18,19]. In terms of geometrical appearance, the difference between the LCA and RCA is the fact that the left side has a shorter main stem which quickly branches [20].

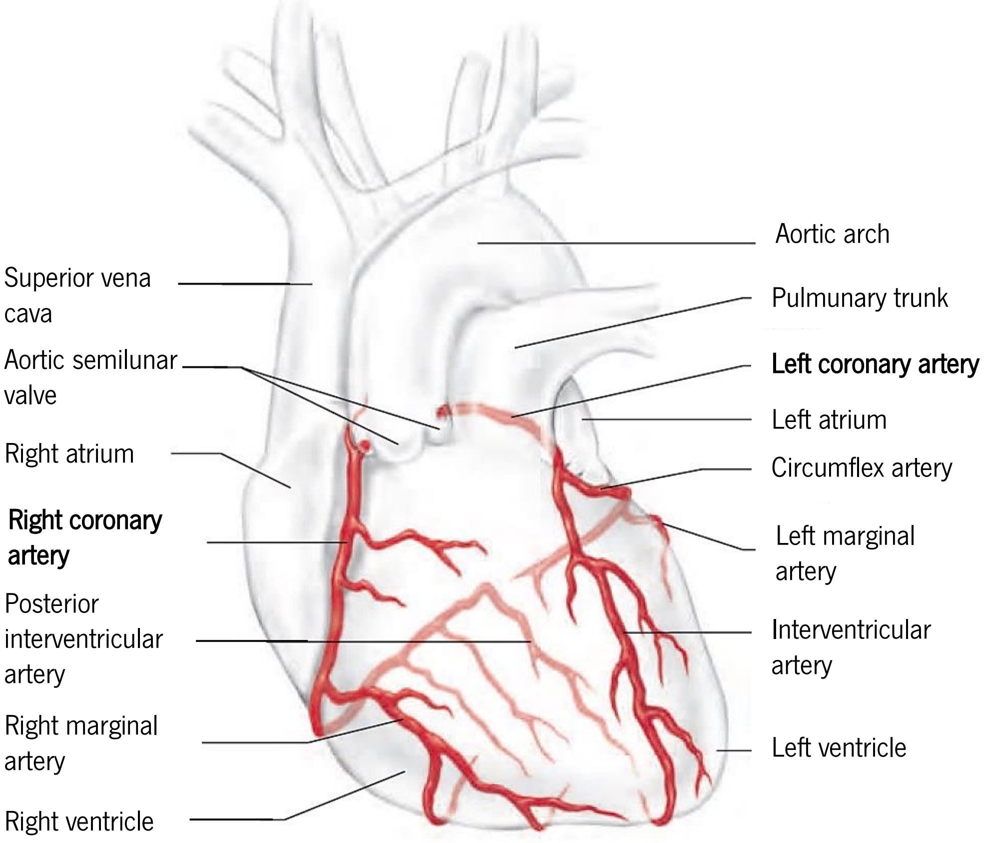

Figure 6. Anatomical structure of the coronary arterial tree. Adapted from [13].

2.1.6. Blood

The human blood is a multiphase complex fluid that carries vital substances to cell tissues and organs of the body and its composition and structure play a vital role in blood rheology. It consists of a concentrated suspension of formed cellular elements (red blood cells – RBCs, white blood cells – WBCs and platelets), which are suspended in plasma [21,22]. The continuous phase of blood, plasma, represents approximately, 55-60% of the blood volume, and the remaining portion (40–45%) are formed elements. However, WBCs and platelets are present in a very low concentration, constituting about 1% of its volume (Figure 7) [23,24]. For this reason, the volume fraction of cells, called the hematocrit, is commonly defined as the red blood cell volume fraction, since RBCs represent 99% of the cell volume [14,25,26].

RBCs are biconcave discs with a mean diameter in the range of 8 μm and a thickness of approximately 2.5 μm and transport oxygen from the lungs to body cells and deliver carbon dioxide from body cells to the lungs. WBCs are principally involved in the immune defense of the body. Platelets are non-nucleated cells that release chemicals to promote blood clotting when blood vessels are damaged [14,24,26].

Despite the complex rheology of the blood being well known, the vast majority of research on hemodynamics assumes that blood behaves as a Newtonian fluid. This assumption is usually reasonable when blood flows in large vessels, such as coronary arteries. However, even in large vessels, non-Newtonian effects may become significant due to the pulsatile nature of the blood flow. This non-Newtonian behavior, also known as shear-thinning, is related to the fact that RBCs can deform and aggregate [27,28].

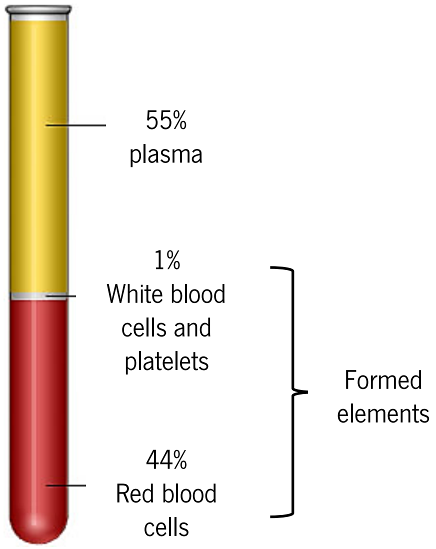

Figure 7. Blood composition. On average, the formed elements make up 45 % and plasma makes up 55 %. Adapted from [13].

2.1.7. Coronary Artery Disease (Atherosclerosis)

CVDs constitute the principal cause of death in the world, and the main underlying disease is known as atherosclerosis. Atherosclerosis is a complex pathological process characterized by the gradual formation of lipid-containing plaques in the innermost layer of the arterial wall, narrowing its lumen (Figure 8 and Figure 9).

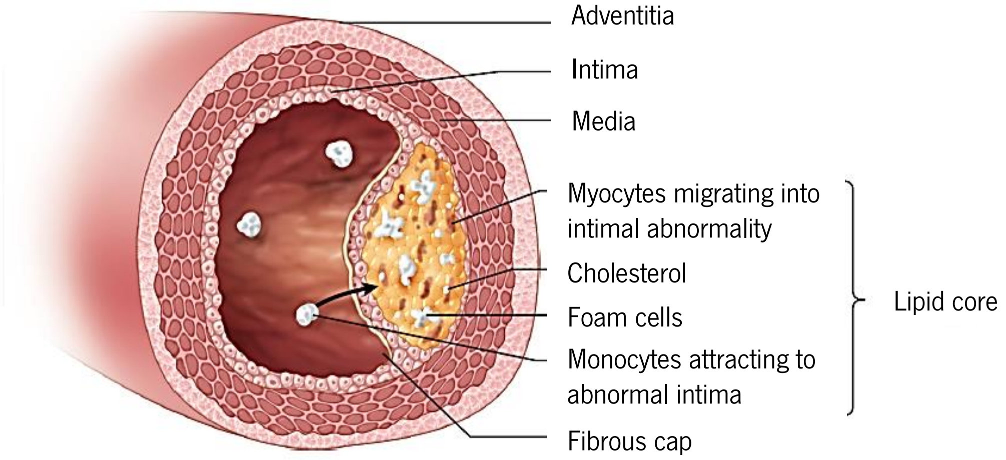

Figure 8. Atherosclerotic plaque components. Adapted from [19].

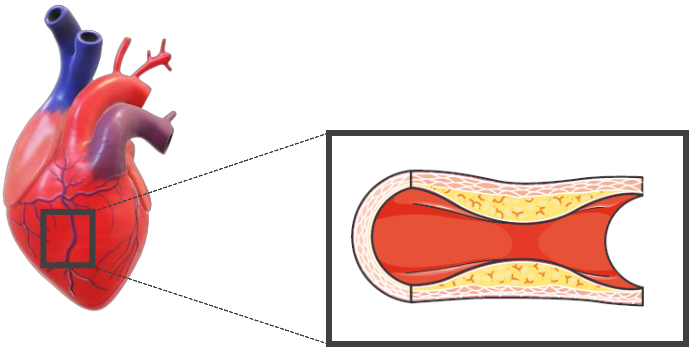

Figure 9. Coronary stenosis representation.

The progressive narrowing of the vessel hinders the normal blood flow, reducing blood supply and, consequently, a lack of oxygen and nutrients are delivered to the heart muscle [29]. As the amount of atherosclerotic plaque increases, blood vessels become stiffened and a greater effort is required from the heart to eject blood in the cardiovascular system [9,30]. The symptoms of the disease, however, will occur only when the extent of the lesions restricts the blood flow to the heart muscle below a critical level (>70% diameter reduction). Cardiac ischemia manifested as chest pain or angina, fatigue, and myocardial infarction are some of the consequences of this illness and, possibly, may cause death [3,4,12,13,18,21,31,32]. Many cases of sudden cardiac death usually result from thrombosis superimposed on a ruptured atherosclerotic plaque [14,33]. Therefore, it is extremely important to physiologically characterize and quantify functional coronary stenosis.

If this happens in a coronary artery, it is called CAD and results in abnormal changes in the coronary artery diameter. This pathology occurs, mainly, due to the presence of a combination of risk factors, such as unhealthy diet, hypertension, diabetes, hyperlipidemia (high levels of cholesterol), smoking, harmful use of alcohol, physical inactivity, and age. Over the years, these factors appear to increase the severity of atherosclerosis and the rate at which it develops [16,34,35].

To diagnose the presence of atherosclerosis, medical practitioners use blood tests, electrocardiograms, stress tests, and techniques that allow visualizing the blood flow through the coronary or other vessels. To treat, patients can receive either pharmacological treatment or coronary revascularization and the choice is based on the stenosis severity and the clinical condition of the patient [36]. In cases of severe atherosclerosis, an effective approach to the treatment of the occlusion injury is to open the coronary blood vessels using a procedure called coronary angioplasty and stent placement, and blood flow is restored [37,38]. If these treatments fail to increase blood flow to the heart muscle adequately, a coronary artery bypass graft can be applied. This is a surgical procedure that involves taking a blood vessel from another part of the body and attaching it to the coronary artery above and below the narrowed area or blockage. Bypass surgery has become safer and it is successful at improving heart function and reducing angina in most people. Nevertheless, it should be noted that neither stents nor coronary artery bypass surgery treat atherosclerosis [16]. This means that even after a successful intervention, it can be developed a re-stenosis or new obstructions elsewhere.

2.2. Hemodynamics

The study of hemodynamics or blood dynamics has captured scientists' attention for thousands of years and it is concerned with the distribution of pressures and flows in the circulatory system [39]. For this purpose, it is of great importance to understand the mechanical forces involved and define some important fluid properties.

2.2.1. Mechanical Forces Exerted by Blood Flow

Due to the cyclical nature of the heart's pumping, arterial blood flow is pulsatile and transient. In Figure 10, three types of hemodynamic forces generated by the pulsatile blood flow through the arterial vasculature are shown: wall shear stress (WSS), a tangential frictional drag force acting on the endothelial cell surface as a result of blood flow [40]; transmural pressure, a perpendicular cyclic force due to blood pressure; mechanical stretch, a cyclic tensile stress of pulsatile flow [41,42]. Among these hemodynamic forces, it has been reported that the pathogenesis of atherosclerosis has a strong correlation with WSS and its influence has been extensively investigated and well understood [11,43–46]. Over the last years, various studies have shown that atherosclerosis lesions tend to be localized in regions of low and oscillatory WSS all over the arterial tree [11,43–47]. On the other hand, the plaque rupture can occur due to high WSS as it causes high flow changes in the vessel [22]. Despite the systemic nature of this disease is associated with risk factors and WSS, it is also a geometrically focal disease that has a propensity to involve well-recognized arterial regions of curvature, bifurcated area and vessel branches [20,40].

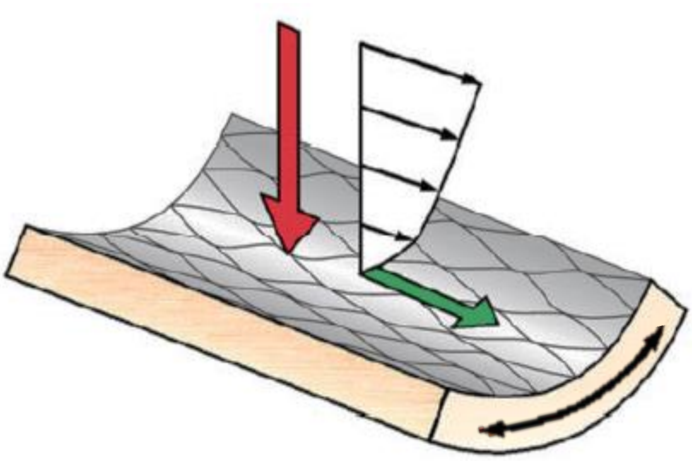

Figure 10. A schematic representation of the forces the vessel wall is exposed to. The red arrow is the normal force component, associated with blood pressure, the green arrow is the tangential component force, associated with wall shear stress and the black arrow is the mechanical stretch. Note that the size of the arrows does not represent the magnitude of the forces, only the direction. Adapted from [41,42].

2.2.2. Blood Viscosity

A fluid is defined as a substance that moves and deforms continuously as long as a shear stress is applied and its viscosity is defined as the internal resistance of a fluid to deform under shear loading conditions [26,48]. This property relates the shear stress to the velocity gradient $\left(\frac{\partial u}{\partial y}\right)$ between adjacent layers of the fluid, where u is the component of the velocity vector in the x-direction and y is the direction perpendicular to the wall. For a Newtonian fluid, the applied shear stress (τ) is proportional to the resulting shear rate $\dot{\gamma}$, being the viscosity (μ) the constant of proportionality. In accordance with Newton's law of viscosity this relation is defined mathematically by Equation 1.

$$\tau = \mu \frac{\partial u}{\partial y} = \mu \dot{\gamma} \tag{1}$$

When the relation between shear stress and shear rate is non-linear, the fluids are called non-Newtonian, and its viscosity is also a function of the shear rate (Equation 2 and Figure 11).

$$\tau = \mu\,(\dot{\gamma})\dot{\gamma} \tag{2}$$

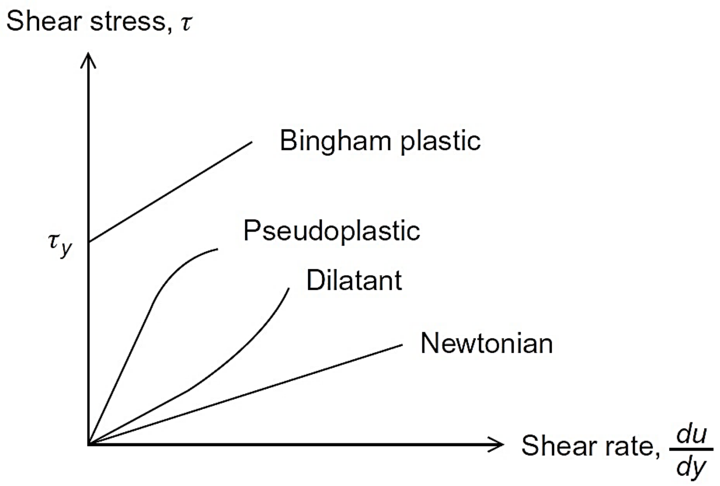

Figure 11. Relationship between shear stress and shear rate. Adapted from [26].

As already mentioned, blood is a non-Newtonian fluid and its viscosity depends on the shear stress applied, which diminishes as the shear rate is increased. This shear-thinning property (also termed "pseudoplastic") is intimately related to the dynamics of RBCs. At very low shear rates, the suspended cells tend to form aggregates (rouleaux), and the apparent blood viscosity increases. By increasing the shear rate, this aggregation decreases, and the apparent viscosity of blood reduces to a limit of approximately 3.5 $mPa \cdot s$ [9,26,49].

The size of the blood vessels also influences blood viscosity. The viscosity decreases progressively with the reduction of vessel diameter [49,50]. This effect is also known as the Fähraeus-Lindqvist effect, which describes how the viscosity of the blood changes with the vessel diameter [51]. Typically, its occurrence is observed at blood vessels smaller than 0.3 mm in diameter. In medium and large arteries, the shear rates are higher than 100 s^{-1} and the blood viscosity is almost constant [49]. For this reason, blood is usually assumed as a Newtonian fluid in simulations of blood flow, which is an accurate approximation at large Reynolds numbers and in large and medium blood vessels. However, in transient studies, there are periods where the shear rate is below 100 s^{-1} and non-Newtonian effects can become remarkably important [52].

There are several mathematical models to describe the behavior of viscous non-Newtonian fluids, such as Power-law, Carreau, Casson, Carreau-Yasuda, Generalized Power-law, among others. However, according to the results obtained by Razavi et al. [53], the Carreau model is a suitable model to represent the non-Newtonian behavior of blood and it has been used by various authors [21,35,54,55].

In the Carreau model, the viscosity is described by Equation 3:

$$\mu = \mu_{\infty} + (\mu_0 - \mu_{\infty})[1 + \lambda\dot{\gamma}^2]^{\frac{n-1}{2}} \tag{3}$$

where μ is the viscosity, μ_0 is the viscosity at zero shear rate, μ_{∞} is the viscosity at an infinite shear rate, λ is the relaxation time, n is the power-law index and $\dot{\gamma}$ is the shear rate [56]. For values of n less than one, the fluid behaves as a pseudoplastic fluid, that have a lower apparent viscosity at higher shear rates. For n equal to one, the fluid is Newtonian. For n values greater than one, the fluid behaves as dilatant (shear-thickening), and its viscosity increases with increasing the shear rates [52]. Besides that, it can be seen that the previous model is valid over the complete range of shear rates, incorporating the values of viscosity at zero shear and infinite shear rate into the formulation.

2.2.3. Reynolds Number

Flow rate is a quantitative value indicating the volume of blood passing through a vessel per unit of time. The qualitative description of the blood flow consists of identifying the flow as laminar or turbulent. The Reynolds number (Re) is the dimensionless number that allows to establish the flow regime and represents the ratio between inertial and viscous forces on an element of fluid. This can be calculated through Equation 4,

$$\mathrm{Re} = \frac{\text{inertial forces}}{\text{viscous forces}} = \frac{\rho U d}{\mu} \tag{4}$$

where ρ is the density of the fluid, U is the average velocity, d is the vessel diameter, and μ is the dynamic viscosity of the fluid.

Physically the inertial forces can be regarded as the ability of the fluid to move and deform freely, while the viscosity acts to hold the fluid together, resisting to any deformation. For lower Reynolds values (Re < 2100), viscous forces are predominant, and the flow is described as laminar. Whereas, for high Reynolds numbers, (Re > 2100), the inertial forces are sufficiently large to amplify the disturbances, and a transition to turbulence occurs. In the transition region (2100 <Re < 4200), the flow can oscillate chaotically between laminar and turbulent. When Re > 4200, the flow is fully turbulent [9,26,42,57].

Laminar flow is described by a parabolic velocity profile which means that the velocity is maximum in the center of the vessel and decreases in the wall direction. All elements of the fluid move in streamlines that are parallel to the axis of the tube. The turbulent flow takes place every time the blood velocity is too high. The elements of the fluid move irregularly with a random behavior and the flow is often described as chaotic with vortices developing [26,49]. Figure 12 represents the developed profiles of these two types of flow. Under normal blood flow conditions, it is unusual the blood has a turbulent flow, however, at highly stenotic vessels is observed the transition from laminar to turbulent flow (Figure 13).

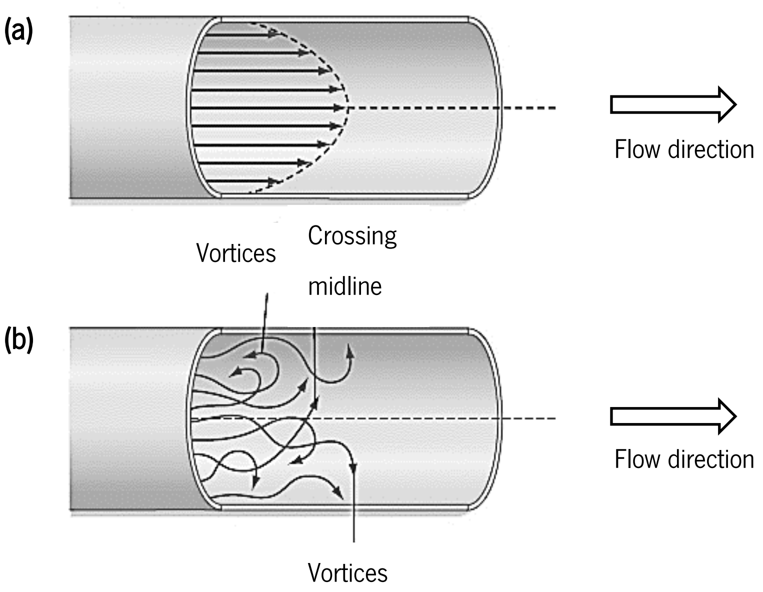

Figure 12. Velocity profiles for (a) laminar and (b) turbulent flow. Adapted from [49].

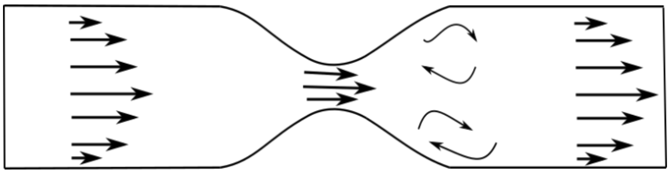

Figure 13. Blood flow behavior along an artery with a severe degree of stenosis.

2.2.4. Coronary Flow

In a previous section, the cardiac cycle was explained and it consists of two periods, systole and diastole. Nevertheless, since the coronary circulation irrigates the heart, during systole the coronary arteries are compressed by the contraction of the myocardium, hindering blood to circulate. Therefore, most of the coronary flow occurs during diastole, where the flow increases. Note that this is the opposite of all other vascular routes in the body. Looking at Figure 14, it can be seen that most of the blood flow to the myocardium occurs during diastole and it is found to decrease during systole. During systole, the microvasculature compresses within the ventricular wall, increasing resistance and, consequently, decreasing flow. In diastole, the ventricle begins to relax, and the compressive forces are removed, allowing the blood flow to increase, reaching a peak, which then falls passively. This happens as the aortic pressure falls toward its diastolic value. Hence, it is the aortic pressure during diastole, which is most crucial for perfusing the coronary arteries. This explains why the heart rate increase can reduce coronary perfusion. At high heart rates, the length of diastole is greatly reduced, which reduces the time for coronary perfusion. This is a problem if the coronary arteries are diseased and are not able to dilate sufficiently, leading to myocardial ischemia and anginal pain [17,18].

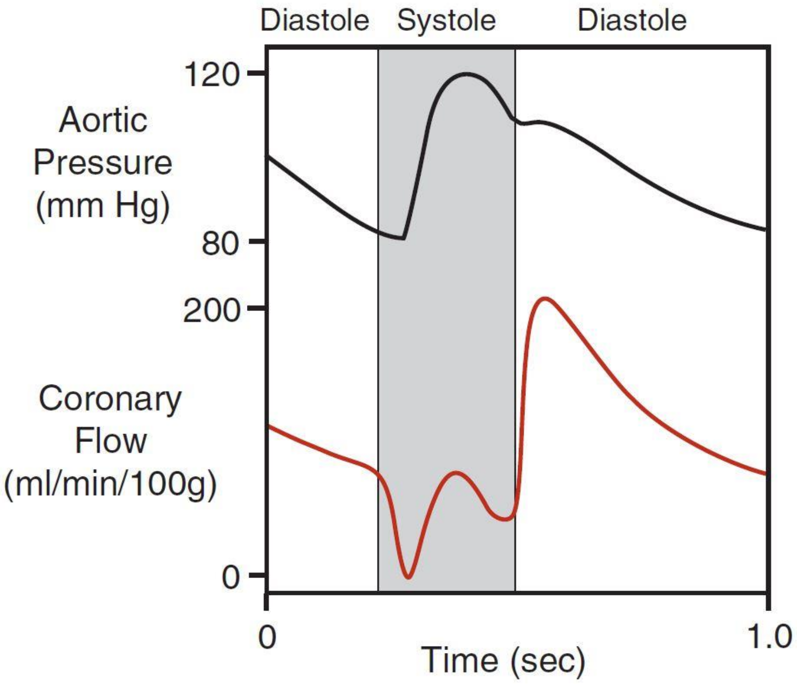

Figure 14. Pulsatile nature of coronary blood flow measured in coronary arteries. Adapted from [17,35]

Chapter 3

In vitro Stenotic Arteries to Perform Blood Analogues Flow Visualizations and Measurements: a Review [1]

Abstract

Cardiovascular diseases are one of the leading causes of death globally and the most common subjacent pathological process is atherosclerosis. Over the years, these cardiovascular complications have been extensively studied by applying *in vivo*, *in vitro,* and numerical methods. *In vivo* studies represent more accurately the physiological conditions and provide the most realistic data. Nevertheless, these approaches are expensive, and it is complex to control several physiological variables. Hence, the continuous effort to find reliable alternative methods has been growing. In the last decades, numerical simulations, in particular Computational Fluid Dynamics, have been widely used to assess the blood flow behavior in arteries and, consequently, providing insights into the cardiovascular disease condition, its progression, and therapeutic optimization. However, it is necessary to ensure its accuracy and reliability by comparing the numerical simulations with clinical and experimental data. For this reason, with the progress of the *in vitro* flow measurement techniques and rapid prototyping, experimental investigation of hemodynamics has gained widespread attention. The present work reviews the state-of-the-art of *in vitro* macro-scale arterial stenotic phantoms for flow measurements, summarizing the different fabrication methods, blood analogues and highlighting advantages and limitations of the most used techniques.

Keywords: cardiovascular diseases, *in vitro*, flow measurement, rapid prototyping, hemodynamics, stenosis, blood flow, blood analogues.

3.1. Introduction

Cardiovascular diseases (CVDs) are the most common reason of death worldwide and are considered to be one of the most important references for human health in the world. According to the World Health Organization (WHO) data, 17.9 million people have died from CVDs in 2016, representing 31% of all

---

[1] Carvalho, V. et al. , 2020. *In vitro* stenotic arteries to perform blood analogues flow visualizations and measurements: a Review. Paper under review in The Open Biomedical Engineering Journal.

global deaths [1]. CVDs are usually caused by atherosclerosis, which is a complex pathological process characterized by the gradual formation of lipid-containing plaques in the innermost layer of the arterial wall that narrows its lumen [2,45,58,59]. As the lumen narrowing increases, the blood supply reduces and, consequently, a lack of oxygen and nutrients are delivered to the heart muscle, causing potentially fatal cardiovascular events [2,60].

To understand the pathology process associated with atherosclerosis, many hemodynamic studies have been conducted [10,61–66], either *in vitro*, *in vivo*, *in silico* or *ex vivo* (see Figure 15) with the purpose to obtain detailed pressure and velocity fields of blood flow phenomena.

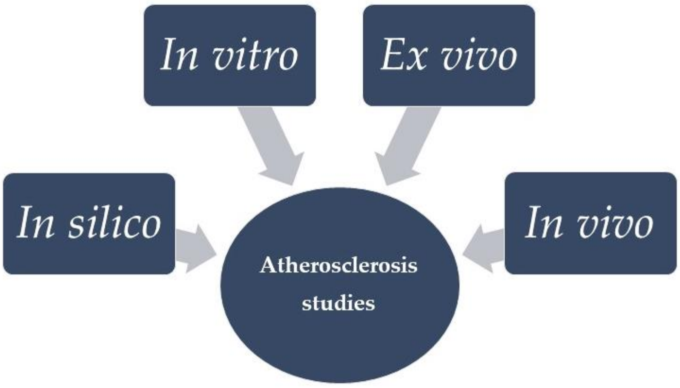

Figure 15. Different approaches performed to study atherosclerosis.

The primary technique used to characterize the flow field in the major blood vessels was performed by Dokunin et al. [67], at mid of 19th century, when the extremities of a known volume airtight U-tube was connected to a blood vessel to measure the rate of arterial blood flow according to the Poiseuille formula. Nowadays, *in vivo* blood flow measurements are acquired through non-invasive techniques that include computed tomography (CT) [68], doppler [66,69,70], ultrasound [71], and phase-contrast magnetic resonance imaging (PC-MRI) [72,73], among others. Despite such measurements having the potential to provide the most realistic flow field data, there are technical difficulties such as long measuring times and lack of spatial resolution to derive velocity gradients and wall shear stresses, which limits the representation of the vessel geometry, blood and tissue properties [10,74,75]. To overcome these limitations, some recent studies have been performed. For instance, Chayer et al. [76] proposed a method to manufacture ultrasonic vascular phantoms that mimic the atheromatous plaque in a carotid artery bifurcation, that can be useful to validate new ultrasound-based imaging technologies. Goudot and his team [77] showed the ability of ultrafast ultrasound imaging to evaluate local flow velocities over an entire 2D image, which has allowed to obtain accurate measurements of WSS, when compared to conventional ultrasound imaging. Although research has progressed to overcome the difficulties of *in vivo* measurements, these methods are still expensive, have low reproductively and require ethical considerations [78,79].

An alternative to those measurements is *in vitro* experiments, which have captured the attention of many researchers and, thus, have been improved over the years. The *in vitro* blood flow has been studied using several techniques including laser doppler anemometry [80], video microscopy and image analysis [81] and particle-based methods such as particle image velocimetry (PIV) [82,83], micro-particle image velocimetry (µPIV) [84], particle tracking velocimetry (PTV) [85] and stereo-PIV [86]. Although these studies do not replicate accurately the complex interactions that occur *in vivo*, they provide a gold standard of experimental control and are an important tool to validate and complement numerical studies.

Another relevant approach are the *ex vivo* studies. These studies bridge the gap between *in vitro* and *in vivo* research, where whole tissue slices are cultured [87,88]. For instance, about two decades ago Santamore et al. [89] have studied the effect of stenosis on arterial vasoconstriction. The authors used portions of the proximal circumflex artery of five dogs. More recently, Karimi et al. [64] have studied human coronary arteries, including both atherosclerotic and healthy, excised within 5 h postmortem.

Moreover, the rapid advances in computer technology, in particular, computational fluid dynamics, has attracted many researchers to investigate in detail several blood flow phenomena in blood vessels, which are difficult to study in detail *in vitro* and *in vivo* [90–92]. Even so, there are still several problems and challenges related to the performance of realistic blood flow modeling [93]. Table 1 summarizes some advantages and disadvantages of these different assumptions.

Despite the large variety of methods to understand the pathology of atherosclerosis, *in vitro* studies provide a valuable and powerful tool. Recent advances in computer-aided design, medical imaging, and 3D printing technologies have provided a rapid and cost-efficient method to generate arterial phantoms. The main aim of this review is to provide a critical evaluation of different 3D printing approaches to manufacture *in vitro* biomodels of stenotic arteries to perform measurements and flow visualizations with techniques frequently used.

Table 1. *Advantages and disadvantages of studies in vivo, in vitro, ex vivo and in silico studies.*

	Advantages	Disadvantages
In vivo	More realistic data; Good to validate new practices and techniques.	Difficult to control variables; Difficult to visualize; Long measuring times; Insufficient resolution; Expensive; Low reproductively; Ethical issues.
In vitro	Easy to control variables; Easy to visualize; Low-cost; Good to validate numerical studies; Reduce the use of animals; Do not have ethical issues.	Difficult to measure some variables (e.g WSS); Do not represent the complexity that happens *in vivo;* Critical to reproduce exact geometry; Difficult to reproduce real wall motion.
Ex vivo	No post-surgical animal care; Maintain the architecture of the tissues closer to the *in vivo* setting; Moderate control of variables; Better visualization compared to *in vivo.*	Short observation time; Difficult to visualize; The age of the models may represent a critical factor; Isolation of the arteries is a critical process; Ethical issues.
In silico	Construction of more realistic virtual models; Reduction of lead times and costs of new designs; Complement experimental and clinical approaches; Ability to simulate biofluid flows that are not reproducible in experiments.	Difficult to define mathematically some physiological parameters; The results are dependent of the accuracy of the mesh performed; Complex simulations can be very long.

3.2. Main Steps Involved in the Fabrication of *In vitro* Biomodels

To perform *in vitro* studies, three major steps must be achieved, which are represented in Figure 16.

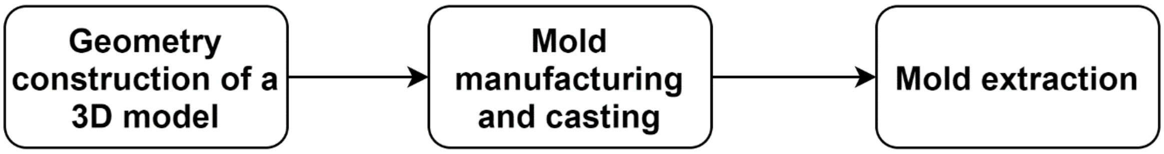

Figure 16. Schematic representation of general steps involved in the fabrication of *in vitro* biomodels.

Firstly, the design of the blood vessel under study is performed and this can be obtained from either patient-specific [10,35,63,78,83,94–96] or idealized geometries [22,62,82,97–103]. The initial research incorporated mostly simpler geometries. Nevertheless, over the years, more realistic studies have been applied to different cardiovascular analyses, including studies conducted in blood vessels [100], aneurysms [104] and stenotic arteries [105,106].

After the geometry construction, a negative mold of the lumen is manufactured. There are many methods for manufacturing, but the most common is rapid prototyping. Rapid prototyping, also named as additive manufacturing (AM), is the latest innovative technology that has revolutionized product design, manufacturing, and biomedical engineering, in the development of *in vitro* biomodels [107,108]. Rapid prototyping, allows the rapid conversion of the information from computerized 3D solid models into physical objects, in a layer-by-layer manner [108–110]. Over the last decades, several rapid prototyping techniques that have involved the processing of materials in solid, powder, or liquid form have been developed [107]. The major rapid prototyping techniques are represented in Figure 17 and include methods such as Stereolithography (SLA), Digital Light Processing (DLP), Multijet Modeling (MJM), Fused Deposition Modeling (FDM), Selective Laser Sintering (SLS), Electron Beam melting (EBM), Direct Metal Laser Sintering (DMLS), Inkjet 3D printing, and Laminated Object Manufacturing (LOM).

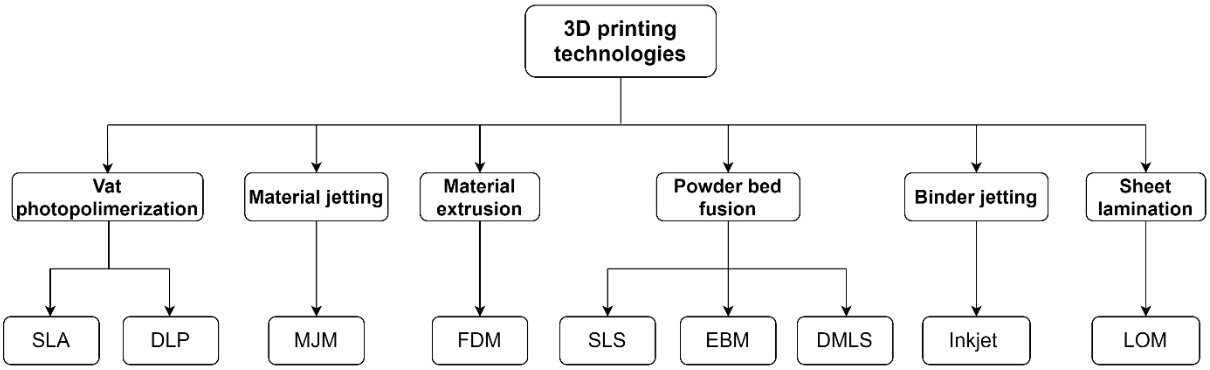

Figure 17. A comprehensive list of different types of printers that are currently in use for several applications.

Despite the numerous types of 3D printers encountered in the market, the SLA, FDM, Inkjet and Multijet techniques are the most commonly used to manufacture artery physical models.

Briefly, in SLA, an object is created layer-by-layer and the polymer resin is cured by photopolymerization using an ultraviolet (UV) laser beam [111]. At each layer, the laser is moved, tracing a pattern and solidifying the resin [109].

In the FDM technique, an object is built by extruding a liquid thermoplastic material from a movable printer nozzle and then deposited layer-by-layer onto a substrate. After extrusion, the thermoplastics solidify almost immediately [109]. For instance, Faria et al. [112] and Hütter et al. [113] made 3D biomodels using FDM printers.

The Inkjet process uses a liquid binding agent and a powder-based material. The print-head selectively drops a fixed quantity of the liquid binding agent. The ejected droplet falls under the action of gravity into the substrate and then dries through solvent evaporation. Then, a piston lowers the powder bed so that a new layer of powder can be spread over the surface of the previous layer. This process is repeated until the 3D structure is finished. In addition, this process can print a variety of materials such as metals, ceramics, and polymers [109,114]. Aycok et al.[115] have used this technology to produce a healthy inferior vena cava, and showed that this technique is suitable to obtain optically transparent internal flow models.

Multijet printing works similarly to traditional inkjet printing, but instead of jetting ink onto powder-based material, a jetting head deposits liquid photopolymer droplets onto a build platform where each droplet cures with a UV light. After building each layer, UV light hardens the layer, and the build platform moves down in the *z*-direction so that the next layer can be printed [108]. Table 2 shows the advantages and disadvantages of these techniques to manufacture arterial phantoms. Additionally, in Table 3 some hemodynamic *in vitro* studies that have used 3D printing technologies to manufacture stenotic phantoms, and the respective geometry, cast material, blood analogues and the analysis method used are presented.

Table 2. Advantages and disadvantages of the most common 3D printing techniques used to produce arterial phantoms.

Methods	Advantages	Disadvantages
SLA	Simple manufacturing process; Fast and good resolution.	Expensive equipment and materials; Only photopolymers.
FDM	Easy to use; Good mechanical properties; Low-cost; Fast.	Materials limited to thermoplastics.
MultiJet	Fast and scalable; Smooth surface finish; Accurate; High resolution.	Poor mechanical properties; Expensive.
Inkjet	Low cost; Easy to use; Reasonably fast.	Low resolution; Low mechanical properties; Expensive replacement ink cartridges.

Table 3. Summary of some experimental *in vitro* studies of hemodynamic using rigid phantoms.

Geometry	RP[2] system	RP material	Cast material	Blood analogue	Measurement method	Authors
Real porcine coronary arteries	Multijet and Inkjet	FullCure®720 and 3Z model	PDMS[3]	W[4]	-	Jewkes et al.[95]
Idealized	Injection molding	Aluminum	Silicone (T-2 silastic)	W- G[5] (40, 60%)	PIV	Brunette et al. [116]
Patient-specific	SLA[6]	-	PDMS	DMSO[7]-W (52, 48 %)	μPIV	Doutel et al.[35]

---

[2] RP – Rapid Prototyping

[3] Polydimethylsiloxane

[4] W-water

[5] G-Glycerol

[6] SLA – Stereolithography

[7] DMSO- Dimethyl sulfoxide

Patient-specific	SLA	PIC100 resin	PDMS	Whole blood	Fluorescence microscopy	Costa et al.[96]
Patient-specific	SLA	Rigid print material (VeroWhitePlus RGD835) and rubber-like material (TangoPlus FLX930	Silicone	DiW[8]- G- corn starch (70, 30, 0.1 %)	Doppler	Maragiannis et al. [117]
Patient-Specific	SLA; Multijet and FDM	Flexible resin, Tango Grey and black resin and TPU filament	-	-	-	Stepniak et al.[118]
Patient-Specific	Inkjet	Low melting point alloy	Silicone	G- SNDS [9]-D[10]-O[11] -Antifungal agent- DM [12](15, 1, 3, 2, 79 %)	Doppler Ultrasound	Malone et al. [119]
Idealized	SLA	Epoxy resin	PDMS	W-G (39, 61%)	µPIV	Doutel et al. [99]
Idealized	FDM	Acrylonitrile butadiene styrene filament (ABS)	PDMS	DiW-G-NaI[13] (47.38, 36.94, 15.68%)	PIV	Choi et al. [61]
Idealized	SLA	Clear resin	PDMS	D	Inverted confocal microscope	Asaad et al. [120]
Patient-specific	Inkjet	Water-soluble plaster	Silicone	W-G (45, 55%)	PIV	Cheung et al.[10]
Patient-specific	SLA	Stereocol Acrylate	RTV[14] Silicone	IA[15]-G (70, 30%)	PIV	Glickman et al.[63]

---

[8] DiW- Distilled water
[9] SND- Synperonic N detergent surfactant
[10] D-Dextran
[11] O-Orgasol particles
[12] DM- Demi water
[13] NaI-Sodium iodide
[14] RTV-Room-Temperature-Vulcanizing
[15] IA-Isopropyl alcohol

Finally, to cast the physical model, a transparent material to the applied wavelength light must be used and its half thickness must be smaller than the focal distance of the used objective lens [121]. Initially, different materials were used, like plastic [122], glass [123,124], latex [125], polymethylmethacrylate (PMMA) [126,127] and Agar-based materials [128]. Despite the diversity of materials mentioned, the most common transparent materials are the polydimethylsiloxane (PDMS), glass and PMMA. However, over time, PDMS became the preferred material of researchers due to its superior properties when compared to the remaining materials [129–131]. Some advantages and disadvantages of PDMS, PMMA, and glass are summarized in Table 4. In turn, Table 5 summarizes the typical mechanical, chemical (solvent and acid/base resistance), and material costs for PDMS and thermoplastics, commonly used in *in vitro* studies.

Although PDMS is the most well-known and most common method, some authors have tried to directly print biomodels without using cast materials, in order to produce compliant phantoms. For instance, Biglino et al. [94] used the polyjet technique to obtain compliant arterial phantoms of patient-specific data. They have concluded that TangoPlus FullCure® is a suitable material for modeling the distensibility of arteries *in vitro* with very representative anatomical finishing and with the ability to represent non-uniform wall thickness. More recently, Stepniak et al. [118] have used several flexible commercially available materials to print 3D stenotic models (Table 3).

Table 4. Advantages and disadvantages of some casting materials used in biomodels.

	Advantages	**Disadvantages**
PDMS	Nontoxicity; Biocompatibility; Simple fabrication process; Good optical transparency; Durability; Elasticity; Capable of sustaining a variety of cell types; Inert.	Can absorb small hydrophobic molecules; Evaporation of water vapor is hard to control; Hydrophobic nature.
PMMA	Economic; Biocompatibility; Ease of processing.	Rigid; Can undergo thermal degradation and thermal oxidative degradation in the presence of oxygen.
Glass	Good optical transparency; Excellent roughness; Inert.	Difficult to reproduce the desired geometry; Rigid.

Table 5. Summary of physical properties for common polymers used in *in vitro* models.

	PDMS	PMMA	Glass
Mechanical properties	Elastomer	Rigid	Rigid
Solvent resistance	Poor	Good	Excellent
Optical transmissivity			
• **Visible range**	Excellent	Excellent	Excellent
• **UV range**	Good	Good	Good
Biocompatibility	Good	Good	Good
Material cost	~135€/ Kg	~1.6-3.6€/Kg	~20-30€/Kg

3.3. *In vitro* Studies in Stenotic Arteries

In the literature, several researchers have been investigating different parameters associated with atherosclerosis, besides the diameter reduction effect. Doutel research group has performed several studies on stenotic coronary arteries. For instance, in one of their studies [99], they have compared two types of casting methods, lost-wax and sucrose, to fabricate *in vitro* models, since the removal process of these materials compromises the optical flow experiments and the credibility of the final results. They have concluded that the lost-sucrose casting method exhibit much better optical characteristics when compared to the lost-wax method. This allows a better flow visualization and the measurement of the velocity fields by using a µPIV (Figure 18 (a)).

In a different perspective, Doutel et al [35] have developed a methodology to create 3D irregular stenosis with different degrees of occlusion in artery models for numerical and *in vitro* hemodynamic studies, identifying areas of low wall shear stress as these locations have more propensity to the development of atherosclerosis (Figure 18 (b)).

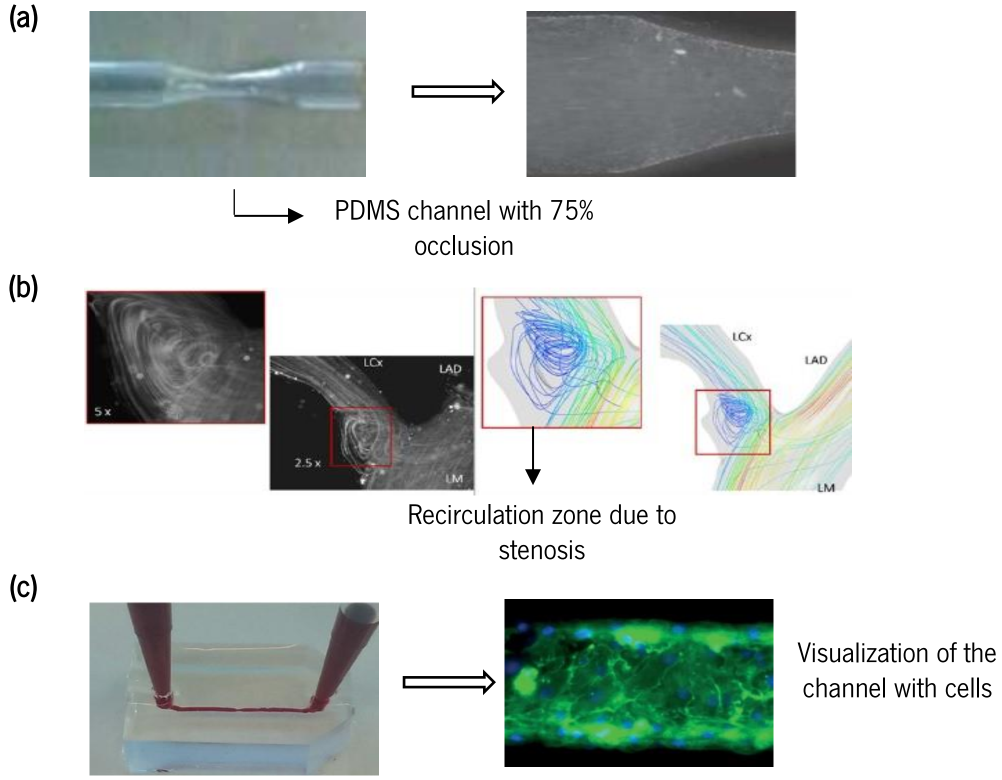

Figure 18. Examples of some phantoms and respective experimental images: (a) Rigid PDMS phantom and flow visualization of a stenotic artery, adapted from [99]; (b) Flow visualization and streamlines obtained numerically of a stenotic left coronary artery, adapted from [35]; (c) PDMS model of a stenotic coronary artery and image obtained by means of fluorescence microscopy, adapted from [96].

In a recent study conducted by Jewkes et al. [95], 3D models of healthy and diseased coronary arteries were fabricated based on a porcine heart and defined based on morphometric measurements. Two different printers were used and compared. Different parameters like layer thickness, anatomical accuracy and time per model, were studied. In their investigation, a hydrostatic system and a pulsatile displacement system setup were applied.

From a different perspective, Helgeson et al. [124] have investigated the transport of particles used to debulking plaques from arterial walls and showed an example of the importance of combining *in silico* and *in vitro* studies. Choi et al [61] have conducted another study, where a comparison of rigid and deformable eccentric stenosis was investigated. A deformable stenosis model was fabricated to mimic a thin fibrous cap and the oily phase of the lipid core part was represented by using the liquid state of the Sylgard 184 base. They have studied the deformation periodically, under a pulsatile flow condition, and the results have revealed the feasibility to detect deformable vulnerable stenosis from the waveform of the pressure drop across the stenosis.

In addition to the previous investigations, interesting studies in stenosed carotid bifurcation arteries have been conducted by Kefayati et al. [102] combining PIV analysis with CFD simulations. Firstly, the researchers have only considered normal and stenosed carotid arteries (50% and 70%) aiming to study transitional flow using a combination of PIV and proper orthogonal decomposition (POD). Then, in another study [132], they have investigated not only the effect of stenosis severity (30%, 50% and 70%) in carotid artery models, but also the plaque eccentricity (concentric or eccentric stenosis) and ulceration, taking into account its influence in the level of turbulence intensity (TI). Considering these last features, in another work [133], the authors have also investigated the levels and patterns of shear stress, derived from both laminar and turbulent phases, in the same models. The combination of these three studies and their results have revealed that beyond stenosis severity, there are other parameters that have the potential to promote clinical implications for a more sensitive assessment of stroke risk. In their studies, the biomodels were manufactured using a lost-core casting technique. A low melting point metal (LMPM) core in the shape of the desired lumen model geometry was cast from an aluminum mold. The core was mounted inside a plastic box and a second material, either plastic resin or agar gel, was then poured into the plastic box around the LMPM core. Once the material surrounding the core had solidified, the LMPM core was melted out. This manufacturing process was also used by other authors like DiCarlo et al. and Poepping et al. [128,134–136].

Griffith et al. [137] have applied a pulsatile inlet flow through a circular tube with an axisymmetric blockage and studied both numerically and experimentally the effect of different degrees of stenosis. They have observed that experimental flows are less stable than the numerical analysis prediction. In another investigation, Yang et al.[138] have studied patient-specific left coronary stenotic arteries. They have performed numerical studies and used 3D printing technologies (SLA) for a comprehensive understanding of the relationship between spatial characteristics and hemodynamics variations. The results have shown that multiple spatial characteristics can potentially improve the non-invasive evaluation of the diseased vessel.

Since atherosclerosis is a complex disease associated with multiple factors, promising studies have emerged [139–142] to understand the process of atherogenesis, thrombus formation and cell interactions in stenotic arteries. In this direction, an interesting study was undertaken by Costa et al. [96]. Combining SLA with real medical images, they have performed both *in vitro* and in silico studies of the flow through healthy and stenotic arteries (Figure 18 (c)). The fabricated channels were lined with endothelial cells and perfused with whole blood.

As can be seen, there are many different types of research, all of them with the same goal to understand the pathology of atherosclerosis. Thus, the research in this field can take many different directions.

3.4. Blood Analogues

The development of blood analog fluids to perform *in vitro* hemodynamic experiments is extremely relevant due to ethical, economical and safety problems related to the use of real blood in those experiments. Hence, several researchers have been focused to the development of new analogues, in order to mimic not only the physical properties but also the flow behavior of the real blood, especially under steady shear conditions [28,143–148]. Some examples of those investigations are presented in Table 3.

Initially, the blood flow studies were performed with Newtonian blood analogues composed of mixtures of glycerol and water [149–154]. In a second stage, non-Newtonian fluids composed by xanthan gum (XG) or/and polyacrylamide (PAA) diluted in glycerin and/or water were developed and applied in different studies [28,155,156].

Pinto et al. [81] have found a noticeable cell-free layer around walls, when performing *in vitro* experiments with blood samples. That is due to the red blood cells (RBCs) migration to the center of the channel leading to the reduction of the effective viscosity [157–162]. This physiological phenomenon does not happen with blood analogues fluids without solid elements, such as microparticles and microcapsules. Consequently, it is crucial to take into account the cellular blood components that exist within the base fluid [81,163–165]. In addition, Lima and co-workers [164,165] have visualized and measured cell-cell interactions. They have shown that the RBCs radial dispersion tends to increase with cell concentration and may influence the blood mass transport mechanisms. Hence, it is important that the hemodynamic flow phenomena that occur at the microscale level also be mimicked by particulate blood analogue fluids. RBCs are able to perform fundamental functions, such as the transport of gases and nutrients, but they also have the ability to deform under shear flow when they pass through a narrower capillary. Several experimental works [146,166–169] have developed blood analogue fluids containing polystyrene and polymethylmethacrylate (PMMA) particles to mimic the key structural attributes of RBCs. Despite the similar size and shape, the mechanical properties, i.e. the stiffness and deformability, were not identical to the real RBCs.

Subsequently, several types of particles with varying stiffness and shapes have been developed and their deformability in narrow channels was investigated [158,166,170–173]. Maruyama et al. [144,174] have developed a blood analogue made of a Newtonian solvent containing a suspension of microcapsules to evaluate the absolute hemolytic properties of centrifugal blood pumps. Later, Nguyen et al. [175] have performed a similar study, but this time using a non-Newtonian solvent. These latter studies present particulate blood analogues that are able to reproduce well the steady viscosity, but they did not study any microscale flow phenomenon. An innovative blood analogue fluid containing giant unilamellar vesicles (GUVs) [176,177] was developed to mimic the flow of RBCs in microchannels. The GUVs were made of a hydrated mixture of soybean lecithin, extruded through polycarbonate membranes, to guarantee the diameter of a uniform vesicle. Merkel et al. [178] have synthesized hydrogel microparticles with tunable elasticity. They also evaluated the behavior of healthy and diseased RBCs and synthetic mimics of RBCs by using microfluidic models of vascular constriction. Vilanova et al. [179] have successfully produced monodisperse silicon droplets to be used as templates for the formation of capsules with potential molecular delivery with controlled release. The mechanical behavior of the generated capsules could be finely tuned by varying the geometrical parameters. Cui et al. [171] have engineered Polyethylen glycol (PEG) hydrogel particles with adjustable elasticity and with a size similar to human RBCs. By using atomic force microscopy and a microfluidic blood capillary model that mimics dimensions and pressure differentials of the *in vivo* environment, they have investigated the deformability behavior of these particles and demonstrated that this behavior could be tuned to be similar to that of RBCs. Choi et al. [180] have developed a simple and fast method to produce micro-sized spherical PDMS particles by mixing uncured PDMS with distilled water.

Pinho et al. [169] and Calejo et al. [146] have developed particulate blood analogues with rigid particles able to show a cell-free layer formation downstream of a microchannel contraction and the reproduction of the viscosity curve of rigid RBCs suspensions. In Figure 19, the comparison between the flow of RBCs and PMMA is illustrated. However, both studies have suggested that the only way to closely mimic some microscale blood-flow phenomena is by using deformable microparticles. Recently, Muñoz-Sánchez et al. [147,181] have proposed a flow-focusing technique to produce micro-sized PDMS flexible spherical particles for biomicrofluidic applications, demonstrating also the ability of the proposed particulate fluid to reproduce the steady shear viscosity curve of ovine RBCs suspended in Dextran 40.

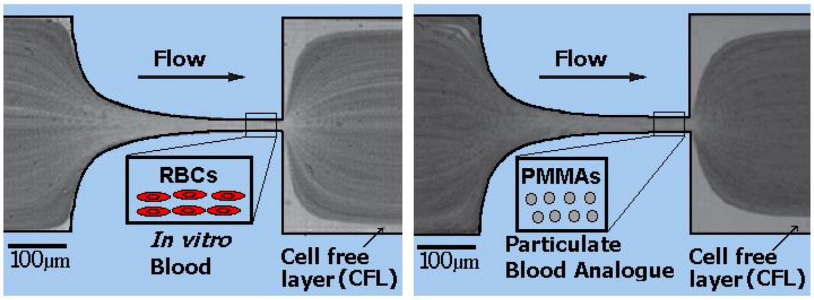

Figure 19. Flow of in vitro blood and a particulate blood analogue (PMMA particles in Dx40) through a hyperbolic contraction (adapted from [146]).

3.5. Conclusions and Future Directions

Atherosclerosis is the primary cause of morbidity and mortality worldwide, having a great negative impact on society around the world. The breakthrough in 3D printing technologies has enabled the production of stenotic arterial phantoms, both idealized and patient-specific, directly from computer-aided-design data. These arterial phantoms are remarkably important due to the ability to validate numerical results and to deeply study atherosclerosis pathology and its effect on hemodynamics. There are several methodologies to produce and perform *in vitro* experiments, making it extremely complex to suggest which is the optimal process. Moreover, there are some drawbacks, limiting the applicability of the outcomes for clinical practice. For instance, assumptions regarding flow behavior, stiffness of the wall, simplified blood analogues and inaccurate vessel geometries, are properties that can affect the clinical value of many findings.

This paper provides a review of various *in vitro* studies focusing on stenotic artery phantoms. In addition, it shows different 3D printing techniques in the construction of stenotic phantoms and the variety and importance of blood analogues selection. The most cost-effective techniques currently used are the laser type, SLA, the jetting type and FDM. The most common material used to perform *in vitro* flow studies is PDMS, not only due to its low-cost, biocompatibility and optical transparency but also due to its elasticity. The most reported measuring techniques were PIV and μPIV. These techniques lead to the generation of accurate flow velocity profiles. Also, while the other techniques measure the velocity at a point, PIV measurements produce two-dimensional or even three-dimensional vector fields. Different types of blood analogues were developed over time. Most of the fluids are water-based or they were made with a mixture of water and glycerin or glycerol. Some of the fluids have the ability to replicate the non-Newtonian behavior of the blood while others have semi-rigid particles to simulate the behavior of the RBCs.

This review also shows that the current state of the art in stenotic arteries is capable of interpreting and mimicking hemodynamic dysfunction and it can be used to optimize the existing treatments and to enhance the medical management of the atherosclerotic disease. Investigation in fluid mechanics has a relevant contribution to the design of interventional diagnostic, measuring and treatment devices. Further research is needed to better understand the physiological phenomena that occur in pathological conditions. For instance, the properties of atherosclerotic plaque are most likely to be very heterogeneous, anisotropic and non-linear.

3.6. Acknowledgements

This work has been supported by FCT – Fundação para a Ciência e Tecnologia within the R&D Units Project Scope: UIDB/00319/2020, UIDB/04077/2020, and NORTE-01-0145-FEDER-030171, funded by COMPETE2020, NORTE 2020, PORTUGAL 2020 and FEDER. This project has received funding from the European Union’s Horizon 2020 research and innovation programme under the Marie Sklodowska-Curie grant agreement No 798014. This project has received funding from the European Union’s Horizon 2020 research and innovation programme under grant agreement No 828835.

Chapter 4

Channels Fabrication and Experimental Procedures

This chapter describes the fabrication techniques used to manufacture the artery channels, as well as some fundamental principles of the experimental setup applied during the experimental tests and data processing.

4.1. Additive Manufacturing Techniques

3D printing, also known as AM or rapid prototyping, is the latest breakthrough technology that has revolutionized many areas of engineering, including biomedical engineering. This technique allows the rapid conversion of 3D digital model information into physical objects. The biggest advantage of this technology is its compatibility with a wide range of polymeric materials, as well as possible compounds and process efficiency [108,182,183].

There are different printer types such as Selective Laser Sintering, Inkjet 3D printing, Multijet Modeling, Electron Beam Melting, Laminated Object Manufacturing, FDM, and SLA [108]. However, in this study, only the SLA and FDM techniques were applied, which have been frequently used to manufacture physical models of stenotic arteries or aneurysms.

4.1.1. Fused Deposition Modeling (FDM)

Also known as fused filament fabrication, this technology uses a thermoplastic filament, which is continuously deposited on an extrusion nozzle heated above the melting temperature of the material. Then, it is extruded and deposited layer by layer on a build plate.

The deposited layers solidify and bond permanently with the adjacent layers. During the process, as the melted material is deposited, the needle moves in the x-y horizontal plane and it hardens promptly. When each layer in the x-y plane is completed, the build plate is moved down in the z-direction to allow the next layer to be constructed. This procedure is repeated until the whole part is obtained (Figure 20). To improve interlayer bonding, the whole process is performed in a closed chamber that maintains the temperature constant [6,108,182,184–186].

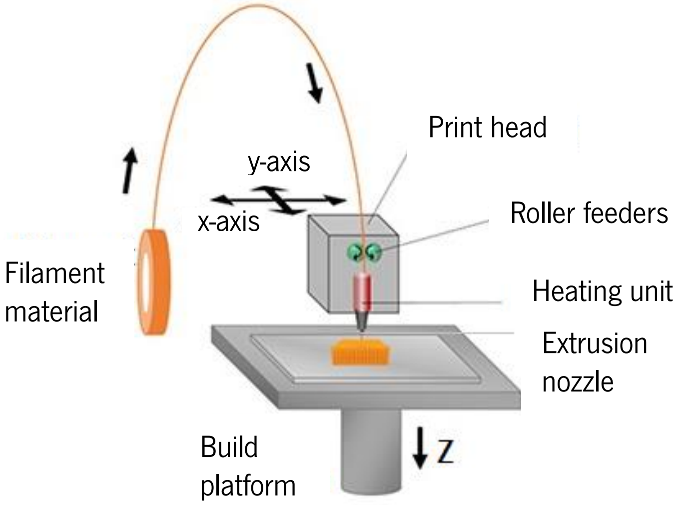

Figure 20. Schematic FDM process. Adapted from [187].

For this printing technology, suitable polymeric materials are thermoplastics, such as polycarbonate, polyphenylsulfone, ABS, and polylactic acid (PLA). These become molten at reasonably low temperatures and solidify fast enough, holding their shape when hardened [186].

The simplicity, ease handling, rapid processing, reliability, and cost-efficiency are the main advantages of the FDM process. The main drawback of FDM is the final surface roughness, which depends on the 3D printer's minimum layer height. The printed objects tend to have visible layer lines, inaccuracies and this can cause unacceptable surface roughness values. Besides that, this technique has the lowest accuracy and resolution along the z-axis when compared with other AM techniques. Another important disadvantage of FDM printers is the lack of thermoplastic polymers available for this technology. Regarding the mechanical strength of the printed parts, the process of FDM manufacturing can provide good and reproducible results [6,183,185,188,189].

4.1.2. Stereolithography (SLA)

Invented in the 1980s, the world's first 3D printing technology was stereolithography and it is still being predominantly used nowadays. Like FDM, models are built layer by layer, however, SLA uses a photocurable polymer. Typically, a liquid resin is hardened by applying a UV laser in a process called photopolymerization [185]. This 3D printing technique provides objects containing high resolution and precision, definite details, slightly visible layer lines, and an extremely smooth surface finish. Those characteristics combined with its versatility are the main benefits of this 3D printing technique. SLA is typically the more efficient process, but it requires more labor-intensive and it is costly when compared to FDM. The construction of a 3D object with SLA can be accomplished in two ways, the bottom-up or bottom-down process. Only the second one was used in this work, which is next described and presented in Figure 21.

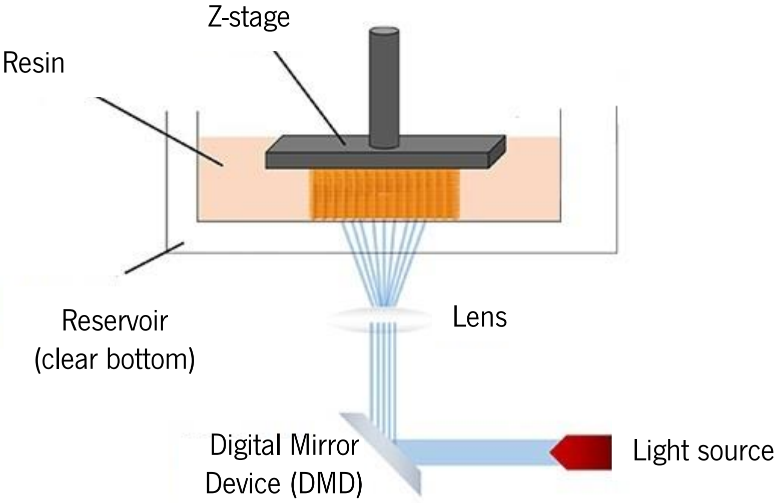

Figure 21. SLA basic parts. Adapted from [187].

The resin is detained in a build tank and the “printhead” is a laser beam, which is focused on a particular focal depth. Then, the laser is moved to trace a pattern and solidify the resin, creating the first layer printed. After that, the platform is raised upward along the z-axis, allowing a new layer of liquid resin to cover the cured layer. This process repeats, creating the object layer-by-layer. Notice that, functional groups that did not react in the solid layer when they are exposed to the resin in the new layer, can then polymerize. This ensures good adherence between each layer of the build.

After the planar sections are completed, the prototype is post-cured exposing it to a final step using UV light in a controlled furnace, in order to ensure the final polymerization of unreacted functional groups in the polymer. At the end of the process, the excess resin is drained and carried away [108,186,190].

In addition, to obtain the optimal resolution, the thickness of the cured layer should be controlled. For a given resin, the energy of the light to which the resin is exposed determines the cure depth and can be controlled by adjusting the power of the light source, the scanning speed, or the exposure time [108,185].

To better understand and compare these two AM techniques, Table 6 summarizes some advantages and disadvantages of FDM and SLA.

Table 6. Summary of advantages and disadvantages of FDM and SLA technologies.

	Advantages	**Disadvantages**
FDM	Low or moderate costs of equipment; Economical (inexpensive materials); High structural stability, chemical, water and temperature resistance properties of materials; Fast; Wide range of colorful printing materials.	Suitable materials are limited to thermoplastics; Difficult to control build plate temperature, which is crucial for the best results; The resolution along the z-axis is low.
SLA	Good resolution; Good mechanical properties; Excellent surface finish; Finished parts can be painted;	Expensive equipment and materials; Suitable materials are limited to photosensitive resins; Waste material is not recyclable and is hard to manage; Supports are needed; The laser needs to be calibrated periodically.

4.2. Experimental Procedures

This section focus on the experimental procedures carried out to perform roughness measurements and the flow visualizations as well as, all the working steps applied during data analysis.

4.2.1. Roughness Measurements

Surface roughness is crucial for several applications and flow visualizations are one of them. Although its effect on flow visualization has never been investigated, in this study it was found that it is a relevant parameter and of great importance. Nevertheless, roughness measurement procedures depend on stylus instruments which have only limited flexibility [191]. For instance, in the present work, the surface profiler (Dektak® 150, Veeco) used, can only perform relevant and reliable measurements on flat surfaces. For this reason, cubes were 3D printed to conduct the study, and the setup used is depicted in Figure 22.

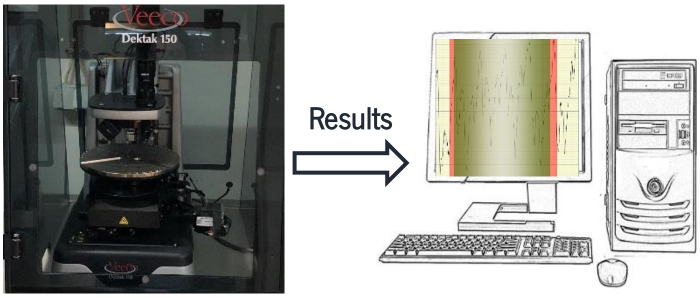

Figure 22. Surface profiler and the computer showing the output results.

Surface roughness most frequently refers to the variations in the height of the surface relative to a reference plane [192]. There are several roughness parameters, however, in the present study, only the arithmetic mean roughness (Ra) was studied since it is the most commonly used to indicate the level of surface roughness [193]. The magnitude of Ra represents the area between the roughness profile and its mean line (Figure 23) and it is estimated as follows in Equation 5 [194]:

$$Ra = \frac{1}{L}\int_{0}^{L} |z(x)|\, dx \tag{5}$$

where L is the sampling length, and $z(x)$ is the absolute ordinate.

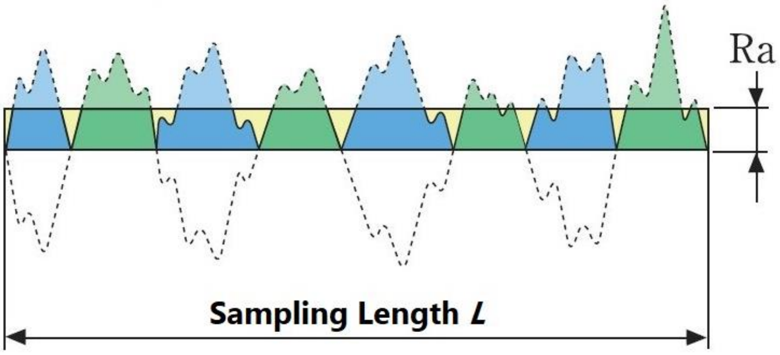

Figure 23. Average roughness illustration. Adapted from [195].

4.2.2. Blood Analogues and Flow Visualizations

Real whole blood is difficult to manipulate *in vitro*, namely, because of ethical, economical, and safety issues involved. For those reasons, the use of blood analogues has become of interest and have been widely used in several experimental studies, because of their advantageous characteristics such as nontoxicity, low cost, transparency, and the absence of ethical issues [28,196]. In the present study, the fluid selected as blood analogue was a dimethyl sulfoxide (DMSO)/water mixture (52%/48%-w/w), which matches the refractive index of both biomodels presented and it has similar rheological properties to the blood ($\mu = 0.00315\ \mathrm{Pa \cdot s}$ and $\rho = 1072\ \mathrm{kg \cdot m^{-3}}$) [197]. The refractive index is an important characteristic since it reduces undesirable optical distortions and hidden regions and reflections that can difficult the obtention of accurate measurements [196]. In suspension of the blood analogue fluid, 40 μm monosized spherical microparticles were used, (CA 40, Spheromers®) at a concentration of 0.2 %. Some tests were made to find the appropriate percentage of particles, and it was concluded that the most suitable was 0.2%.

The experimental method used to perform the flow visualizations and measurements was a high-speed video microscopy system, which is commonly used in experimental fluids. This method allows obtaining detailed and valuable information about the fluid flow that occurs in microscopic timescales, by acquiring a series of image frames captured at a high temporal and spatial resolution [198,199].

The whole experimental setup used is depicted in Figure 24 and it consisted of an inverted microscope (IX71, OLYMPUS, Tokyo, Japan) combined with a high-speed video camera (Fastcam SA3, Photron, USA).

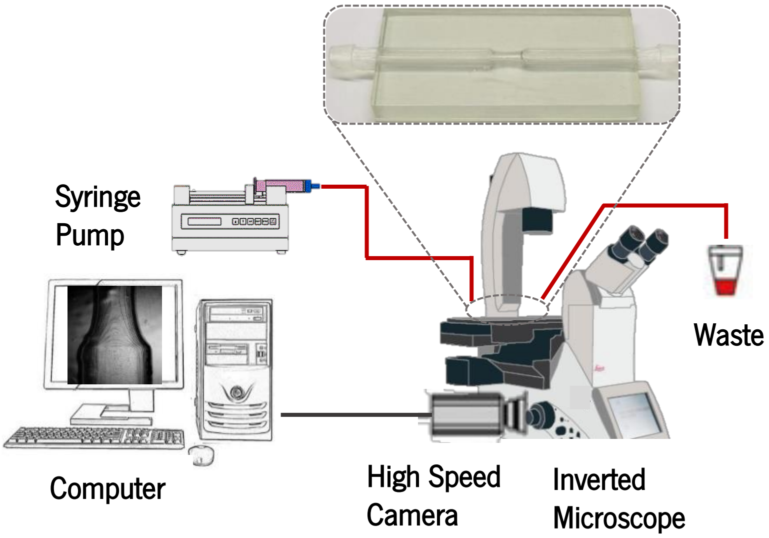

Figure 24. Experimental equipment used to control and visualize the blood analog flow.

The biomodels were placed and fixed in the microscope. To control and impose a constant inlet flow rate ($5\ \mathrm{ml \cdot min^{-1}}$), a syringe pump (LEGATO® 100, USA) was used. Various sequences of images were captured and recorded by the high-speed video camera only on the center and post stenotic region, which are the zones of interest. To obtain good quality results, for each case the best frame rate and illumination were adjusted and, thus minimizing image artifacts. The recorded series of images were transferred to a computer and evaluated by using an image analysis software.

4.2.3. Imaging Technologies and Velocity Measurements

To process and extract data from the video sequences captured by the high-speed camera, an image handling software ImageJ was used [200], which is commonly applied by most researchers. Essentially, two main methods were applied to analyze and present the data obtained during this dissertation. The first one is the Z Project function in ImageJ. This function was first applied to select the median projection type. After that, the image calculator tool was used to subtract the median from the original image. Finally, the Z project function was employed again selecting the maximum or minimum intensity to obtain the images presented in this work. The second one is the tracking plugin, MTrackJ [201]. This plugin was used to manually track the centroid of individual microparticles, by starting to apply the two first steps discussed above, aiming to remove the noise and image artifacts. By performing the trajectories of particles for a given frame rate, this plugin has as output the x and y positions and the respective velocity for each trajectory of each particle (Figure 25).

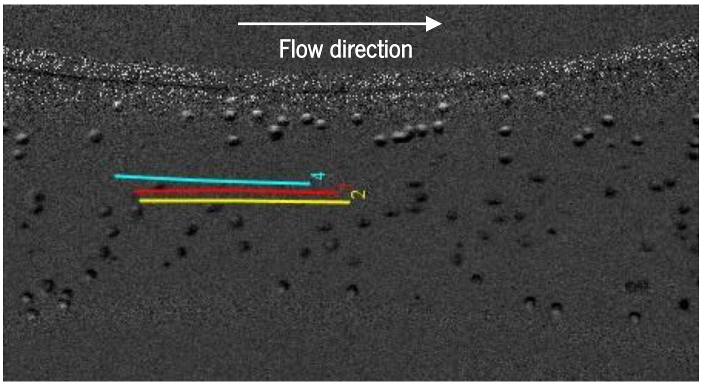

Figure 25. Manual method showing the trajectories of particles.

Note that, since the regions of interest in this study are the stenotic and post stenotic region of the biomodel, the frame rate selected for each case was different. Lower values (1000 frames per second) were selected to obtain the images that only show the flow behavior. In turn, to track the particles and measure their velocities at the stenosis throat, the frame rate selected was higher (6000 frames per second). In this location, the velocity increases and so, to reliably track the particles it is necessary to increase the frames number. Moreover, it should be highlighted that as the severity of stenosis increases, the velocities are higher and the errors associated also increase due to particle-position uncertainty [202].

Chapter 5

Blood Flow Modeling

Fluid dynamics studies have been used to complement and improve our understanding of cardiovascular diseases. However, to solve those problems, it is important in one first stage to understand the mathematical basis, the physical principles behind the mathematics, the governing equations for the problem, among other issues. This chapter aims to define and explain the mathematical models used for this work, as well as present relevant literature review of blood flow modeling.

5.1. Literature Review

Despite the variety of experimental studies and blood flow measurement techniques, there are some difficulties associated with them. For instance, *in vitro* WSS measurements are extremely difficult to perform and the velocity measurements have high associated errors. These combined with other complications of directly measuring quantities of interest, have motivated the use of computer simulations and CFD to predict them *in silico* [203].

The earliest numerical detailed studies solving the flow problem in constricted tubes were conducted by Lee and Fung (1970) [204]. After that, other studies in this field conducted by Caro, Glagov and Ku et al. can be highlighted [44,205,206]. Ever since, CFD approaches have been progressively adopted by most researchers as the preferred technique for numerical modeling of hemodynamics.

Like in experimental studies, the numerical hemodynamic analysis of CAD has been performed by many researchers, using one of two approaches: idealized stenotic geometries with idealized shapes (e.g. half-sphere [207], ellipsoid [208], gaussian equation [209], cosine function [22], among others designed by the authors themselves [210]) or realistic coronary arteries models extracted from patient's medical data [46,47,211–213]. In addition to the geometrical models, the boundary conditions assumed in each investigation vary from author to author.

Chaichana et al. [20] performed an interesting study on the hemodynamic effect of variations in the angulations of the left coronary artery, simulating blood flow in LCA models, based on idealized and realistic coronary artery models. This study showed a strong relation between hemodynamics and LCA angulations. Consistent observations between idealized and patient-specific LCA models demonstrated that for particular parameters, the idealized models help to understand their impact in hemodynamics.

They showed a direct correlation between wide angulation in the LCA and hemodynamic changes, such as disturbed flow and low WSS, possibly inducing the development of atherosclerosis. In another work [47], they investigated the influence of realistic coronary plaques on the LCA side branches, based on coronary CT angiography images in a patient with CAD, and also compared the effect of non-Newtonian and Newtonian fluid on WSS. Coronary plaques were found to be closely related to the subsequent WSS and wall pressure stress gradient changes in the coronary side branches. They observed that the highest wall pressure stress gradient was in stenotic regions, as well as the WSS, which was similar for both non-Newtonian and Newtonian models. In the post stenotic section, a low flow velocity was found. Then, the same authors [212] studied various types of plaques in different anatomical positions of the LCA to represent a realistic distribution of coronary plaques. WSS and flow velocity were found to change at different stenosis locations and a high WSS was found at 70% lumen stenosis. Similarly, Zhang et al. [214] also proved that different locations and stenosis length affect blood flow behavior.

Gaudio et al. [50] compared Newtonian and non-Newtonian blood behaviors in patient-specific stenotic coronary arteries at different grades of stenosis. For that, the researchers investigated numerically the blood velocity and the distribution of the shear stress indices at different times of the cardiac cycle. Their results showed that the velocity for the Carreau-Yasuda model is slightly lower when compared to the Newtonian model, but the non-Newtonian effects are most important in shear stress indices distributions.

Kamangar and his team [46] investigated the effect of stenosis in left coronary arteries on the hemodynamics in suspected CAD patients. They measured the pressure, velocity, and WSS during the cardiac cycle and observed a considerable pressure drop across the stenosis and an increase in the velocity and wall shear stress at the stenosis. The high WSS at the stenosis throat may cause plaque rupture. In the post stenosis section, they observed the prevalence of the recirculation zone which can result in the formation of new stenosis.

In a study carried by Biglarian et al.[215], the stenosis effect in two different modeling conditions, static and dynamic (modeling the heart motion) for real pulsatile inlet mass flow was investigated numerically. They concluded that the arterial wall motion affects the WSS and the plaque formation site. For that, the researchers studied the WSS profiles and in both degrees of stenosis, the maximum WSS (center of the artery) increases with the degree of stenosis.

It can be seen that the articles mentioned above [46,50,215,216] are in agreement concerning the results obtained for WSS and post-stenotic flow behavior.

A different way to study the effect of stenosis in blood flow hemodynamics was addressed by Doutel et al. [11]. They developed a methodology to create three-dimensional irregular stenosis with different degrees of occlusion in artery models for numerical and *in vitro* hemodynamic studies. This process is based on the identification of areas with low WSS, because these are the locations prone to the development of atherosclerosis. This method allows a rapid hemodynamic comparison between healthy and a stenotic case for a given artery geometry, which is useful for researchers to perform computational studies of blood flow in stenotic vessels. Applying this methodology, the authors in another investigation [35], evaluated the influence of non-planarity through patient-specific LCA models that deviate from its original geometry in their planarity.

Besides the effect of stenosis, several studies have emphasized the importance of the non-Newtonian behavior of blood. An interesting study was undertaken by Razavi et al. [209] aiming to compare six Non-Newtonian models and a Newtonian model. The authors used axisymmetric stenotic models and evaluated parameters such as WSS, velocity, and non-Newtonian effects, through an unsteady flow condition. The results showed that the power-law model produces higher deviations, in terms of velocity and wall shear stress in comparison with other models, overstating Non-Newtonian behavior. The generalized power-law and modified-Casson models are more prone to Newtonian state, however, they underestimate non-Newtonian behavior. In contrast to previous models, Carreau and Carreau–Yasuda represented moderate IG values (cut-off value above which flow can be assumed as non-Newtonian) proving to be the suitable models to mimic the blood. Besides that, the authors verified that the increasing stenosis intensity causes flow patterns more disturbed downstream of the stenosis, and WSS increases significantly at the stenosis throat, which is in agreement with the previous studies.

Despite most investigations consider the blood flow as laminar, the presence of the stenosis, curvature effects and the pulsatile nature of the blood flow through arteries, can cause the transition from laminar to turbulent flow condition, even at much lower Re numbers. For this reason, some authors have been used turbulent models in computational simulations. Mahalingam et al. [216] utilized the Shear-stress transport (SST) k-ω model to study the turbulent transition during pulsatile flow through coronary arteries for different degrees of stenosis and analyzed quantitatively. They demonstrated that the transition to turbulence starts occurring above 50% stenosis, but affects significantly the hemodynamic parameters like WSS and oscillatory shear index (OSI) for stenosis above 70%.

The prior studies assumed the wall to be rigid, however, in recent years, fluid-structure interaction (FSI) (an approach that can simultaneously model blood flow and arterial wall deformations) has received increasing interest due to its potential impact in the medical field. One of the most cited works in this area was performed by Torii et al [217] wherein the effects of compliance in WSS calculations were studied. For that, they compared a rigid and compliant wall for a stenotic right coronary artery, considering the physiological velocity and pressure waveforms. Recently, Ahmadi and his team [21] modeled a stenotic artery and studied the dynamic behavior of the atherosclerosis phenomenon through FSI. More considerations were taken comparing to Torii et al, since they also studied the influence of plaque angle, percentage of stenosis, non-Newtonian properties of the blood flow, and hyperelastic artery models.

Taking into account the variety of studies in the literature, some considerations taken in numerical studies of stenotic coronary arteries are summarized in Table 7.

Table 7. Numerical studies of hemodynamics and the respective assumptions for numerical simulations.

Geometry	Modeling approaches	Fluid	Boundary conditions			Authors
			Wall	Inlet	Outlet	
Idealized	k-ω turbulent model	Non-Newtonian (Carreau model)	Rigid (No slip wall)	Spiral boundary condition with a parabolic velocity profile	The default setting for the gauge pressure	Kabir et al. [54]
Idealized	k-ω turbulent model (SST)	Non-Newtonian (Carreau model)	Rigid (No slip wall)	Time-dependent flowrate profile	Time-dependent pressure profile	Mahalingam et al.[216]
Idealized	Laminar	Non-Newtonian (Cross model)	Rigid (No slip wall) and Flexible wall (FSI)	Constant velocity inlet (45 m/s)	Constant pressure outlet (10KPa)	Mulani et al.[22]
Idealized	Laminar	Newtonian	Rigid (No slip wall)	The time-dependent mass flow profile	Zero surface tension	Biglarian et al. [215]
Idealized	Laminar	Newtonian	No-slip wall and elastic nature	Time-dependent flowrate profile	Time-dependent pressure profile	Wu et al.[210]
Patient-specific	Laminar	Non-Newtonian (Generalized power law)	Rigid (No slip wall)	Time-dependent flowrate profile	Time-dependent pressure profile	Chaichana et al.[47]

		and Newtonian				
Patient-specific	Laminar	Non-Newtonian (Carreau model)	Rigid (No slip wall)	Time-dependent velocity profile	Time-dependent pressure profile	Liu et al.[55]
Patient-specific	Laminar	Newtonian	Rigid (No slip wall) and Flexible wall (FSI)	Parabolic velocity profile	Flow partition implied in Murray's law	Siogkas et al.[218]
Patient-specific	Laminar	Newtonian	Rigid (No slip Wall) and Flexible wall (FSI)	Time-dependent velocity profile	Time-dependent pressure profile	Torii et al.[217]
Patient-specific	Laminar	Non-Newtonian (Carreau-Yasuda) and Newtonian	Rigid (No slip Wall)	Time-dependent velocity profile	Time-dependent pressure profile	Gaudio et al.[50]

Considering the diversity of studies performed in stenotic coronary arteries, in the present dissertation the effects of the degree of stenosis on blood flow are evaluated, assuming the wall as rigid. Furthermore, taking into account the conclusions of Razavi et al. [209], the Carreau model was applied to compare the influence of the Non-Newtonian model on blood flow in stenotic arteries. Additionally, the SST k- ω model was studied since it was the most found in the literature to model blood flow under turbulent conditions.

5.2. Computational Fluid Dynamics (CFD)

CFD is an extremely powerful technique commonly used by engineers, which allows the analysis of systems involving heat transfer, fluid flow, and associated phenomena such as chemical reactions through computer-based simulation [219,220]. In the last decades, CFD investigations have been increasingly used in biomedical research of CAD because of its high-performance hardware and software. It can be employed as a research tool to better and deeply understand the physical nature of blood flow, providing valuable hemodynamics results, useful in the clinical assessment [8,9,220]. For instance, it allows evaluating blood flow along the cardiac cycle with various physiological conditions, and estimating induced vessel wall stresses [31].

There are several advantages of CFD over experiment-based approaches, like the substantial reduction of lead times and costs of new designs and developments, the ability to study systems where controlled experiments are difficult to accomplish because of hazardous conditions and almost unlimited level of detail of results [220–222]. Despite the advantages presented, numerical computations surely will never completely replace experimental studies.

A CFD code encompasses three main steps: pre-processing, solving, and post-processing [223] (Figure 26).

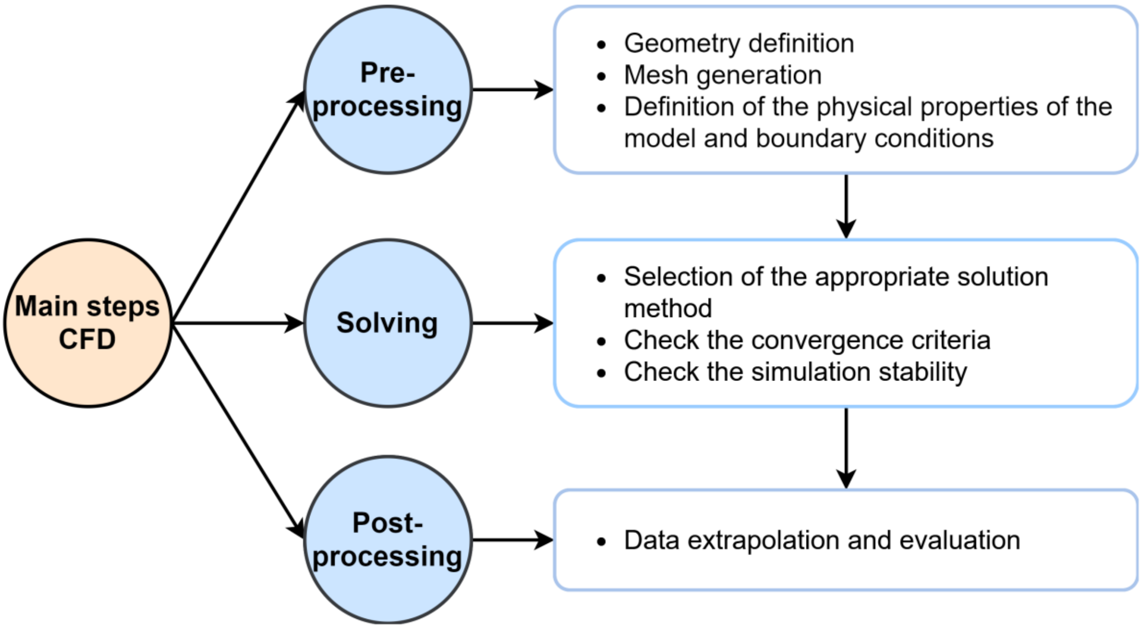

Figure 26. Main steps involved in CFD simulations.

The initial point of any numerical method is the description of the mathematical model, *i.e.* the definition of the differential equations, and the implementation of the boundary conditions and other parameters that need to be modeled (geometry, mesh generation, fluid properties, among others). After that, it is necessary to choose a suitable discretization method to convert the governing partial differential equations to a system of algebraic equations. To obtain approximate solutions to these equations, numerical methods have been used, of which, the most popular are finite difference, finite volume, and finite element methods. In this work, only the Finite Volume Method (FVM) is implemented in the CFD code of the software used. Despite the difference between these methods, the basis of the solver is to perform an approximation of unknown flow variables employing simple functions, discretize by substitution those approximations into the governing flow, and obtain an algebraic solution [220,223,224]. After the solution be determined, in the post-processing the user can visualize the computational results, such as velocity vectors, streamlines, and WSS contour plots [9].

5.2.1. Governing Equations of Fluid Flow

The mathematical governing equations which describe the laws of fluid mechanics are the continuity equations of mass and momentum (Navier-Stokes). These are mathematical statements of two fundamental physical principles upon which all of fluid dynamics is based [14,31]:

- The conservation of mass.
- The conservation of momentum (Newton's second law, the rate of change of momentum equals the sum of forces acting on the fluid).

For a three-dimensional, homogeneous, laminar flow and incompressible fluid, the governing equations, in the differential form, are summarized in Equation 6 and 7:

Continuity

$$\nabla\cdot \vec{u} = 0 \tag{6}$$

Momentum

$$\rho\left(\frac{\partial\vec{u}}{\partial t} + \vec{u}\cdot\nabla\right) = -\nabla p + \mu\nabla^2\vec{u} \tag{7}$$

Where $\vec{u}$ is the velocity vector, t is the time, p is the static pressure, ρ is the fluid density and μ the dynamic viscosity.

5.2.2. Turbulence Models

In the laminar regime, flows are completely described by the continuity and momentum equations. Nevertheless, in a stenotic artery, small disturbances within the fluid of laminar flow can eventually lead to a chaotic and random state of motion, which is a condition of turbulence [9]. To capture the turbulent fluctuations in the flow field, turbulence models involve additional equations or modifications to the governing equations.

One of the difficulties associated with modeling turbulent flow in CFD, concerns the selection of the most suitable turbulence model, not only because of the many variations that may appear for each model, but also because it depends on the problem considered, like the physics of the flow, the level of precision required, the existing computational resources, the amount of time available for the simulation, among others [56,225]. The Reynolds Averaged Navier-Stokes (RANS) models offer the most economic approach for computing complex turbulent flows and the computing resources required for reasonably accurate flow computations are modest, so this approach has been the most used in engineering flow calculations in the last decades [56,220]. This produces a set of time-averaged equations with the turbulent features encapsulated by a new term called the Reynolds stress [9]. Each model has its strengths and weaknesses and range in complexity, which are summarized in Table 8.

Table 8. Summary of common RANS turbulence models.

Turbulence model	Notes	Advantages	Disadvantages
Spallart Almaras	One-equation model.	Relatively simple; Good performance for wall-bounded flows, flows with mild separation and recirculation and for boundary layers with adverse pressure gradients.	Bad for large separation, decaying turbulence and is not well calibrated for free shear flows; Lacks sensitivity to transport processes in rapidly changing flows.
k-ε	Two-equation model, one for k and ε each; Assumes fully turbulent fluid flow.	Robustness; Economic; Reasonable accuracy for a wide range of turbulent flows and stable calculations.	Insensitivity to adverse pressure gradients and boundary layer separation; Poor predictions for swirling and rotating flows; flows driven by anisotropy of normal Reynolds stresses.
k-ω	Two-equation model, one for k and ω each.	The ω equation can be integrated without additional terms through the viscous sublayer; Better in predicting adverse pressure gradient boundary layer flows and separation; More accurate turbulent profile near the wall.	Relatively strong sensitivity of the solution depending on the freestream values of k and ω outside the shear layer.
SST k-ω	The SST - k-ω model is a transformation of the k– ε model into a k– ω model in the near-wall region with the k– ε model in the fully turbulent region in the far-field.		
Transition-SST	Four-equation model. It couples the SST k-ω transport equations with two	The great advantage of the SST model is its robustness and ease of use.	Additional mesh refinement is necessary, in order to properly capture the rapid transition.

	other transport equations, one for the intermittency and one for the transition onset criteria.		
RES	Seven additional equations, one each for the six independent Reynolds stresses, and one turbulent dissipation.	Predicts accurately more complex flows, accounting for streamline curvature, strong swirl, rotation, and separation.	Relatively complex; High cost of the computations due to additional equations and reduced convergence.

Within arteries, the k-ω turbulence model is currently preferred for turbulent flow CFD simulations and it seems to provide more accurate results than other turbulence models [225]. To obtain near-wall results, all k-ε turbulence models use wall functions and they were found to be inadequate for blood flow problems [225,226]. In concrete, the SST k-ω model has been used for several authors in stenotic coronary arteries and they concluded that it is the best-suited RANS turbulence model to capture the transition, if any, to turbulent state [216,226]. As showed in Table 8, the SST k-ω model is based on both the standard k-ω model and the standard k-ε model. To combine these two models, the standard k-ε model has been transformed into equations based on k (turbulence kinetic energy) and ω (specific dissipation rate), which leads to the introduction of a cross-diffusion term (D_ω). The k and ω, are obtained from the following transport equations (Equation 8 and 9):

$$\frac{\partial}{\partial t}(\rho k) + \frac{\partial}{\partial x_i}(\rho k u_i) = \frac{\partial}{\partial x_j}\left(\Gamma_k \frac{\partial k}{\partial x_j}\right) + G_k - Y_k + S_k \tag{8}$$

$$\frac{\partial}{\partial t}(\rho \omega) + \frac{\partial}{\partial x_i}(\rho \omega u_i) = \frac{\partial}{\partial x_j}\left(\Gamma_\omega \frac{\partial \omega}{\partial x_j}\right) + G_\omega - Y_\omega + D_\omega + S_\omega \tag{9}$$

In these equations, G_k represents the generation of turbulence kinetic energy due to mean velocity gradients, G_ω represents the generation of ω. Γ_ω and Γ_k represent the effective diffusivity of k and ω, respectively. Y_k and Y_ω represent the dissipation of k and ω due to turbulence. Finally, S_k and S_ω are user-defined source terms [56].

5.2.3. Discretization Methods

The FVM method is a numerical technique that, as a starting point uses the integral form of the conservation equations. In general, this method involves several steps: the decomposition of the problem domain into control volumes (grid generation); formulation of integral balance equations for each control volume (discretization), and solution of the discrete algebraic system [220,222,224].

The first step consists in the division of the solution domain into a finite number of control volumes (CV), and the conservation equations are applied to each CV. The boundaries (or faces) of the CV are located mid-way between adjacent nodes. Figure 27 presents part of a 2D mesh used to subdivide the domain, in which the usual notation for identifying each node, faces, and neighboring elements can be observed.

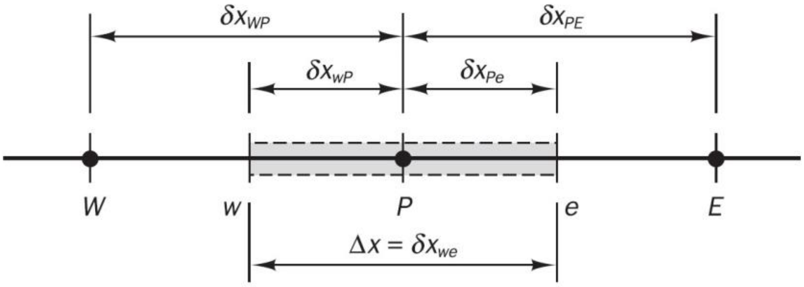

Figure 27. Typical control volume and nomenclature used for equation discretization. Adapted from [220].

A general nodal point is identified by *P* and its neighbors, in a one-dimensional geometry, are identified by *W* (west) and *E* (east). The next step is the discretization, consisting in the integration of the governing equations over each control volume to yield a discretized equation at its nodal point *P*. After the equations are discretized, a set of algebraic equations for each CV is obtained, linking the value of the variable at an element to the values at its neighbors. The algebraic equations are then assembled into global matrices and the resulting system can be then solved by an iterative method. These iterative methods are based on the repeated application of an algorithm, which leads to the convergence of the system of algebraic equations [9,220,222].

Moreover, the FVM method is strictly conservative, since the flux which enters in a given volume is equal to that leaving the adjacent volume. Another advantage of this method is the ease implementation of a variety of boundary conditions (BC) in a noninvasive way since the unknown variables are evaluated at the centroids of the volume elements, not at their boundary faces. Besides that, this approach can accommodate any type of grid, so it is suitable for complex geometries and it is possibly the simplest to understand and to program. These properties of the FVM make it the preferred method in CFD and suitable for the numerical simulation of a variety of applications involving fluid flow [219,224].

5.2.4. Solution Algorithm

Since the discretized equations are non-linear, an iteration scheme is used to solve them. ANSYS FLUENT® provides different pressure-based algorithms that employ a similar discretization process, but the approach used to linearize and solve them is different. These can be separated into a segregated algorithm and a coupled algorithm. In the segregated algorithm (SIMPLE – Semi-Implicit Method for Pressure-Linked Equations, SIMPLEC – Semi-Implicit Method for Pressure Linked Equations-Consistent, and PISO – Pressure-Implicit with Splitting of Operators), the governing equations are solved sequentially, segregated from one another. In the coupled algorithm, the momentum equations and the pressure-based continuity equation are solved in a coupled manner. Generally, SIMPLE or SIMPLEC are used for steady-state calculations, while PISO is recommended for transient calculations or calculations on meshes with high skewness. The Coupled algorithm enables full pressure-velocity coupling [56,224].

In the present study, the SIMPLE algorithm was used. In this algorithm, the velocity field is obtained from momentum equations and the pressure field is obtained by solving a pressure correction equation. The solution is found iteratively by generating pressure and velocity fields that successively satisfy the momentum and continuity equations while approaching the final solution at every iteration [219,220]. The solving process is iterative until the solution converges, which happens when the difference between two successive iterations is less than the selected value [219].

It should be noticed that in some cases the solution did not converge with the SIMPLE algorithm and so the Coupled method was used, since this improves significantly the convergence over the segregated algorithm [56].

5.2.5. Mesh

A mesh can be regarded as a number of elements or grid cells that involve the entire geometric domain and result from the discretization of the original geometry into a set of subdomains, called control volumes [9,219]. However, the purpose of constructing a mesh is not a simple question of creating a mesh of the domain of interest, but to obtain a good quality mesh, and most of the time spent is devoted to this process. This is an extremely important step, because the mesh quality plays a significant role in the accuracy and stability of the numerical computation, which consequently is reflected in the results [56,223,227].

The larger the number of grid cells, the better the solution accuracy. In other words, the finer the mesh, the better the accuracy of a CFD simulation [220,223]. The accuracy of a solution and the required time for computational problem solving is dependent on grid fineness. A highly refined mesh may give very accurate results, however, its simulation time may be unreasonable [223].

Regardless of the type of mesh used, it is necessary to analyze the quality of the cell, because also has a significant impact on the accuracy of the numerical solution. This includes its aspect ratio, orthogonal quality, and skewness, however, in the present study only the last two were evaluated, since these are considered the most important.

Skewness is defined as the difference between the shape of the cell and the shape of an equilateral cell of equivalent volume, i.e this criterion evaluates the geometric perfection of an element (Figure 28). Cells with high skewness can compromise and decrease the accuracy of the computational results, or lead to numerical instabilities. For quadrilateral cells, the mesh lines should be at an angle θ of approximately 90° (orthogonal). Whereas, triangular meshes should have angles close to 60° and inferior to 90°. It is suggested that the maximum skewness for a triangular/tetrahedral mesh be kept below 0.95, with an average value significantly lower. With a maximum value above 0.95, the convergence can be difficult and may require changing the solver controls [9,56].

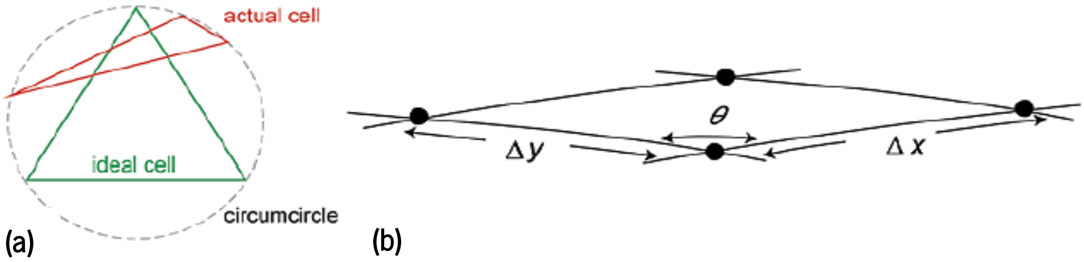

Figure 28. An example of (a) a highly skewed triangular cell, and (b) a quadrilateral cell. Adapted from [9].

Another important indicator of mesh quality is the orthogonal quality and also varies between 0 and 1. The worst cells will have an orthogonal quality closer to 0 and the best cells will have an orthogonal quality closer to 1 (perfect orthogonal element). The minimum orthogonal quality should be higher than 0.01, with an average value that is significantly higher [56].

In addition to the mesh quality, mesh independence studies should be carried out to assure a compromise between accuracy and computational resources. For that, flow results are checked using different refinement meshes, and the mesh is considered adequate when the results are almost unchanged with the decreasing of the cell size and are only a consequence of the simulation conditions.

Chapter 6

Case of Study

This chapter presents the case of study, indicating the geometry dimensions, the meshes developed for each model, the boundary conditions applied to solve the problem under study, and the printing parameters used to fabricate the physical biomodels.

6.1. Geometry

The first step required to study blood flow has consisted in the acquisition of the three-dimensional geometry of the coronary arteries' lumen. In this work, the geometry was built based on a 2017 study [228] of the coronary artery diameter in 167 adult patients through a coronary angiography, where an average value of 2.9 mm was obtained. After the diameter selection, the geometric configurations of coronary lesions were defined. Coronary lesions can be morphologically classified as concentric or epicardial stenosis, eccentric stenosis, and multiple irregularities. The first one is an axisymmetric narrowing of a coronary artery. In other words, a concentric stenosis means equal deposition of plaque on both walls. The second one, is an asymmetric narrowing of a coronary artery, with a preferential deposition of the plaque on the outer wall. In the third case, three or more successive and severe closely spaced blocks are found in a coronary artery [128,229]. Given the higher prevalence of concentric stenosis in humans, this will be the stenotic geometry addressed in this work.

Considering the characteristics mentioned above, two different geometries were developed and from now on, these will be designated as Model 1 (developed at University of Minho) and Model 2 (developed by Biofabics[16]). Both models are represented in Figure 29.

---

[16] Biofabics, is an R&D company specialized in the generation and culture of 3D Biotissue analogues, who collaborated in this work, having provided *in vitro* stenotic biomodels.

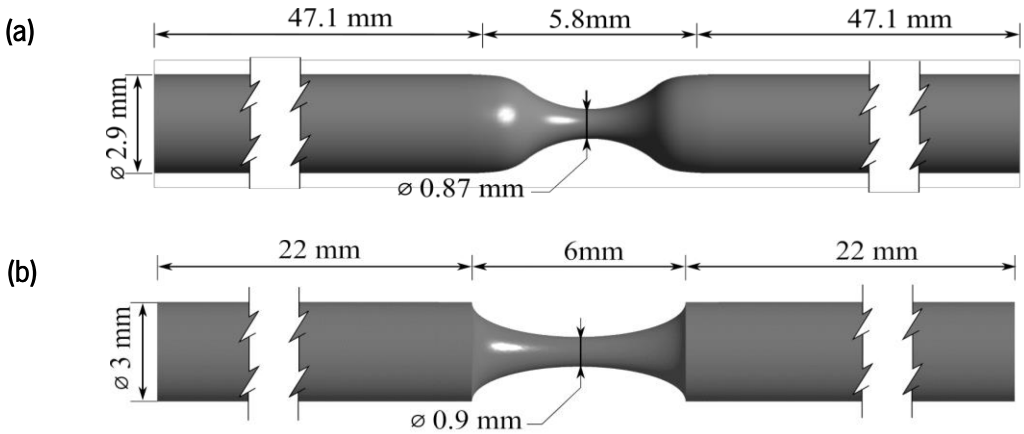

Figure 29. Dimensions of the stenotic model with a diameter reduction of 70%. (a) Model 1, (b) Model 2.

It can be observed that the Model 2 has a smaller length and the diameter is assumed as 3 mm. This is due to the limit imposed by the SLA printer of Biofabics and their online platform which only allows introducing whole numbers. Besides that, the main difference between these two models lies in the stenosis geometry. While Model 2 has an ellipsoid stenosis with unrealistic pointed zones, Model 1 has a smoother transition when the diameter reduces, which is more closer to reality. For both models, the stenosis length was defined as twice the normal diameter, an assumption applied by several researchers [54,230–232]. In addition, the length of the inlet zone for both models was selected to ensure the creation of a fully developed inlet flow.

Another aspect that should be highlighted, is the degree of stenosis. This is referred to as the percent occlusion either by diameter or area. However, only some authors [64,120] consider the area reduction instead of diameter reduction. In this regard, since most medical books and authors [35,95,120,233,234] refer to the diameter reduction as the preponderant factor, this was used in the present study and the degree of stenosis is given by Equation 10:

$$Stenosis\ (\%) = \left(1 - \frac{d_{stenosis}}{d_{straight}}\right) \times 100 \tag{10}$$

According to the diameter reduction, these lesions can be defined as minimal (50%), moderate (between 50% and 70%), and severe or significant (70% or more) [234]. For this study, the percentages selected were based on the vast analysis of the literature, and it was concluded that only a reduction of 50% or more in the artery diameter compromises blood flow. Inferior to this no surgical intervention is required [120]. For this reason, 0%, 50%, 60%, 70%, and 80% of stenosis were considered. The selection of this set of models was also to ensure the capture of changes in flow behavior when the severity of stenosis increases.

6.2. Mesh Optimization

For the present numerical study, geometries were constructed in Ansys software and two different types of meshes were created for each geometry. For Model 1, a hexahedral mesh was created, combining the "sweep" method and the "edge sizing" tool with a bias factor. The sweeping method consists in using an initially meshed face (source) and sweeps that source through a path to a target face. The "edge sizing" was used to refine the mesh in the areas of interest, until an acceptable skewness was reached. The bias factor was applied to ensure the accuracy of computational calculations near the wall. The same process was applied to the remaining stenotic models, and the number of cells and medium skewness and orthogonal quality are presented in Table 9.

Table 9. Mesh characteristics of each degree of stenosis for Model 1.

	Without stenosis	**50%**	**60%**	**70%**	**80%**
Number of elements	112,500	315,900	496,000	510,720	403,200
Skewness	0.109	9.434e-02	0.107	9.4669e-002	0.189
Orthogonal quality	0.974	0.981	0.973	0.9783	0.950

To assure a mesh independent solution, grid tests were made in the 70% stenosis model, by refining the mesh and rerunning the simulations until no significant differences were observed. Table 10 shows the characteristics of the meshes built for this study. For each mesh, the maximum velocity was calculated, and the results are represented in Figure 30. It can be concluded that for meshes with more than 500000 elements, the results are independent of the mesh. Since the differences are minimal between the results of mesh 3 and 4, and taking into account the computational time, mesh 3 was selected (Figure 31). Similar meshes were created for the remaining models.

Table 10. Characteristics of the different meshes generated for Model 1 with 70% of stenosis.

	Mesh 1	**Mesh 2**	**Mesh 3**	**Mesh 4**	**Mesh 5**
Number of elements	60,800	329,550	510,720	752,000	1,140,000
Skewness	0.1380	0.1058	9.4669e-002	8.3534e-002	7.6122e-002
Orthogonal quality	0.9689	0.9759	0,9783	0.97917	0.9790

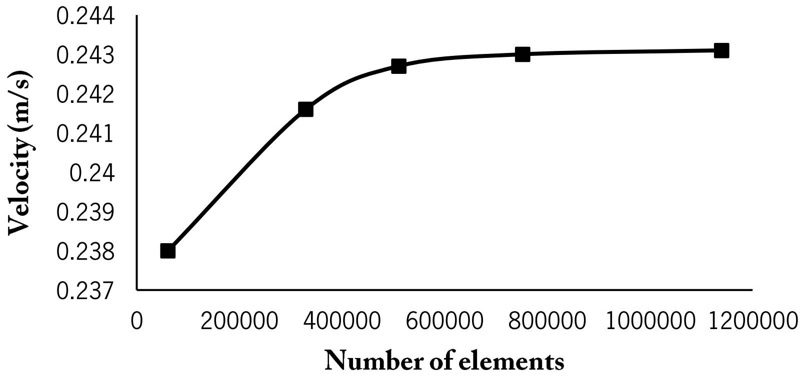

Figure 30. Variation of the velocity magnitude with mesh refinement for Model 1 with 70% of stenosis.

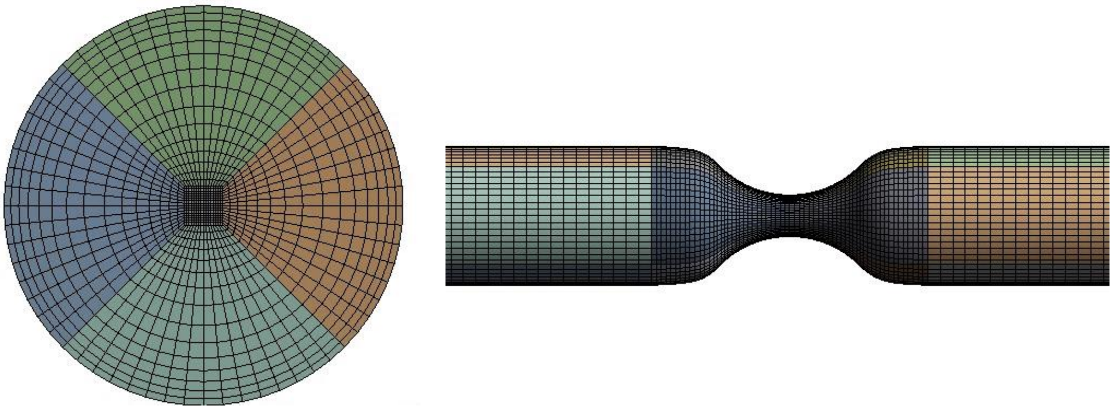

(a) **(b)**

Figure 31. Computational mesh selected for Model 1 with 70% of stenosis, (a) at the entrance, and (b) along the model.

For Model 2, the meshes constructed were more complex. These consisted of tetrahedral cells with inflation layers in the stenosis zone, and hexahedral cells with a bias factor in the remaining geometry. The characteristics of the various meshes are represented in Table 11. Similarly to the previous models, the inflation and bias factor were applied, in order to improve the accuracy of the computed WSS. Performing the same process as before, a mesh convergence study for 70% stenosis case was done and five different meshes were created (Table 12). According to the results (Figure 32), the mesh that combines accuracy and lower computation time for the 70% stenosis case is mesh 4 (Figure 33).

It should be noticed that to refine the mesh in the interest zones, both geometries were divided into different bodies.

Table 11. Mesh characteristics of each degree of stenosis for Model 2.

	Without stenosis	50%	60%	70%	80%
Number of elements	123,750	498,697	469,593	498,974	468,717
Skewness	0.124	0.1492	0.146	0.1457	0.135
Orthogonal quality	0.964	0.878	0.883	0.8952	0. 8899

Table 12. Characteristics of the different meshes generated for Model 2 with 70% of stenosis.

	Mesh 1	Mesh 2	Mesh 3	Mesh 4	Mesh 5
Number of elements	71,750	136,410	413,514	498,974	843,167
Skewness	0.1827	0.1527	0.1557	0.1457	0.1261
Orthogonal quality	0.8878	0.9113	0.8816	0.8952	0.9183

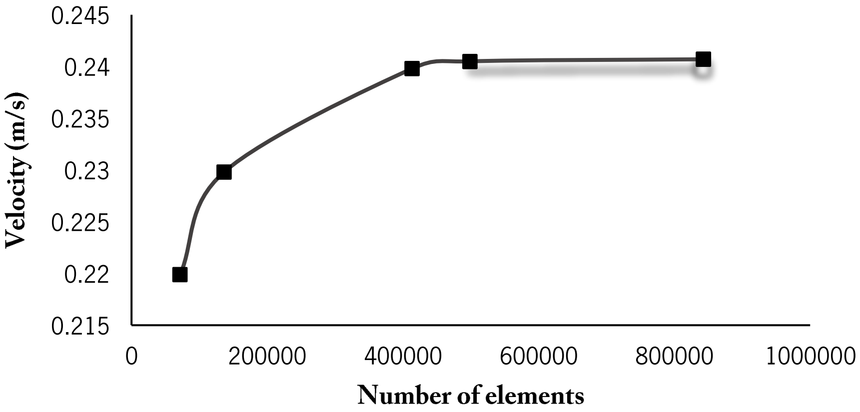

Figure 32. Variation of the velocity magnitude with mesh refinement for Model 2.

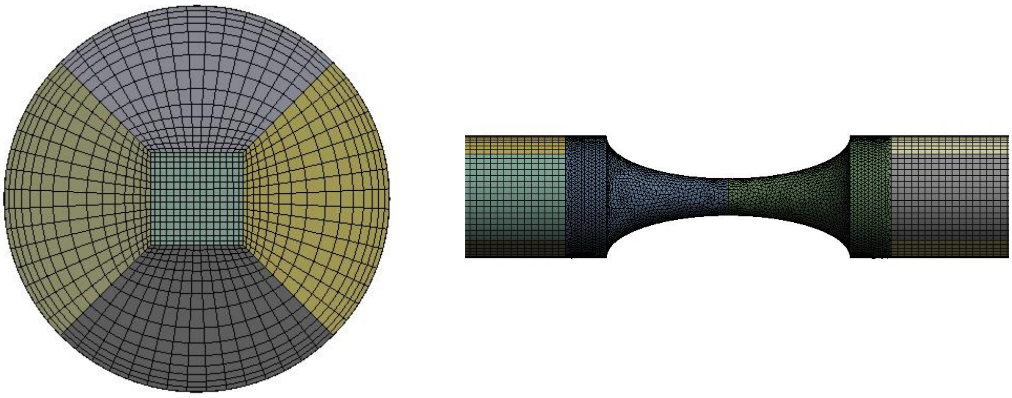
(a) (b)

Figure 33. Computational mesh selected for Model 2 with 70% of stenosis, (a) at the entrance, and (b) along the model.

6.3. Boundary Conditions

To carry out the numerical simulations, it was necessary to define the boundary conditions, which are a set of additional constraints to the problem on specified boundaries. Firstly, the blood was assumed as a Newtonian fluid to compare with the experimental data and a stationary inlet flow was applied. At the walls, a no-slip BC was imposed, which indicates that the fluid adheres to the walls, and it assumes the velocity of the wall. As in this case, the arterial wall was assumed to be rigid and motionless, this condition induces a zero velocity next to the wall [56]. At the outlet, the gauge pressure was set to zero and there was no backflow.

When the blood was considered as Newtonian, the blood density was assumed to be equal to $1072.033\ kg/m^3$, and a constant viscosity of $0.00345\ kg/m \cdot s$. Similar properties had been applied by other authors [35,103]. Combined with these assumptions, an inlet flow rate constant and equal to 5 $\mathrm{ml/min}$ was defined.

For transient simulations, the blood was assumed as a non-Newtonian fluid and a realistic physiological inlet velocity profile was applied. The mean inlet velocity (V_m) of the cardiac cycle is defined as follows in Equation 11:

$$V_m(t) = \frac{\overline{V_m}}{a_0}\left\{a_0 + \sum_{i=1}^{5}\left[a_i cos(iwt) + \ b_i sin(iwt)\ \right]\right\} \tag{11}$$

Where $\overline{V_m}$ is the average velocity of a complete cycle (0.18 m/s), t is the time, w the angular frequency of the cardiac cycle, and a_i and b_i are parameters of the fitting model and they were obtained from Doutel et al. [35] for left coronary arteries (Table 13). A constant time step of 0.001 seconds and a residual target of 10^{-3} were considered. In FLUENT, this inlet condition was applied to the inlet of the artery by creating a user-defined function (UDF). This reflects the pulsatile nature of the human cardiac cycle (approximately 0.714 s), with the two distinct phases, systole and diastole, marked with a red dot (Figure 34).

Table 13. Pulsatile model parameters.

Parameters	Values	Parameters	Values
a_0	0.1308	b_1	-0.04866
a_1	0.05282	b_2	-0.0104
a_2	-0.00909	b_3	0.002598
a_3	-0.02733	b_4	0.02111
a_4	0.02509	b_5	-0.01372
a_5	-0.00268	w	8.483

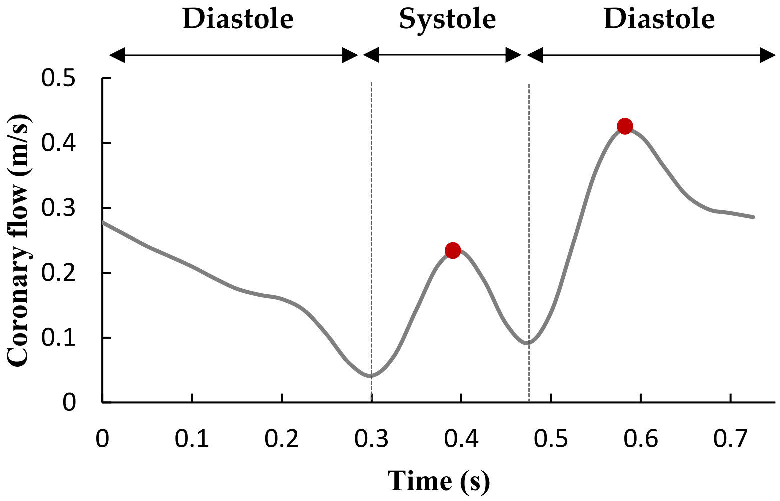

Figure 34. Coronary pulsatile velocity applied for computational fluid dynamic simulation at the coronary artery.

As previously mentioned, for the pulsatile non-Newtonian blood flow simulations, the selected model was the Carreau, since it is considered the most adequate to perform these simulations. The values of the respective parameters are represented in Table 14.

Table 14. Parameters values of the Carreau model, for blood [35,54,55].

Parameters	Value
$\boldsymbol{n}$	0.3568
$\boldsymbol{\lambda}$ (s)	3.313
$\boldsymbol{\mu_\infty}$ (Pa·s)	0.00345
$\boldsymbol{\mu_0}$ (Pa·s)	0.0560

6.4. 3D Printed Biomodels

After the geometry construction of the coronary arteries on Ansys, the models were converted in stereolithography (.STL) format file. The next step was to print a negative mold of the lumen geometry, which was obtained using an SLA printer (FabPro 1000 3D System) using a ProtoGry resin, and an FDM printer (Ultimaker 2+). Some characteristics of each printer are presented in Table 15.

Table 15. Overall characteristics of the Ultimaker 2+ and FabPro 1000 printers.

	Ultimaker 2+	**FabPro 1000 3D System**
Printer type	FDM	SLA
Time per model	Low (minutes)	High (hours)
Machine Cost (€)	2,368	4,485
Resolution	Low	High
Material cost (€/kg)	≈20	179
Mechanical properties	Low-High	Medium
Available materials	Thermoplastics	Photocurable resins

Initially, the FDM printer, whose manufacturing process is shown in Figure 35, was used with two different materials (PLA and ABS), aiming to compare and investigate if the differences between them influence significatively the results. PLA is biocompatible, biodegradable, it has low shrinkage and good printability. When compared to PLA, ABS has higher flexural strength, excellent ductility, and thermal stability. However, these features are not so important for the purpose concerned, since only a mold was manufactured [185,186,235,236]. Other characteristics of ABS and PLA filaments are represented in Table 16. The characteristics of the ProtoGry resin used in the SLA printer, are also presented.

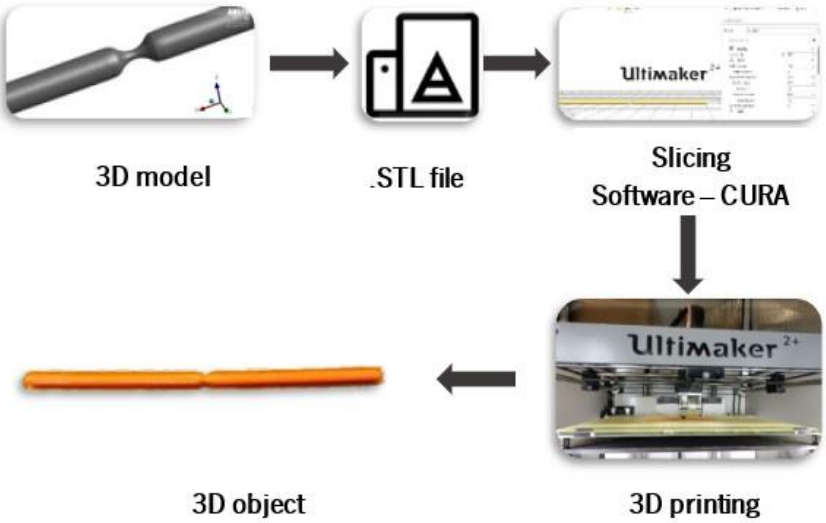

Figure 35. Schematic process carried out to obtain the final 3D object.

Table 16. Principal properties of the three different printable materials.

	ABS	**PLA**	**ProtoGry resin**
Environmentally friendly	No	Yes	No
Degradability	No	Yes	No
Glass Transition Temperature	105°C	65°C	–
Surface quality	Poor	Good	Very good
Cost (€/kg)	19.90	19.90	180.3
Melting Point	— (amorphous)	173 °C	177°C

To change the sample and 3D printing parameters in the FDM printer, the CURA software was used, designed by Ultimaker. Despite the several parameters in printing settings, only the most relevant are addressed in Table 17.

Table 17. Printing parameters applied for each material.

	Material			
	PLA	**ABS**	**PLA**	**ABS**
Nozzle diameter (mm)	0.4	0.4	0.25	0.25
Layer height (mm)	0.06	0.06	0.06	0.06
Print speed (mm/s)	50	45	30	30
Filament diameter (mm)	2.85	2.85	2.85	2.85
Infill (%)	22	22	22	22
Support material	None	None	None	None
Nozzle temperature (°C)	200	230	200	230
Build plate adhesion type	Skirt	Brim	Skirt	Brim
Build plate temperature (°C)	60	80	60	80
Time per model (min)	16	23	32	37

Regarding the nozzle diameter, Ultimaker 2+ is capable of working with different nozzles sizes: 0.25, 0.4, 0.6, and 0.8 mm. Firstly the 0.4 mm nozzle was used, which is the most common and then the same process was done with the 0.25 mm nozzle. Although the 0.25mm nozzle worked perfectly with the PLA filament, the same was not true when using ABS. The nozzle constantly clogged, and the repair process was time-consuming. For this reason, for this nozzle diameter, only the PLA was used.

The other parameter studied was the build plate adhesion type, which can be brim or skirt. The first one adds a single layer flat area around the base of the model which is attached to it, making the bottom surface area bigger. Thus, the model is better stuck to the build plate and there is less probability to the corners curl up. The second one is a line, not connected to the object, printed around it on the first layer. Thus, to understand the influence of this parameter, preliminary tests were made to conclude, which one build plate adhesion type, brim or skirt, allows better results. After the PLA printed models were obtained, it was observed that the removal process was significatively easier when using the skirt mode. Also, the finishing was better. For this reason, the remaining models were printed using this method. In turn, when using the ABS filament, the better results were obtained using the brim mode. Using the ABS filament with a skirt mode, the first layer does not stick well enough and starts warping, which is due to the material properties. The ABS has a high melting point and the tendency to shrink when cooling down fast is higher [183,237].

Another extremely important parameter, when printing, is the humidity of the air. This changes the proper functioning of the 3D printer. Consequently, many models were discarded, because the filament starts to fail, mainly when using the ABS filament.

Comparing the final products, it can be seen clearly that the PLA (Figure 36 (b)) samples tend to be shinier and smoother than ABS (Figure 36 (a)). However, when both thermoplastics are compared to the model printed with the ProtoGry resin (Figure 36 (c)), it is clearly seen that the latest model exhibits minimum surface roughness.

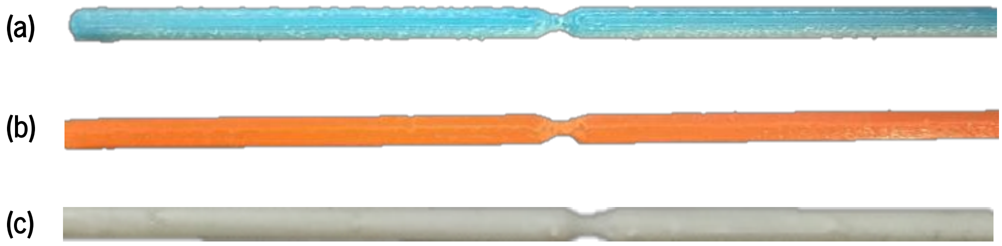

Figure 36. Biomodels printed using (a) ABS; (b) PLA and (c) ProtoGry resin.

Although this initial study was carried out and the PDMS casting technique was applied (Appendix A), it was not possible to perform detailed experimental tests on these models, due to some difficulties faced during preliminary tests. Firstly, both models printed with PLA and ABS showed very poor visualization results. The model that provided excellent results was the one obtained through stereolithography. However, some difficulties were found in the PDMS curing process and when tested experimentally, the blood analogue made the channel tarnished, making it impossible to carry out further tests.

For those reasons, all the experimental tests were performed in the Biofabics models. These were manufactured using stereolithography, however, the channel is automatically printed on a transparent rigid material (Figure 37).

Figure 37. Stenotic model fabricated by Biofabics.

Chapter 7

Hemodynamic Studies in Coronary Artery Models Manufactured by 3D Printing[17]

Abstract

Atherosclerosis is one of the leading causes of death worldwide. It is a chronic inflammatory disease of the arterial wall that progressively reduces the lumen size because of plaque formation. To understand this pathological process, several hemodynamic studies have been carried out, either experimentally or numerically. However, experimental studies have played an important role to validate numerical results. Recent advances in computer-aided design, medical imaging, and 3D printing technologies have provided a rapid and cost-efficient method to produce physical biomodels for flow visualization. As a manufacturing process, 3D printing techniques have attracted significant attention due to the low cost and potential to rapidly fabricate biomodels to perform flow hemodynamic studies.

In the present work, a study was performed using biomodels manufactured by 3D printing that mimic both healthy and stenotic coronary arteries with different degrees of stenosis (0%, 50% and 70%). Firstly, it was evaluated the influence of the printing resolution on flow visualization, and the results showed that, when comparing to 150 μm, the 100 μm resolution biomodel was the most adequate for performing the proposed experimental studies, presenting an arithmetic average roughness of 7.24 μm. Secondly, the effect of stenosis severity on velocity and flow behavior was studied. It was concluded that as the severity of stenosis increases, the velocity at the stenosis throat also increases. In addition to this, it was also observed a recirculation zone downstream the stenosis, when the diameter was reduced to 70%.

Keywords: atherosclerosis, hemodynamic, 3D printing, *in vitro*, biomodels, print resolution.

---

[17] Carvalho, V., Ribeiro,R., Costa, P., Teixeira, S., Lima, R., 2020. Hemodynamic studies in coronary artery models manufactured by 3D printing, International Conference Innovation in Engineering (ICIE), 2021, Guimarães, Portugal.

7.1. Introduction

Cardiovascular diseases (CVDs) remain the biggest cause of death worldwide, responsible for over 17.3 million deaths per year and the underlying disease process is known as atherosclerosis [30]. This is a complex disease characterized by fatty material deposition in the inner most layer of the arterial wall. These deposits cause the lumen to become narrow, affecting the blood flow behavior [30]. Given its significant negative socioeconomic impact, atherosclerosis has been intensively studied in the last decades. *In vivo* studies are of capital importance as they allow a direct observation of the physiological phenomena. However, these are expensive, it is hard to control and obtain detailed measurements of the flow behavior and sometimes the selected animal model does not completely represent the disease condition [78,96,238].

With recent advancements on microscopy, computational power and software, image analysis techniques, and additive manufacturing techniques, experimental flow studies have gained widespread attention [62,75,78,82,162,239]. In particular, 3D printing technologies have become an effective tool for rapidly producing artery phantoms with high-fidelity at low cost [162,240]. In the past few years, many researchers used these technologies to manufacture arterial biomodels, namely by means of inkjet-based printing [115], Fused Deposition Modelling (FDM) [78,112], Poly Jet [95], Binder jetting [112,121], Inkjet printing [121] and stereolithography (SLA) [96,103]. For instance, Geoghegan et al [121], used two different 3D printing technologies (Binder Jetting and InkJet) to manufacture rigid and flexible stenotic phantoms. In a study conducted by Doutel et al. [103], secondary flows were studied using 3D printed coronary artery biomodels by SLA technology. By using the same additive manufacturing technique, Costa et al.[96], studied arterial thrombosis in stenosed and healthy coronary arteries, employing biomodels fully printed with inlets, outlets and a box-like container. In another perspective, Lai et al. [241] combined SLA with a compliant photopolymer to produce vessel-like structures. Recently, Stepniak et al. [118] produced coronary biomodels with three different technologies (FDM, SLA and PolyJet) and concluded that SLA and Polyjet techniques are appropriate to manufacture arterial phantoms. As observed, SLA is a suitable technique for phantom production, particularly, due to its high resolution, which allows to obtain extremely smooth surfaces. In this technology, the models are manufactured layer-by-layer from a photocurable liquid resin and cured by exposure to light [108].

Despite extensive research work in this field, there is still a lack of knowledge regarding the influence of printing parameters in flow visualization and measurement. In this study, it was performed an experimental study that shows how the printing resolution can affect flow visualization. Moreover, the hemodynamic effects of atherosclerosis were studied, using both healthy and stenotic idealized coronary arteries.

7.2. Materials and Methods

7.2.1. Coronary Artery 3D Biomodels Design and Fabrication

The geometry employed in this study is a simplification of a 3D model of a coronary artery, although based on real data [228]. The online platform BIOFABICS TOOLBOX (www.biofabics-toolbox.com) was used to automatically generate the studied geometries, by employing its design tool number 3. The biomodels were custom-designed with a 24-well plate layout, 50 mm total channel length, 3 mm channel 1 diameter, 3 mm channel 2 diameter, 6 mm stenosis length, 0.5 mm base thickness, and a total device height of 4.5 mm (Figure 38). To capture the changes in flow behavior, the degrees of stenosis selected were 0%, 50%, and 70%. The first one represents the healthy case. On the other hand, the 50% model represents a moderate stenotic condition, while 70% represents the most severe case. After defining all parameters, the 3D biomodels were custom-manufactured (Biofabics, Porto, Portugal) at 100 μm and 150 μm resolutions.

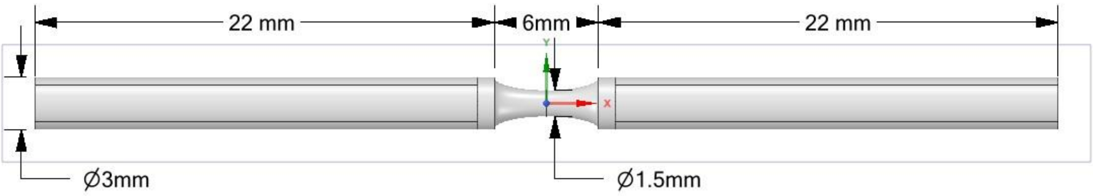

Figure 38. Dimensions of 50% stenosis model.

7.2.2. Experimental Setup for Roughness Measurements and Flow Characterization

Roughness measurements were performed in order to understand the influence of printing resolution in the flow visualizations. To evaluate the roughness of the biomodels, a surface profiler (Dektak® 150, Veeco) was used which is represented in Figure 39. Due to the difficulty of performing these measurements on circular surfaces, it was decided to print 3D cubes with the various resolutions employed.

Figure 39. Experimental setup for roughness measurements.

For the flow visualization, all experiments were conducted by using a high-speed video microscopy system (Figure 40). The main equipment of this system consists of an inverted microscope (IX71, OLYMPUS, Japan) and a high-speed camera (Fastcam SA3, Photron, USA). To impose a constant inlet flow rate was used a syringe pump (LEGATO® 100, USA), which was kept constant and equal to 5 $\mathrm{ml} \cdot \mathrm{min}^{-}1$.

The fluid selected as blood analogue was a dimethyl sulfoxide (DMSO)/water mixture (52%/48%-w/w), which is similar to blood in its viscosity and density. In suspension of the blood analogue fluid were used 40 μm monosized spherical microparticles, (CA 40, Spheromers®) at a concentration of 0.2 %.

Figure 40. Experimental setup used to control and visualize the flow.

7.2.3. Image Processing

To understand the diameter reduction effect on flow behavior, the video sequences captured by the high-speed camera were digitally processed using an image handling software ImageJ [200]. This is a tool frequently used to process and analyze images. In this study, it was used to perform the pre-treatment of the acquired frames, aiming to remove the noise and image artifacts. Firstly, it was selected the median projection type by means of the Z Project function in ImageJ. Secondly, it was used the image calculator tool to subtract the median from the original image. Finally, the maximum intensity projection was applied in order to obtain the images presented in this work.

To track the particles, the process previously described were applied together with a manual plugin (MTrackJ) of the image analysis software ImageJ. This plugin allows, not only to track moving particles at several image sequences, but also to measure the particle velocities.

Notice that, the regions of interest in this study are the stenotic and post stenotic region of the biomodel, however, for each case the frame rate selected was different. At the post-stenotic section, a sequence of 1000 frames per second were used and the same for the healthy model. Contrarily, to track the particles at the stenosis throat, the frame rate selected was higher (6000 frames per second). In this location, the velocity increases and so, to reliably track the particles it is necessary increase the frames number.

7.3. Results and Discussion

7.3.1. Printing Resolution Effect on Flow Visualization

Looking at Figure 41 (a) and (b), it is possible to observe the differences between the two printing resolutions, verifying that the best visualization is obtained in model (b) (100 μm). Smoother lines are observed in the second case, making it easier to visualize the flow.

To better support this observation, roughness measurements were performed in both models. One of the most widely used parameters is the arithmetic average roughness (Ra). This parameter represents the arithmetic mean of the absolute ordinate Z(x) within the sampling length [242]. The Ra parameter for the 150 μm and 100 μm model was 19.23 μm and 7.24 μm, respectively. These results demonstrate that the best biomodel was obtained with a printing resolution of 100 μm.

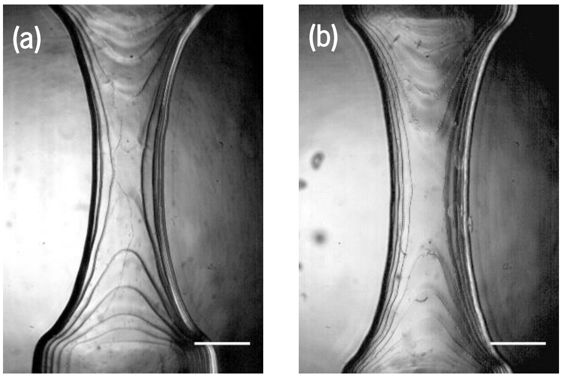

Figure 41. Images obtained with a printing resolution of (a) 150 μm and (b) 100 μm. Scale bar, 1mm.

For these reasons, the measurements were performed in the 100 μm model.

In summary, the choice of the printing resolution is a valuable step, as it can compromise the reliability of the experimental results. Without quality images, it is difficult to analyze the flow behavior and to accurately perform the particle tracking.

7.3.2. Velocity Measurements

The presence of plaques in the coronary artery is responsible for obstructing blood flow to the myocardium, consequently affecting the flow velocity. Because of this, the velocities were evaluated quantitatively in the healthy model and in the stenotic section of the diseased models. For each case, several particles were tracked, in order to ensure the accuracy of the measurements (Figure 42). The results effectively show the influence of diameter reduction on velocity. As expected, comparing the measured velocities in the healthy model with the remaining, it can be observed the increasing velocity as the severity of stenosis increases, due to the reduction in the arterial area.

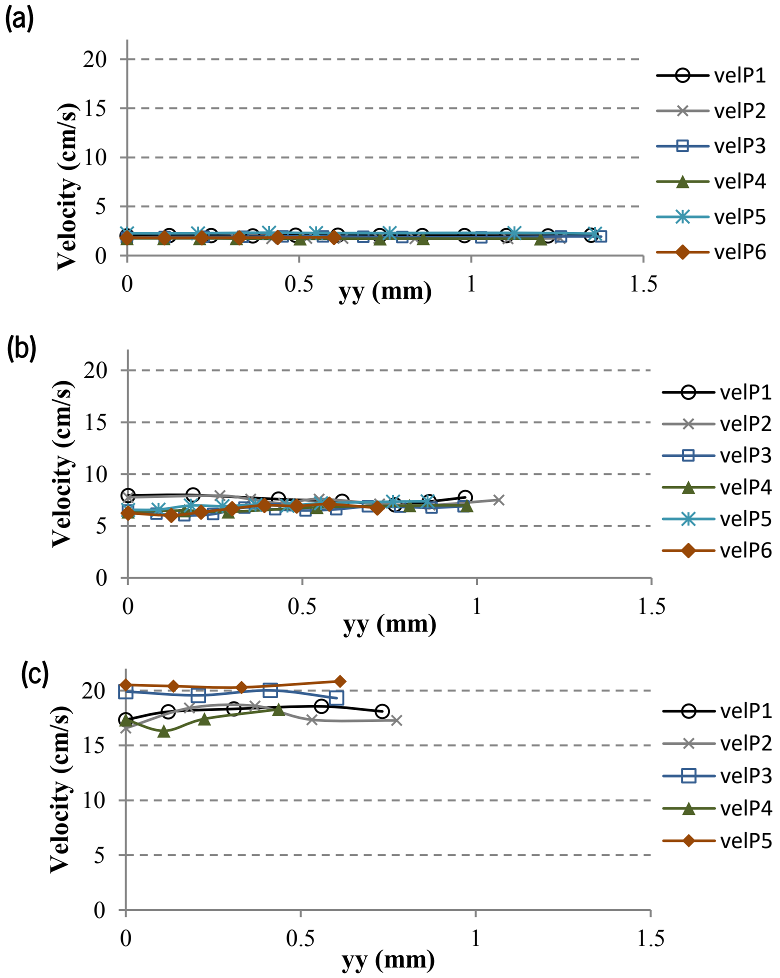

Figure 42. Particle velocity measurements for (a) healthy model; (b) 50% stenosis and (c) 70% of stenosis.

One aspect that should be highlighted is the irregularities of the different particles trajectories performed for each case. For the healthy model, the measured velocities were practically the same. However, for the 50% and 70% model, it was detected some oscillations at the measurements of each particle. Especially for the severe model (70%), those variations were found to be the highest. This might be due to the extremely high velocities of the particles flowing in this region and some possible measurement errors due to the limitations of our high-speed video camera. The tracking of the particles is extremely difficult to perform at high flow rates and consequently, the velocity error may increase [202].

Through the previous results, the average velocity was calculated for each particle and the results are shown in Figure 43. The lowest values were obtained for the healthy model (1.92 cm/s). In contrast, when the diameter reduces 50% and 70%, the velocities are significatively higher, and the average value was approximately 6.98 cm/s and 18.72 cm/s, respectively.

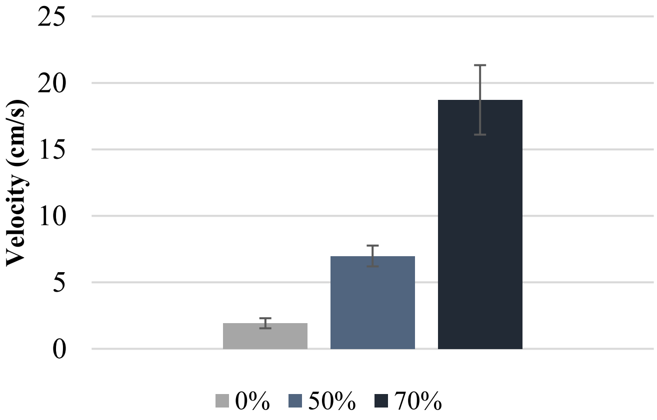

Figure 43. Average velocity measured for each stenosis degree. The measurements are expressed as the mean ± standard deviation according to a t-test analysis at 95% confidence interval.

7.3.3. Effect of Stenosis Degree on Flow Behavior

Figure 44 and Figure 45 show the images obtained by applying Z Project maximum intensity to all images of a movie. Figure 44 represents the healthy model and the alignment of the particles within the flow was observed. On the other hand, the effect of stenosis on hemodynamics is shown in Figure 45 (a) and (b). Similarly, to the healthy model, in the 50% stenosis, there is no recirculation and the fluid flows in a laminar way (Figure 45 (a)). When the degree of stenosis reaches 70% (Figure 45 (b)), there is a significative recirculation zone at the post-stenotic section. This clearly shows the effect of stenosis severity on changing the flow behavior. This phenomenon may be explained by the significative increase in velocity observed at the stenotic section of the 70% model. In contrast, when the diameter reduces 50%, the velocities at the throat are not high enough to cause these changes in flow.

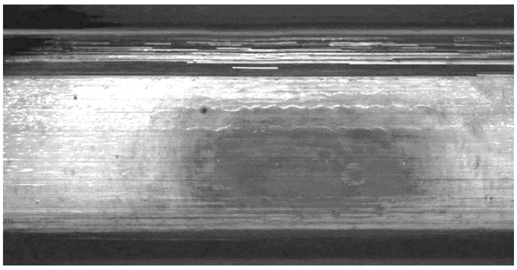

Figure 44. Z Project maximum intensity image of the healthy model.

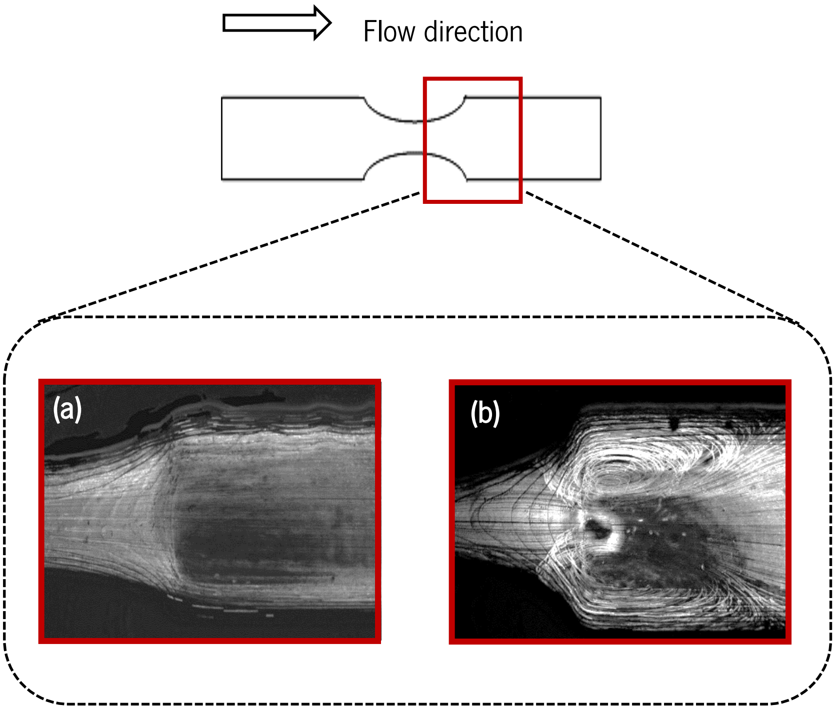

Figure 45. Z Project maximum intensity image: (a) 50% stenosis (b) 70% stenosis.

7.4. Conclusions

The present study shows flow measurements and visualizations of idealized coronary arteries with atherosclerotic plaques. The results acquired in this study shows effectively that the printing resolution affects the flow visualization and reveals the importance of this parameter when 3D printing technologies are used to obtain biomodels for experimental flow studies. In addition, some changes in the flow behavior were clearly observed. For example, it was observed the formation of recirculations immediately at downstream of the stenosis when a diameter reduction of 70% was reached. Comparing all the obtained results, it is clear that diameter reduction has a significant impact on the velocities and flow behaviors. The study of these phenomena is extremely important, helping not only to better understand what happens in physical models but also to validate and improve numerical models.

7.5. Acknowledgements

The authors acknowledge the financial support provided by Fundação para a Ciência e a Tecnologia (FCT), through the projects UIDB/04077/2020, UIDB/00319/2020, and UIDB/04436/2020, NORTE-01-0145-FEDER-029394 and NORTE-01-0145-FEDER-030171, funded by COMPETE2020, NORTE 2020, PORTUGAL 2020 and FEDER. This project has received funding from the European Union's Horizon 2020 research and innovation programme under the Marie Sklodowska-Curie grant agreement No 798014. This project has received funding from the European Union's Horizon 2020 research and innovation programme under grant agreement No 828835.

Chapter 8

3D Printed Biomodels for Flow Visualization in Stenotic Vessels: An Experimental and Numerical study[18]

Abstract

Atherosclerosis is one of the most serious and common forms of cardiovascular diseases and a major cause of death and disability worldwide, leading to acute cardiovascular events and chronic injuries. It is a multifactorial and complex disease, that promoted several hemodynamic studies, either *in vitro*, *in vivo* or *in silico*. Although *in vivo* studies represent more accurately the physiological conditions, *in vitro* experiments are more reliable to control several physiological variables and the most adequate way to validate numerical flow studies. Here, a hemodynamic study in an idealized stenotic and healthy coronary artery, using both numerical and *in vitro* approaches, by means of computational fluid dynamics (CFD) simulations and high-speed video microscopy technique, is presented. The biomodels used to perform the experimental studies were obtained using stereolithography 3D printing technology, which has been considered a suitable fabrication method and a cost-effective way to produce 3D *in vitro* biomodels. By varying the print resolution, it was concluded that the 50 μm biomodel was the most adequate to perform flow visualizations and velocity measurements, presenting the best roughness results (Ra=1.8 μm). In general, the flow experimental results obtained in this study have validated the numerical data of the blood flow, by showing a recirculation zone in both cases when the diameter reduction has reached 60%.

Keywords: atherosclerosis; *in vitro* biomodels; CFD; 3D printing; stereolithography; blood flow; blood analogues; hemodynamics

---

[18] Carvalho, V.,Rodrigues, N., Ribeiro,R., Costa, P., Teixeira, S., Lima, R., 2020. 3D Printed Biomodels for Flow Visualization in Stenotic Vessels: An Experimental and Numerical study. Micromachines Journal, under review.

8.1. Introduction

Atherosclerosis is considered the pathological basis of several cardiovascular diseases and the leading cause of death worldwide, originating over 20 million deaths every year. It is a silent and progressive disorder characterized by abnormal lipid deposition within the intima and commonly affects large and medium-sized arteries, like coronary arteries [2,29].

Given the clinical importance of this disease worldwide, hemodynamics research has increased exponentially. *In vivo* experimental methods provide the most realistic physiological data and remain essential to establish an adequate understanding of basic biophysical phenomena that happen *in vivo*. However, even performing these studies in animal models, human physiology or human disease is not fully recapitulated. Moreover, in these types of experiments, the measurements oftentimes are not accurate, are expensive, have low reproducibility, and have ethical issues associated [78,79,96,99]. Therefore, over the years, engineered *in vitro* biomodels have gained widespread attention and have been developed to overcome those limitations. Moreover, these are often used to validate numerical studies and to complement and confirm results from *in vivo* experiments [75]. On the other hand, numerical hemodynamic studies can be an auxiliary tool to investigate such arterial diseases, offering advantages over experimental analysis, since they are faster, the construction of more realistic virtual models becomes more flexible and they reduce the lead times and costs of new designs and developments. Although experimental and numerical methods are important by themselves, these studies should be compared to verify the accuracy of the results and thus validated [220,221].

The flow dynamics of stenotic arteries have been subjected to extensive studies with early *in vitro* [67,205] and *in silico* studies [204,243] and there has been continuously growing interest to understand the blood flow behavior in the atherosclerosis condition, due to its serious impact on human life. An important geometric factor to the local hemodynamics is the shape of the stenosis. Some experimental and numerical studies apply idealized stenosis shapes [99,132,137,244]. Other studies make use of patient-specific geometries based on medical images [35,96,138,245]. Kefayati et al. studied numerically and experimentally, the effect of stenosis severity, plaque eccentricity and ulceration on turbulence intensity [14], and on shear stresses measured *in vitro* [133]. In another study, the authors analyzed the transitional flow [102], using always idealized carotid models. Similar studies were conducted by DiCarlo et al. [135,136]. Another interesting study that can be highlighted was undertaken by Costa et al. [96], using a patient-specific geometry of a coronary artery with a shape similar to the one presented here. By combining Stereolithography (SLA) 3D printing and computed tomography angiography (CTA) data, they obtained a 3D biomodel and performed both *in vitro* and *in silico* studies of the flow through healthy and stenotic arteries. In a recent study, Stepniak et al. [118] studied the lipid-rich plaque in stenotic coronary artery phantoms using three different 3D printing technologies (Fused Deposition Modeling, SLA and PolyJet).

Despite the variety of ways to produce arterial phantoms for flow visualization, 3D printing technologies have become popular due to its capability to fabricate fully 3D structures, that closely mimic the shape of human blood vessels [246,247]. There are different 3D printing methods that have been used in this field, such as Fused Deposition Modelling [78,105,112,118,162], Inkjet [115], Poly Jet [95,118] and Binder jetting [112]. In addition to those methods, a suitable technique to fabricate those vessel models is SLA, since it can reach very high printing resolutions and accuracy, well-defined details, slightly visible layer lines and an extremely smooth surface finish. Notice that these characteristics play an important role, aiding the visualization process during experimental studies. Briefly, in this technique the models are manufactured layer by layer, using a photocurable liquid resin that is hardened by applying a low-power ultraviolet (UV) laser, a process called photopolymerization [96,108,182,185].

After the fabrication process, *in vitro* velocity fields of blood flow can be measured using several techniques [35,80,85,86,115,163,248], however, in the present study, blood flow measurements and visualizations were performed by using a high-speed video microscopy system.

In the last decades, many *in vitro* studies have been conducted, however, none of them considered the influence of roughness on the flow visualization. The present paper shows the influence of this parameter on visualization and the effect of stenosis severity on hemodynamics. Using numerical and experimental approaches, it is evaluated five degrees of stenosis (DOS) seen in human arteries, in addition to a healthy model, fabricated by stereolithography 3D printing technique.

8.2. Materials and Methods

8.2.1. Coronary Artery 3D Biomodels Design and Fabrication

The 3D biomodels were custom-designed using the online platform BIOFABICS TOOLBOX (www.biofabics-toolbox.com), and custom-manufactured using a rigid material (Biofabics, Porto, Portugal) at printing resolutions of 50, 100 and 150 μm. The biomodels were designed with tool number 3 of the BIOFABICS TOOLBOX, employing as parameters a 24 well plate layout, a 50 mm total channel length, 3 mm channel 1 diameter, 3 mm channel 2 diameter, 6 mm stenosis length, 0.5 mm base thickness and a total device height of 5.5 mm. The DOS selected for this study were 0%, 50%, 60%, 70% and 80%, in order to capture the changes in flow behavior when the severity of stenosis increases.

The shape of the artery is a full cylindrical tube with a circular cross-section and an axisymmetric blockage (Figure 46). The selected diameter (3 mm) was based on the literature [40,41] and the length of the stenosis was defined as twice the normal diameter, an assumption applied by several researchers [54,230–232]. In addition, the length of the inlet zone (22 mm) was selected to ensure the creation of a fully developed inlet flow.

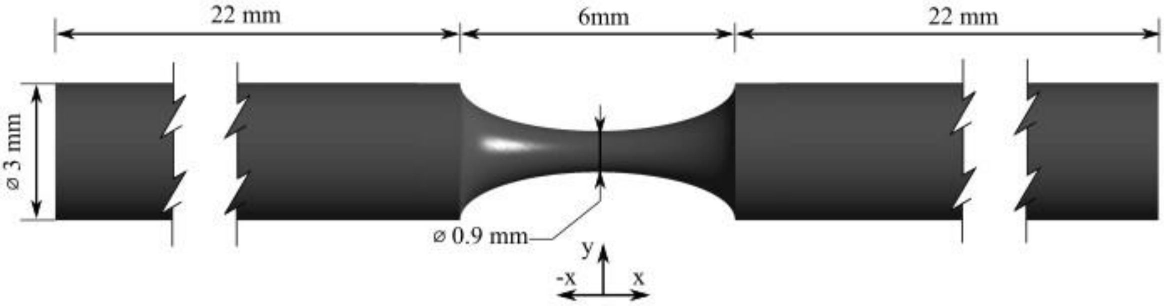

Figure 46. Dimensions of 70% stenosis model.

The DOS is estimated by comparing the minimum diameter of the vessel at the lesion site to the diameter of the straight section without any stenosis (Equation 12). It can be defined as minimal, moderate and severe. Minimal if the narrowing is less than 50%, moderate between 50% and 70%, and severe or significant for a diameter reduction of 70% or more [234].

$$stenosis\ (\%) = \left(1 - \frac{d_{stenosis}}{d_{straight}}\right) \times 100 \tag{12}$$

8.2.2. Blood Analogue Fluid and Flow Rate

Recently, the use of blood analogues has been increasing due to the difficulties associated with the manipulation of real blood *in vitro* because of ethical, economical or hazardous issues [146,169,181].

In this study, the fluid selected as blood analogue was a dimethyl sulfoxide (DMSO)/water mixture (52%/48%-w/w), with properties similar to blood ($\mu = 0.003153426\ \mathrm{Pa \cdot s}$ and $\rho = 1072.033\ \mathrm{kg \cdot m^{-3}}$), where μ, is the viscosity and ρ, is the density of the fluid. The density of the biofluid was measured using a density meter (DMA 5000M, Anton Paar®) [197]. Moreover, the refractive index of this mixture matches the refractive index of the biomodels, eliminating the visual distortion given by the curvature of the walls. By using a syringe pump the infusion flow rate was kept constant and equal to 5 $\mathrm{ml/min}$. The same flow rate was used to perform the numerical simulations.

8.2.3. Experimental Setup for Roughness Measurements and Flow Characterization

To understand the influence of the print resolution in flow visualization, roughness measurements were performed using a surface profiler (Dektak® 150, Veeco) (Figure 47). Considering the difficulty and inaccuracy of the roughness measurements on circular surfaces, cubes printed with the respective resolutions were used to make the comparison.

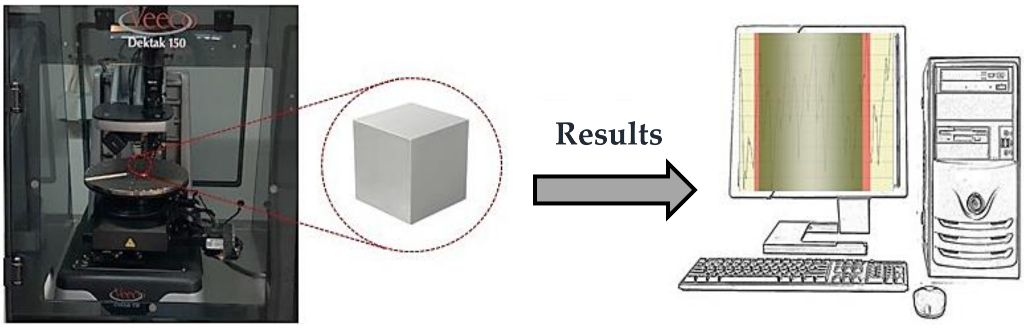

Figure 47. Experimental setup for roughness measurements.

In Figure 48, the experimental setup used to perform the flow visualization is represented. This was composed by an inverted microscope (IX71, OLYMPUS, Tokyo, Japan) combined with a high-speed video camera (Fastcam SA3, Photron, USA) and the objective lens used in this study has a magnification of 2.5×. To control and impose steady flow rates through the channels of the biomodel, a syringe pump (LEGATO® 100, USA) was used. All images were captured and recorded by a high-speed video camera (Fastcam SA3, Photron, USA). The microparticles used in suspension of the blood analogue fluid were 40 µm monosized spherical tracer particles (CA 40, Spheromers®) at a concentration of 0.2%.

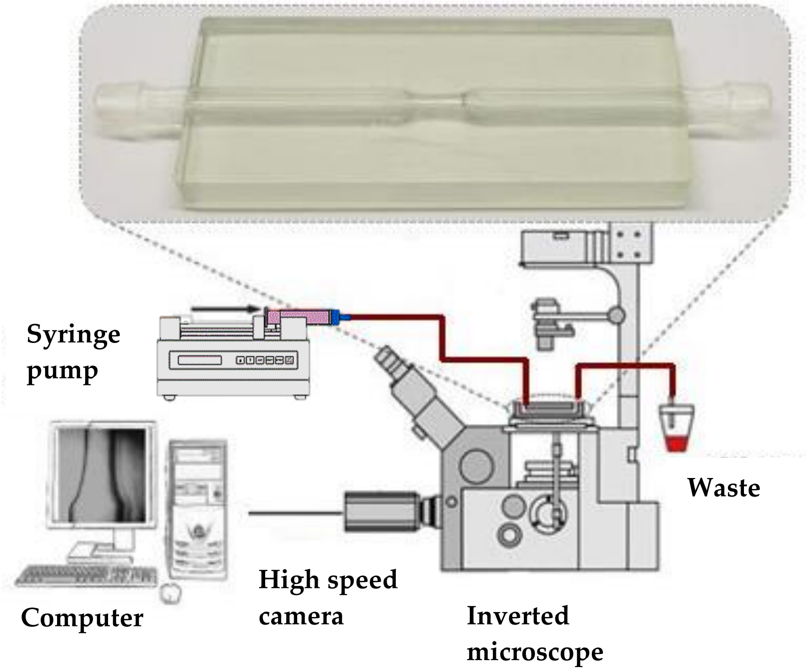

Figure 48. Experimental equipment used to control and visualize the flow of the blood analogue.

8.2.4. Numerical Approach

Numerical simulations were performed in the CFD package ANSYS Fluent (version R2), which utilizes the finite volume methodology. In addition, the semi-implicit method for pressure linked equations (SIMPLE) scheme was used to solve the governing equations.

For each model, a hybrid mesh was generated with tetrahedral cells with inflation layers in the stenosis zone and hexagonal cells with a bias factor in the remaining geometry. The inflation and bias factor were applied, in order to improve the accuracy of the computed Wall Shear Stresses (WSS). Moreover, several mesh tests were performed to guarantee a grid-independent solution. The mesh that combines accuracy and lower computation time for the 70% stenosis case has 498 974 elements (Figure 49). For the remaining models, similar meshes were performed.

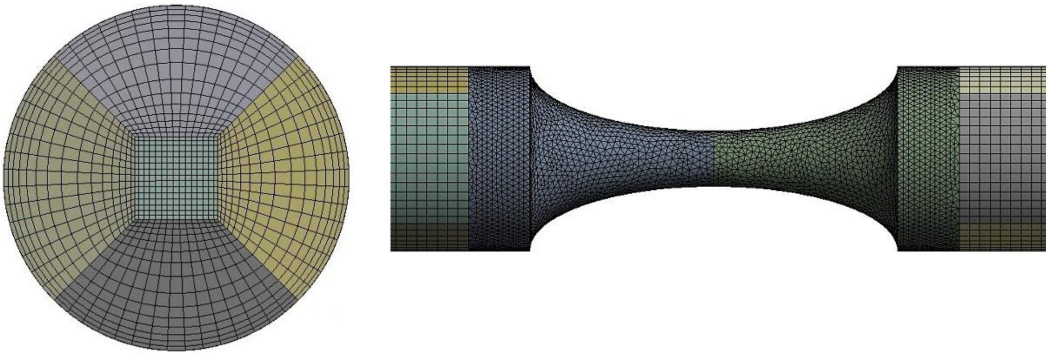
(a) (b)

Figure 49. Hybrid mesh generated for the 70% model: (a) inlet view; (b) front view.

Although in small arteries and capillaries the blood exhibits non-Newtonian behavior, in vessels with a diameter superior to 1 mm, such as the coronary arteries, the non-Newtonian behavior can be neglected because of the predominant high-shear rates [25,103,249,250]. In this study, the blood is considered as incompressible, homogeneous and a Newtonian fluid. The no-slip boundary condition was applied at the artery walls, which were assumed as rigid and motionless. The outlet gauge pressure was set to zero and there was no backflow. Although the blood flow in the coronary arteries is time-dependent, the current investigation first simplifies it to a steady flow condition, with constant inputs, assuming a laminar regime.

Under these assumptions, three-dimensional blood flow through an artery with stenosis can be described by the steady continuity and Navier-Stokes equations (Equation 13 and 14),

$$\nabla \cdot \vec{u} = 0 \tag{13}$$

$$\rho\left(\frac{\partial \vec{u}}{\partial t} + \vec{u} \cdot \nabla\right) = -\nabla p + \mu \nabla^2 \vec{u} \tag{14}$$

Where $\vec{u}$ is the velocity vector, p is the static pressure, ρ is the fluid density, and μ the dynamic viscosity.

8.2.5. Image Processing

The images were obtained essentially in the post stenotic section of the biomodel, by using a frame rate of 1000 frames/second. All sets of frames were analyzed using the Z Project method from the ImageJ software [200]. The number of analyzed frames was about 800 for each movie and the recorded sequence of images was replaced by an image that represents the minimum or maximum intensity in each pixel. By using this methodology, it is possible to observe clearly the flow behavior.

To perform the particles' velocity measurements, the manual MtrackJ plugin was used. This is an ImageJ plugin that allows the tracking of moving particles and to calculate their velocities automatically.

Moreover, to estimate the difference between the experimental results and the numerical values, Equation 15 was used:

$$\%\, error = \frac{|Experimental\ value - Numerical\ value|}{Numerical\ value} \times 100 \tag{15}$$

8.3. Results and Discussion

8.3.1. Printing Resolution Effect

To understand the influence of the print resolution in flow visualization, three different cases were tested (50 μm, 100 μm and 150 μm). Initially, it was analyzed in a qualitative way observing the flow through the microscope. As can be seen in Figure 50, there is a significant improvement when the print resolution is reduced to 50 μm. In Figure 50 (a) and (b), there are accentuated lines that affect the flow visualization, as well as particle tracking.

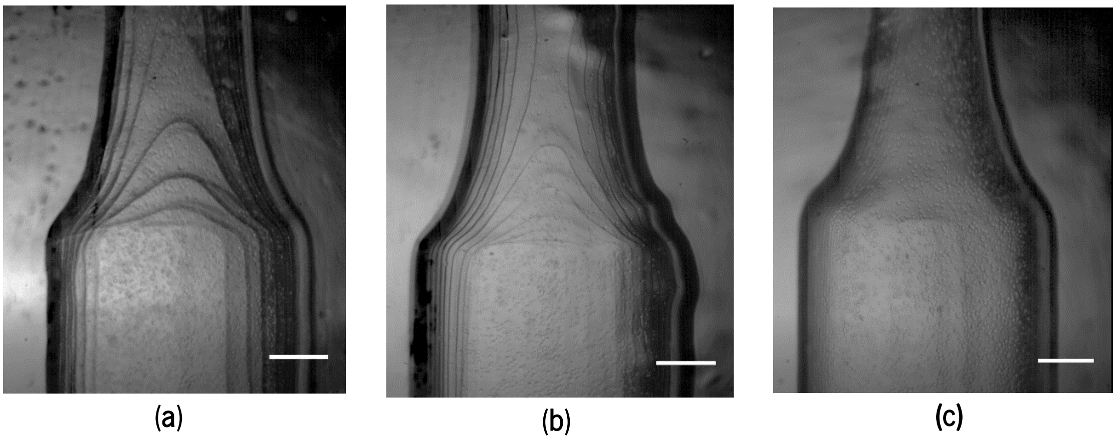
(a) (b) (c)

Figure 50. Images obtained for each printing resolution: (a) 150 μm. Scale bar, 1 mm. (b) 100 μm. Scale bar, 1 mm. (c) 50 μm. Scale bar, 1 mm.

To better understand the impact of the printing resolution in the assessment of the experimental results, additional images from ImageJ were obtained (Figure 51). Those images were recorded before the application of the Z project tool, which can be used to track the trace particles. Through the analysis of the results, it is possible to observe the difficulty to track the trace particles near the walls for the printing resolutions of 100 and 150 μm (Figure 51 (a) and (b)). Between these two biomodels, there is almost no difference. However, in comparison to the 50 μm biomodel, the differences are quite significant. For instance, by using images obtained with the 50 μm biomodel (Figure 51(c)), the tracer particles can be tracked without almost any influence of the channel wall, while in the remaining cases, the images are too noisy near the walls which promote the generation of large errors when tracking those particles. These results are extremely relevant in flow experiments as it essential to obtain high-quality flow images near the walls to obtain accurate *in vitro* results, namely in WSS and velocity measurements.

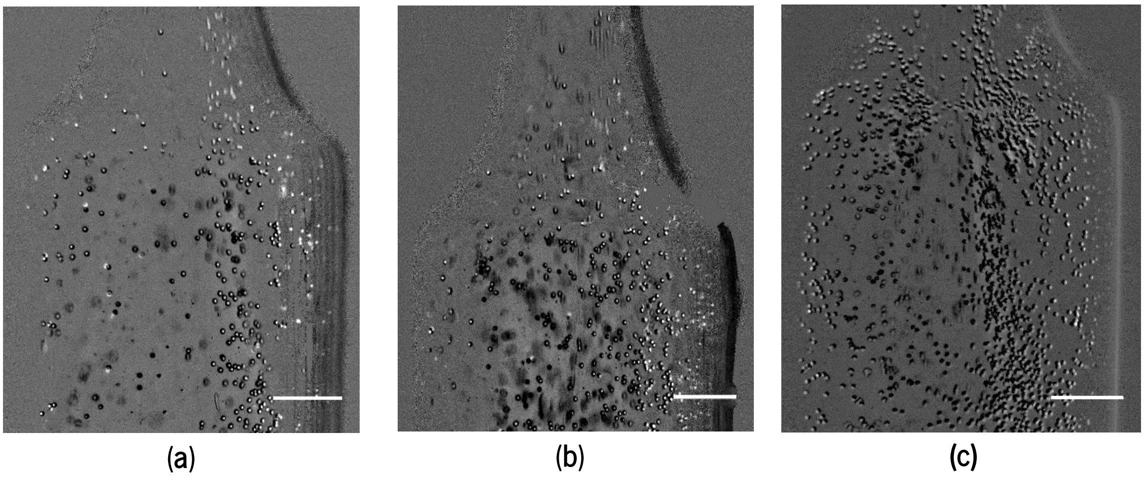
(a) (b) (c)

Figure 51. Images with tracer particles obtained by the high-speed camera: (a) 150 μm. Scale bar, 1 mm. (b) 100 μm. Scale bar, 1 mm. (c) 50 μm. Scale bar, 1 mm.

Following the previous results, it was quantitatively evaluated the effect of the printing resolution in the experimental measurements near the wall, where the results are most affected by this parameter. For this purpose, the mean particles' velocity was measured experimentally and numerically near the wall in the post stenotic section of the 50% stenotic model. Analyzing the results depicted in Figure 52, it can be seen that the model with values closest to the numerical results is the 50 μm model. While the 150 μm model presents the worst results, where the velocities measured experimentally are much lower than those predicted numerically. The 100 μm model presents results between the two models mentioned above, but it is significatively better than the 150 μm model.

The error associated with the measurements was also calculated, and as expected, the measurements in the 50 μm model presented the lowest error of about 10%. The measurements in the 100 μm and 150 μm presented higher errors, approximately 28% and 50%, respectively. Considering these results, it can be concluded that the 50 μm and 100 μm models are the most adequate to perform the experimental studies with more reliability, being the 50 μm the best one.

Through the analysis of these results, it is possible to verify the direct influence of printing resolution on the quality and reliability of particles' velocity measurements near the wall.

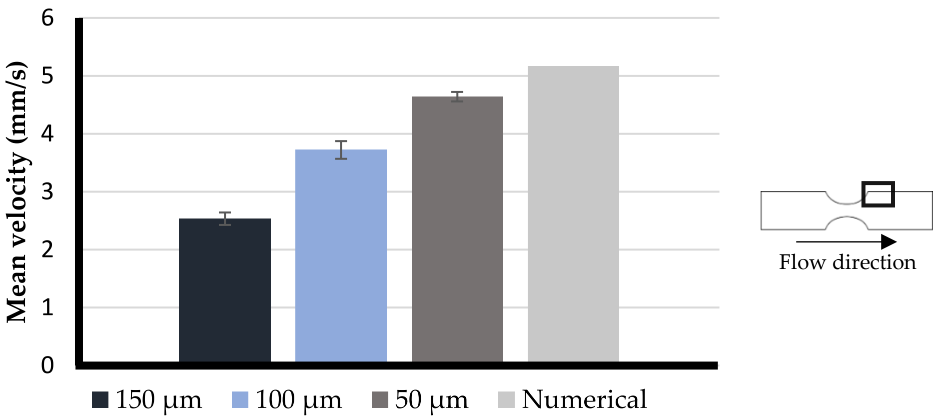

Figure 52. Comparison between the mean velocities measured experimentally near the wall at each model with the mean velocity estimated numerically. The experimental measurements are expressed as the mean ± standard deviation according to a t-test analysis at 95% confidence interval.

Additionally, roughness measurements were carried out to verify the previous observations. For that, roughness measurements were performed. The main roughness parameter is the average roughness (Ra). This parameter evaluates the average standard deviation of the heights (peaks and valleys) in a scanned profile to compute the degree of roughness [251,252].

To perform the roughness tests, different cubes were printed with three different resolutions (three measurements for each case). Figure 53 shows the average Ra values obtained per each resolution proving that, effectively, this parameter influences the models' roughness. The higher value is measured in the 150 μm model, with an average Ra of approximately 19.53 μm. In turn, the 100 μm model has a significantly lower roughness (7.35 μm). However, the best model is the one printed with the lowest resolution (50 μm), presenting an average Ra of 1.78 μm.

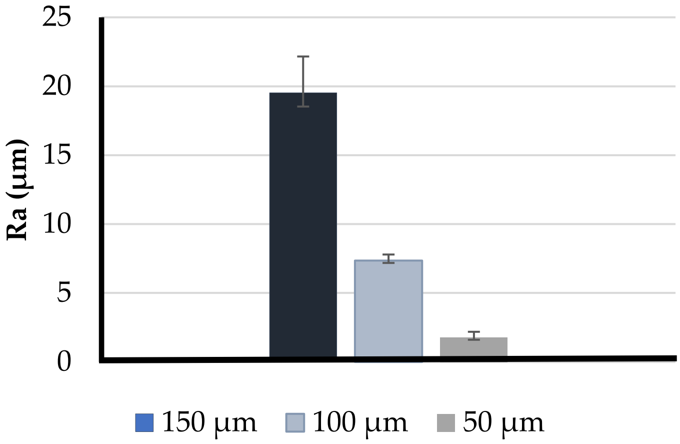

Figure 53. Comparison between the roughness parameter, Ra, at three different print resolutions. The measurements are expressed as the mean ± standard deviation according to a t-test analysis at 95% confidence interval.

From these results, it can be concluded that the best surface roughness can be achieved with a print resolution of 50 µm and so, the remaining tests were performed in that model.

8.3.2. Velocity Profiles and Wall Shear Stress Evaluation

The effect of stenosis severity on blood velocity profiles at different sites in the artery for different DOS is depicted in Figure 54. Figure 54 (a) shows that the velocity profile is fully developed at the beginning of the channel and is not significantly affected by the DOS. It is seen only a slight difference in the maximum velocity between the healthy model and the rest. Whereas, in Figure 54 (b), it can be clearly noticed that at the stenosis throat for all DOS, the velocity increases reaching its maximum. As the throat diameter reduces, the velocity increases and the highest speed is achieved with a DOS of 80% (0.50 m/s). Figure 54 (c) and (d) shows the corresponding velocity profiles at two different locations in the downstream region of stenosis. In Figure 54 (c) the velocity profiles are a little disturbed and fluctuating due to the presence of secondary recirculating flows for some models. The remaining velocity profiles do not display that behavior, showing absence or reduced recirculation. In Figure 54 (d) the flow is stabilized again, although in the DOS of 80% the velocity is slightly higher.

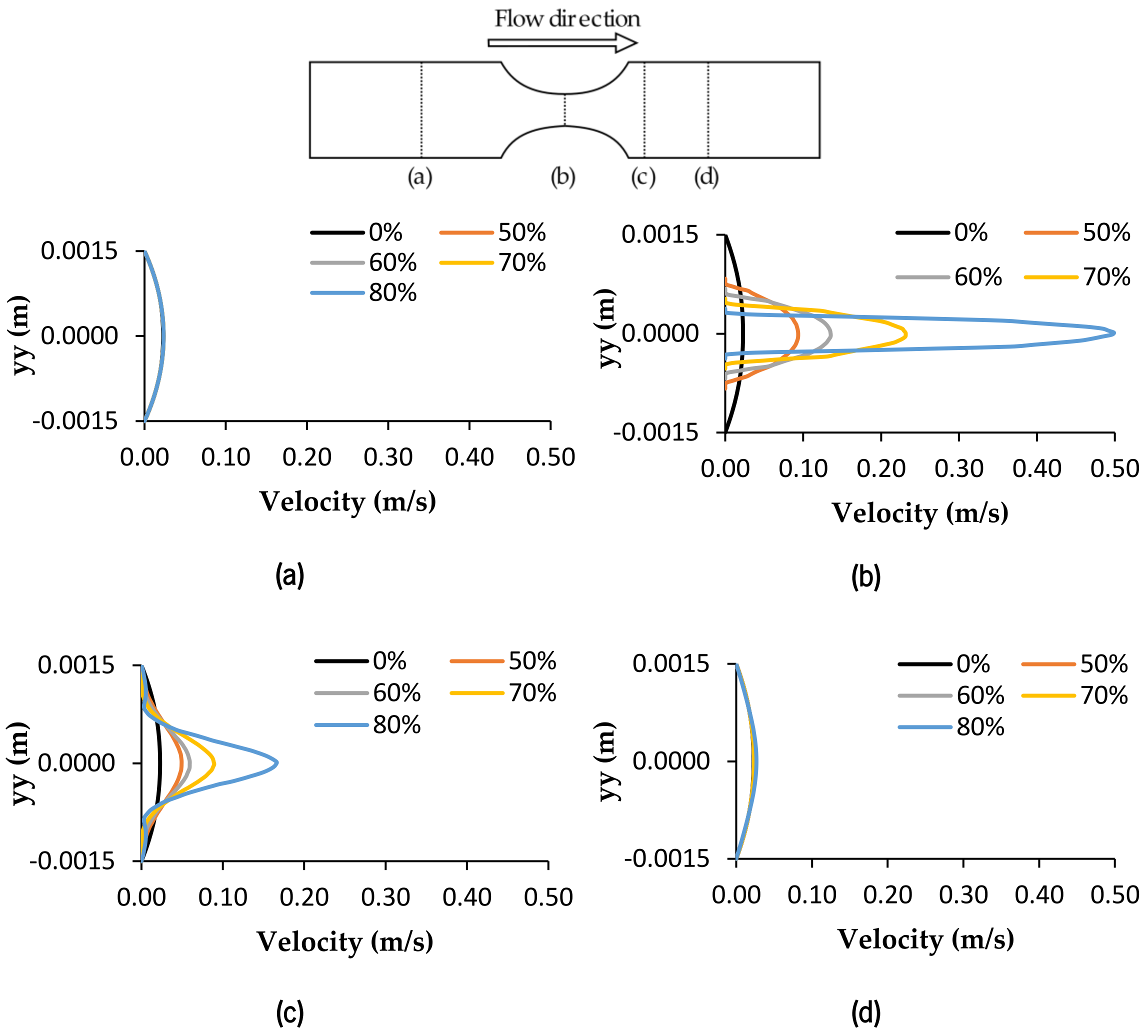

Figure 54. Comparison of velocity profiles at different axial positions for the different degrees of stenosis.

Table 18 shows the Reynolds number (Re) ($\rho U d/\mu$) in the stenotic region for each degree of stenosis. As the stenosis severity increases, the Re also increases, which is explained by the velocity increase in that region. Additionally, as can be observed, the maximum Re is, approximately, 102. Therefore, the laminar flow assumption is the most adequate in the present simulation.

Table 18. Reynolds number at the stenotic section for the different degrees of stenosis.

Stenosis degree	Reynolds
0%	23
50%	45
60%	55
70%	71
80%	102

WSS plays an important role in the development of various vascular disorders, including atherosclerosis [39]. This is a key parameter in the hemodynamic analysis because of its direct relationship to the development of cardiovascular disease and atherosclerosis in general. High WSS is indicated as a contributor to the rupture of the atherosclerotic plaque in human coronary artery [212]. Whereas, low WSS is associated with plaque progression in diseased human coronary arteries [41]. For a Newtonian fluid, the applied shear stress (τ_w) is proportional to the resulting deformation rate ($\dot{\gamma}$) and the viscosity is constant (Equation 16):

$$\tau_w = \mu \frac{\partial u}{\partial y} = \mu \dot{\gamma} \tag{16}$$

The effect of stenosis on WSS is depicted in Figure 55. The maximum WSS is observed at the throat stenosis and its value increases with the degree of stenosis. This happens because the artery diameter reduction causes higher velocities in the stenosis throat and, consequently, the WSS also increases. Similarly to the previous results, it can be verified that the maximum WSS is reached for a DOS of 80% being, approximately, 14.64 Pa. For the healthy model, WSS is almost constant at the value of 0.10 Pa.

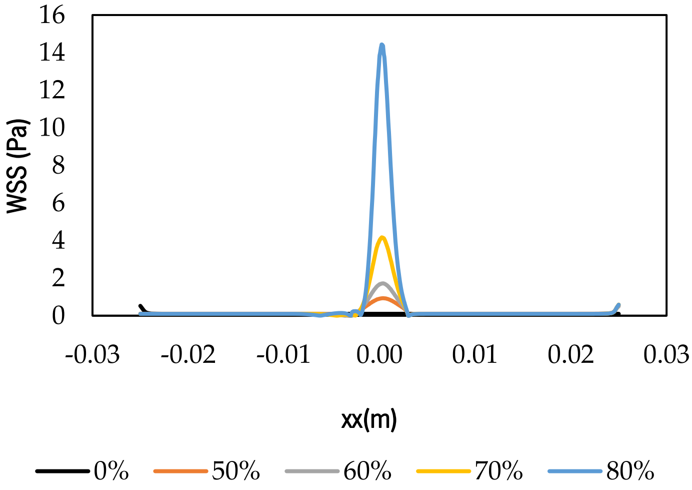

Figure 55.WSS distribution along the vessel wall.

For the 50%, 60% and 70% of stenosis, WSS values of 0.86, 1.73 and 4.19 Pa are observed at the throat, respectively. In addition, it can be noticed that there is a sudden increase in the WSS from DOS 70% to 80%, showing that the second case is already extreme, possibly leading to acute myocardial infarction.

8.3.3. Velocity Fields and Flow Visualizations

To evaluate the flow behavior, the velocity vectors obtained by CFD simulation and the respective minimum intensity experimental images were compared and depicted in Figure 56.

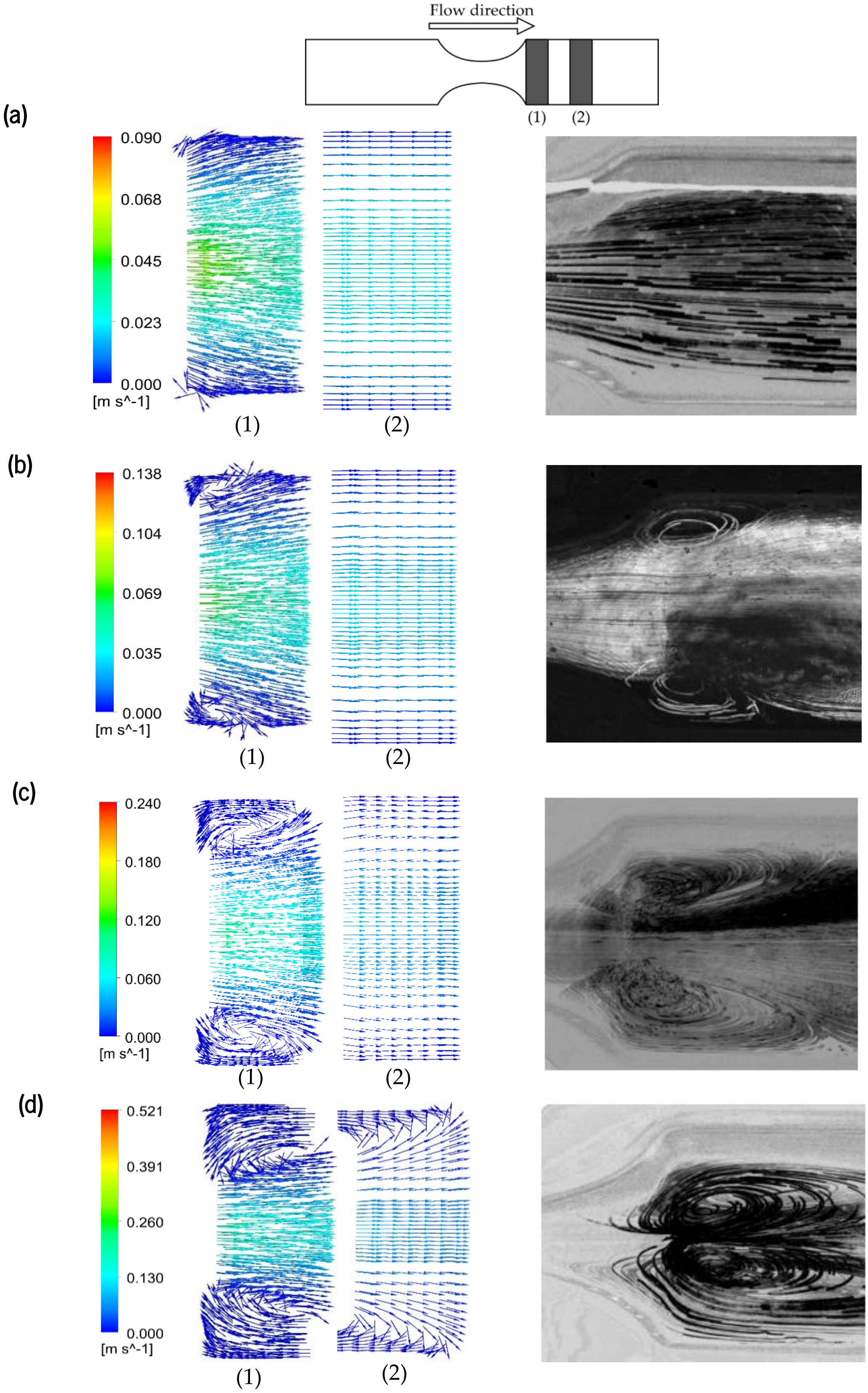

Figure 56. Images for different degrees of stenosis: (a) 50%; (b) 60%; (c) 70% and (d) 80%. Left: velocity vectors; Right: Z project image.

Notice that the vectors were normalized to better visualize what is happening in the flow and they were studied in two locations downside of the stenosis. In general, the numerical data describes well the experimental results. However, looking at (a) left, there are some vectors in the opposite direction to the flow, which are not seen in the image obtained experimentally (right). This may be due to the numerical instability in the pointed area of the geometry. On the other hand, recirculation can occur experimentally and be so reduced that it is not captured with the experimental setup adopted. In (b) both results are in close agreement, and a small recirculation zone appears. In the 70% stenosis case ((c)), the results are also similar, but the length of recirculation is slightly higher experimentally than numerically. Another aspect that should be highlighted is the difference in the recirculation behavior numerically and experimentally when the diameter reduces 80% ((d)). The recirculation length is clearly in agreement between the two methods. However, experimentally, the recirculation spreads to the center of the biomodel and also near of the stenotic section, which does not happen numerically. These are small details that prove the importance of *in vitro* studies to complement and validate numerical studies.

8.4. Conclusions

The effect of printing resolution was both studied qualitatively and quantitatively on flow visualization. The authors concluded that there is a direct effect of this parameter when performing the experimental studies and the best biomodel is the one with the smaller roughness, corresponding to a print resolution of 50 μm. Additionally, the effect of coronary stenosis on hemodynamic changes were numerically and experimentally studied and both results are in good agreement. It was observed a recirculation flow at the post stenotic section when the regular diameter reduces 60%. Moreover, the velocity profiles and wall shear stress were evaluated, indicating a significant increase of these parameters in the stenosis throat.

These results have the potential of providing new insights and additional information about the importance of printing parameters, namely the resolution on *in vitro* biomodels.

8.5. Acknowledgments

This work has been supported by FCT – Fundação para a Ciência e Tecnologia within the R&D Units Project Scope: UIDB/00319/2020, UIDB/04077/2020 and NORTE-01-0145-FEDER-030171, funded by COMPETE2020, NORTE 2020, PORTUGAL 2020 and FEDER. This project has received funding from the European Union's Horizon 2020 research and innovation programme under the Marie Sklodowska-Curie grant agreement No 798014. This project has received funding from the European Union's Horizon 2020 research and innovation programme under grant agreement No 828835. The authors would also like to express their gratitude to Dr. Paulo Sousa and Dr. Vânia Pinto, Minho University, for the assistance provided in measuring the roughness of the models.

Chapter 9

Numerical Simulation of Blood Pulsatile Flow in Stenotic Coronary Arteries: The Effect of Turbulence Modeling and non-Newtonian Assumptions[19]

Abstract

Atherosclerosis is a common cardiovascular disease characterized by the accumulation of plaques on the artery walls, resulting in the lumen stenosis. Over the past few decades, this pathological condition has been deeply studied and computational fluid dynamics has played an important role in investigating the blood flow behavior. Commonly, the blood flow is assumed to be laminar and a Newtonian fluid. However, under a stenotic condition, the blood behaves as a non-Newtonian fluid and the pulsatile blood flow through coronary arteries could result in a transition from laminar to turbulent flow condition. The aim of the present study is to analyze and compare numerically by means of CFD, the blood flow behavior, applying the k-ω SST model and a laminar assumption. The effects of Newtonian and non-Newtonian (Carreau) models were also studied.

According to the results, the turbulent model is shown to give a better overall representation of pulsatile flow in stenotic arteries. In addition, the effect of non-Newtonian modeling was found to be more significant in wall shear stress measurements than in velocity profiles.

Keywords: hemodynamics, CFD, atherosclerosis, turbulence, non-Newtonian, coronary arteries

9.1. Introduction

Cardiovascular diseases (CVDs) are the leading cause of death globally, being expected to cause over 22 million deaths per year in 2030. The main underlying pathological process of CVDs is atherosclerosis, an inflammatory disorder of the arterial wall, which narrows its lumen [3]. During early stages, there are no significant changes in the flow dynamics, nevertheless, as time progresses, these plaques play a critical

---

[19] Carvalho, V., Rodrigues, N., Lima, R., Teixeira, S., 2020. Numerical simulation of blood pulsatile flow in stenotic coronary arteries: The effect of turbulence modeling and non-Newtonian assumptions, International Conference on Applied Mathematics and Computer Science (ICAMCS), 2020, Athens, Greece.

role in altering the flow characteristics and transition to turbulence can occur, even at much lower Reynolds number [60,216]. To understand the flow field changes, several hemodynamic studies have been conducted. This can be achieved under *in vivo* conditions using different measurement techniques. However, it is difficult to measure with sufficient accuracy some hemodynamic parameters, e.g wall shear stress (WSS). For this reason, computational fluid dynamics (CFD) has been used as an effective alternative to investigate in detail several blood flow phenomena in blood vessels and an important component in the study of CVDs, allowing the calculation of various hemodynamic parameters with high precision [10,216,253].

One of the earliest detailed studies of the flow in stenosis was conducted by Young [243] considering the flow in a mildly constricted tube based on a simplified model. Over the years, research into hemodynamics has grown exponentially and researchers have taking different assumptions, because of the blood flow complexity. Some authors assumed the blood flow in coronary arteries to be laminar [35,50,55,212,213,218] and behave as Newtonian fluid [11,210,215,217,218], and others studied turbulence transition [60,216,225,226,254] and non-Newtonian effects [22,47,55,210,216]. In fact, in large vessels, blood can be considered as a homogeneous fluid with constant viscosity. However, in the presence of stenosis, it is observed that the viscosity decreases with increasing velocity and reduction of vessel diameter. Therefore, the non-Newtonian behavior should be considered [50]. Another important factor to the local hemodynamics is the shape of the stenosis. Some researchers apply idealized stenosis shapes [11,22,207], while others make use of artery stenotic models based on medical images [35,46,213]. For instance, Gaudio et al [50] compared Newtonian and non-Newtonian (Carreau-Yasuda model) blood behaviors in patient-specific stenotic coronary arteries at different degrees of stenosis. For that, the researchers investigated numerically the blood velocity and the distribution of the shear stress indices at different times of the cardiac cycle. Their results showed that the velocity for the Carreau-Yasuda model is slightly lower when compared to the Newtonian model, however, the non-Newtonian effects are most important in shear stress indices distributions. Kamangar and his team [46] investigated the effect of stenosis in left coronary arteries on the hemodynamics in suspected diseased patients, using non-Newtonian (Carreau model) and laminar assumptions. They observed a considerable pressure drop and an increase in the velocity and wall shear stress at the stenosis throat. In the post stenotic section, they observed the prevalence of a recirculation zone which can result in the growth or formation of a new stenosis.

To understand the turbulence transition effect on hemodynamic parameters, Mahalingam et al. [216] applied the SST k-ω model during pulsatile flow through coronary arteries for different degrees of stenosis. They demonstrated that the transition to turbulence starts occurring above 50% stenosis and becomes fully turbulent above and beyond 70% of stenosis.

According to the literature, the best suited turbulent model to simulate the blood flow in pulsatile conditions is the transitional k-ω model, also referred as SST k-ω. This has been investigated and validated by several authors [60,225,226,255] using as reference the experimental study of Ahmed and Giddens [256]. However, the comparison between laminar and turbulent modeling has not been greatly investigated.

In this regard, in the current study an analysis of the turbulence modeling effects on blood flow is performed, comparing the SST k-ω model to a laminar flow in an idealized coronary artery with 70% of stenosis. Additionally, the effect of shear-thinning blood behavior was also studied, by using the Carreau model.

9.2. Methodology

9.2.1. Geometry of the Stenotic Coronary Artery Model

To study the blood flow, it is necessary to obtain the three-dimensional geometry of the lumen of the coronary artery. This step was performed in the Design Modeler tool in ANSYS® workbench. The selected diameter was based on real data obtained in the literature [228], and according to some authors [216,230,231], the length of the stenosis is defined as twice the normal diameter. In addition, the entrance length was chosen so that the velocity profiles could be fully established proximal to the stenosis. The axisymmetric stenosis model developed, and its geometric parameters are represented in Figure 57.

9.2.2. Mesh Generation and Blood Flow Assumptions

The numerical meshing and simulations were performed in the computational fluid dynamics (CFD) package ANSYS Fluent (version R2). In Ansys Meshing, a hexahedral mesh was created with a bias factor to ensure the accuracy of computational calculations near the wall, and a more refined mesh in the stenotic section (Figure 57). To assure a mesh independent solution, grid tests were made by refining the mesh and rerunning the simulations until no significant differences were observed. The results were mesh independent after using a grid of 510,720 elements.

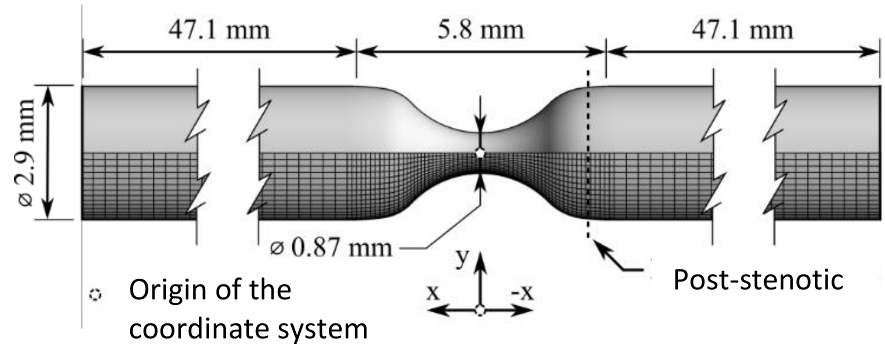

Figure 57. Geometry and dimensions of the 70% stenotic model with the generated mesh represented at the half bottom of the figure.

Blood flow is modeled using the Navier-Stokes equations and the continuity equations, which were solved by the semi-implicit method for pressure linked equations (SIMPLE) scheme; the artery walls were considered as rigid with a no-slip condition and a zero gauge pressure condition was applied at the outlet. To ensure that this analysis reflects the realistic simulation of *in vivo* conditions, a physiological inlet velocity profile adopted by Doutel et al. [35] was applied as seen in Figure 58 along the negative X-axis direction. This was written in C-language using the interface of User Defined Function (UDF) of Fluent and linked with the solver. For each transient simulation, four consecutive cardiac cycles were run and the results from the last cycle were analyzed.

When the blood is modeled as a Newtonian fluid, appropriate rheological parameters were applied with a density of 1072.033 $kg \cdot m^{-3}$ and a viscosity of 0.00315 $Pa \cdot s$, which are similar to those used in previous studies [35,103]. For the pulsatile non-Newtonian blood flow simulations, the selected viscosity model was the Carreau, since it is commonly used by several authors [35,54,55] to simulate the shear-thinning blood behavior and it is considered the most suitable to perform these simulations. In the Carreau model, the viscosity (μ) is given by Equation 17:

$$\mu = \mu_\infty + (\mu_0 - \mu_\infty)[1 + \lambda\dot{\gamma}^2]^{\frac{n-1}{2}} \qquad (17)$$

where, according to the previously cited authors, $\mu_\infty = 0.00345\, Pa \cdot s$ is the infinite shear viscosity, $\mu_0 = 0.0560\, Pa \cdot s$ is the blood viscosity at zero shear rate, $\dot{\gamma}$ is the instantaneous shear rate, $\lambda = 3.313\, s$ is the time constant and $n = 0.3568$ is the power-law index.

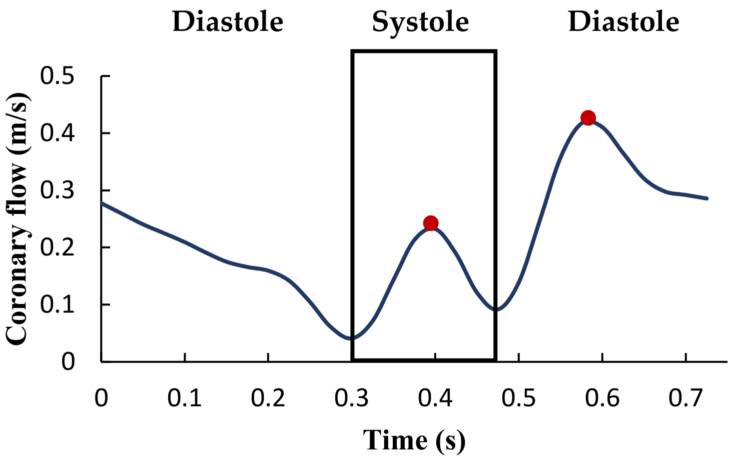

Figure 58. Velocity profile adopted in the simulation, representing a full cardiac cycle, according to Doutel et al. [35]. The red dots represent the peaks of the systolic and diastolic cycle, respectively.

9.2.3. Turbulence Modeling: Transitional k-ω Model

The transitional k-ω model is similar to the standard model, but with some modifications. The SST k-ω model has two other transport equations, one for the intermittency and one for the transition onset criteria. This is of interest in this study since the flow is not fully turbulent in the entire domain or throughout the entire cardiac cycle [60,226]. Moreover, this model is used to effectively combine the robust and accurate formulation of the k-ω model in the near-wall regions with the freestream independence of the k-ε model far from the wall [56,60,220].

9.3. Results and Discussion

9.3.1. Turbulent Models and Laminar Assumption

To assess the flow behavior through the simulated stenotic artery, a velocity profile of the fluid flow was plotted along the geometry center. The plotted data starts near the stenosis center, where X = 0 and follows the blood flow direction until X = -50 mm. Figure 59 I) and II) represent the velocity flow in the diastolic and systolic peak, respectively, with both assuming the blood as a Newtonian fluid, to compare the effect of the laminar and turbulent behavior according to the SST k-ω model.

Through observation of Figure 59, it is possible to observe that the velocity waveform near and at the stenosis throat (X = 0) the predicted values by both models in the different phases of the cardiac cycle are in excellent agreement. However, after the contraction, the differences are more notable.

In the diastolic peak (Figure 59 (I)), the SST k-ω and laminar model show a similar behavior along the geometry, with a gradual reduction in velocity after stenosis. These results are in good agreement with a study conducted by Straatman et al. [226], who also compared the SST k-ω model with experimental data obtained by Ahmed and Giddens [256]. Looking at Figure 59 (II), it can be also observed an identical behavior for both models, however, the transitional k-ω model presents an earlier drop in velocity, that marks the end of the recirculation zone. The laminar model predicts a slightly higher recirculation length.

In Straatman work [226], it was also showed that the transitional k-ω model over-predict a bit the length of the recirculation when compared to the experimental data. Taking this assumption, it can be concluded that the laminar model over-predicts considerably more the recirculation length, and, therefore is not the most adequate.

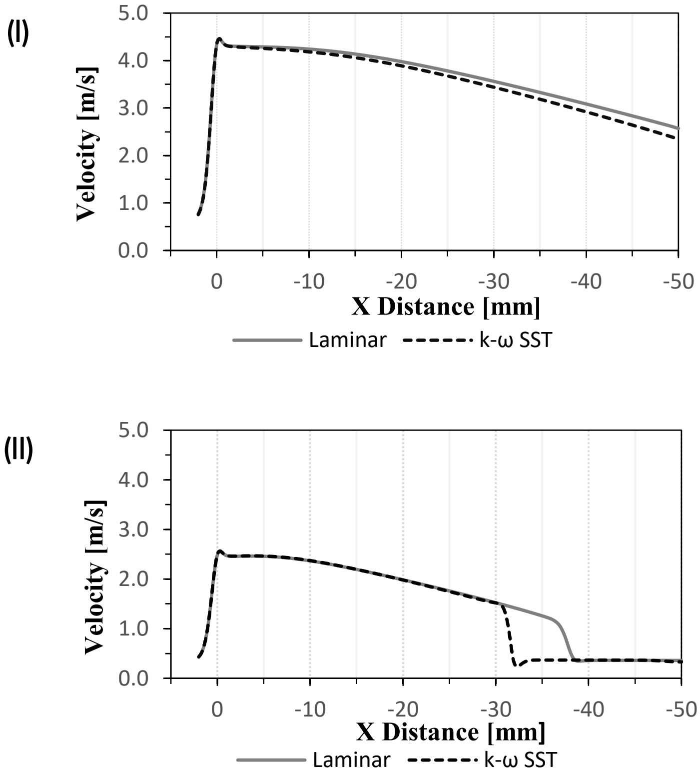

Figure 59. Simulated centerline velocity at the time of the: (I) diastolic peak; (II) systolic peak of the input velocity profile.

Despite the few differences between the two models, it was showed that the model selection influences the results and the most adequate model seems to be the transitional k-ω. For this reason, the remaining simulations were performed with that model.

9.3.2. Newtonian and Non-Newtonian Behavior

To compare the non-Newtonian effects in flow behavior, the velocity profiles in the stenotic and post stenotic section (X = -2.5 mm), only at the diastolic peak were evaluated. As can be observed in Figure 60 (a) and (b), the two models present the same behavior and there is only a small variation in the maximum velocity. It can be seen a lower maximum value in the curve of the Newtonian model compared to the Carreau model.

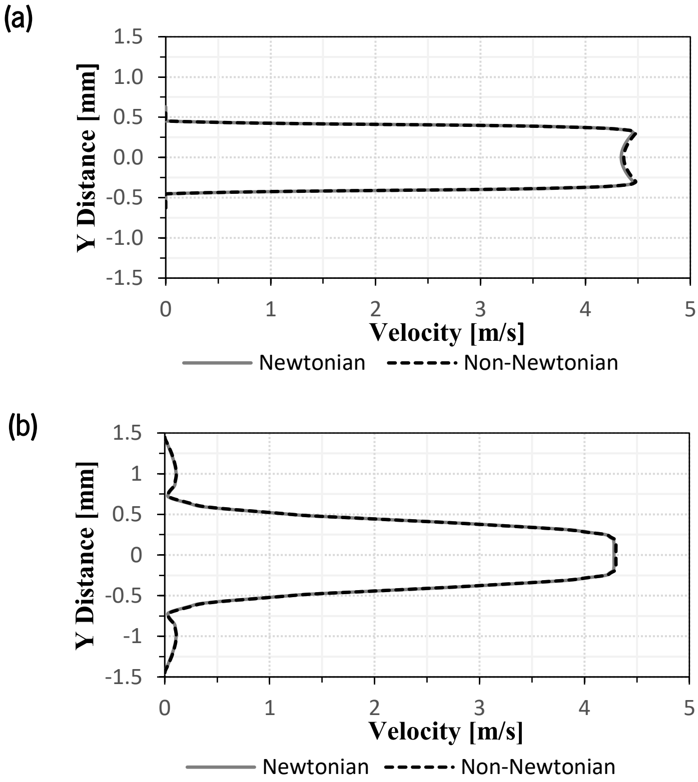

Figure 60. Comparison between the velocity profiles at (a) stenotic section; (b) the post-stenotic section.

Figure 61 shows the wall shear stress (WSS) along the coronary artery, in particular in the region of the stenosis at the diastolic peak. For incompressible fluids and non-slip conditions applied to the arterial wall, the spatial WSS, τ_w, is calculated through Equation 18:

$$\tau_w = \mu \frac{\partial u}{\partial y} = \mu \, \dot{\gamma} \tag{18}$$

where $\dot{\gamma}$ the deformation rate.

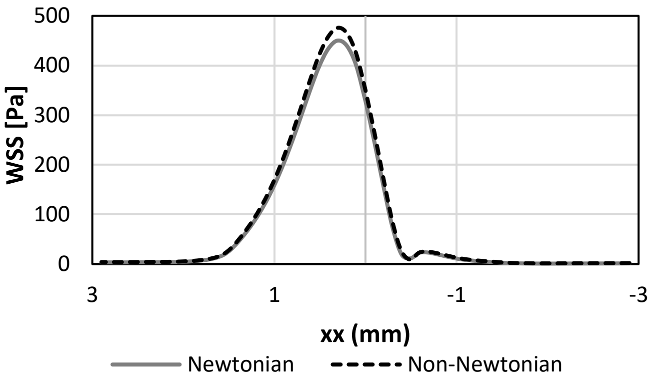

Figure 61. Comparison between the WSS using the Newtonian and Carreau model.

The maximum value of WSS is located in the maximum narrowing area and the differences between the two models are more perceptible than in velocity. Comparing the Newtonian model to the Carreau model, the first one predicts a lower value of WSS, visible in the peak where there is the presence of the stenosis. These results are in agreement with a previous study conducted by Gaudio et al. [50].

9.4. Conclusions

The present study provides new insights on the use of the transitional variant of the k-ω model for predicting pulsatile flow through stenotic coronary arteries, instead of the laminar model, which is used commonly by several researchers. Note that, the differences between the two models are verified only in the post stenotic area, where recirculation occurs.

The authors also concluded that the non-Newtonian effects are more significant in the wall shear stress measurements, and the Newtonian model predicts lower values. The same tendency was observed in the velocity profiles, however, it is almost imperceptible.

Despite the results agreed with previous studies, further investigations are necessary, since the physiological flows are complex.

9.5. Acknowledgments

This work has been supported by FCT – Fundação para a Ciência e Tecnologia within the R&D Units Project Scope: UIDB/00319/2020, UIDB/04077/2020, and NORTE-01-0145-FEDER-030171, funded by COMPETE2020, NORTE 2020, PORTUGAL 2020 and FEDER.

Chapter 10

Numerical Validation and Transient Simulations

This chapter presents further validation of the numerical model and also, the effect of the stenosis degree in the transient simulations.

10.1. Numerical Validation

After presenting detailed numerical and experimental results of the blood flow behavior, in the presence of stenotic coronary arteries, it is important to validate the numerical model. Quantitative results, already visualized in Chapter 8 (Figure 56), are now presented in Figure 62. To this end, the experimental results were obtained by tracking particles in the stenotic section, while the numerical data were obtained by drawing a line transversely to the channel in the stenotic section.

Looking at the results, it can be observed that the velocity progressively increases with the stenosis severity, and this tendency is well shown by both experimental measurements and numerical results.

In general, the experimental results are in very good agreement with the numerical simulation. However, closer to the walls the measurements are more accurate. This can be explained by the lower velocities in that region. At these locations, the particles preserved its rounded shape, and has facilitated the localization of the particles' centroid, and consequently the tracking process. In turn, in the central region of the channels, the particles have higher velocities, which resulted in an elliptical shape, making measurements less accurate. This, combined with irregular illumination and low resolution, are the main causes for higher uncertainties and discrepancies between the numerical and experimental measurements in the central region, which is more noticeable in Figure 62 (d). Figure 62 (a) represents the healthy model and the results are similar, with only two experimental points slightly away from the velocity profile. For the stenotic cases with 50, 60 and 80% (Figure 62 (b), (c) and (e), respectively) the results are also in good agreement.

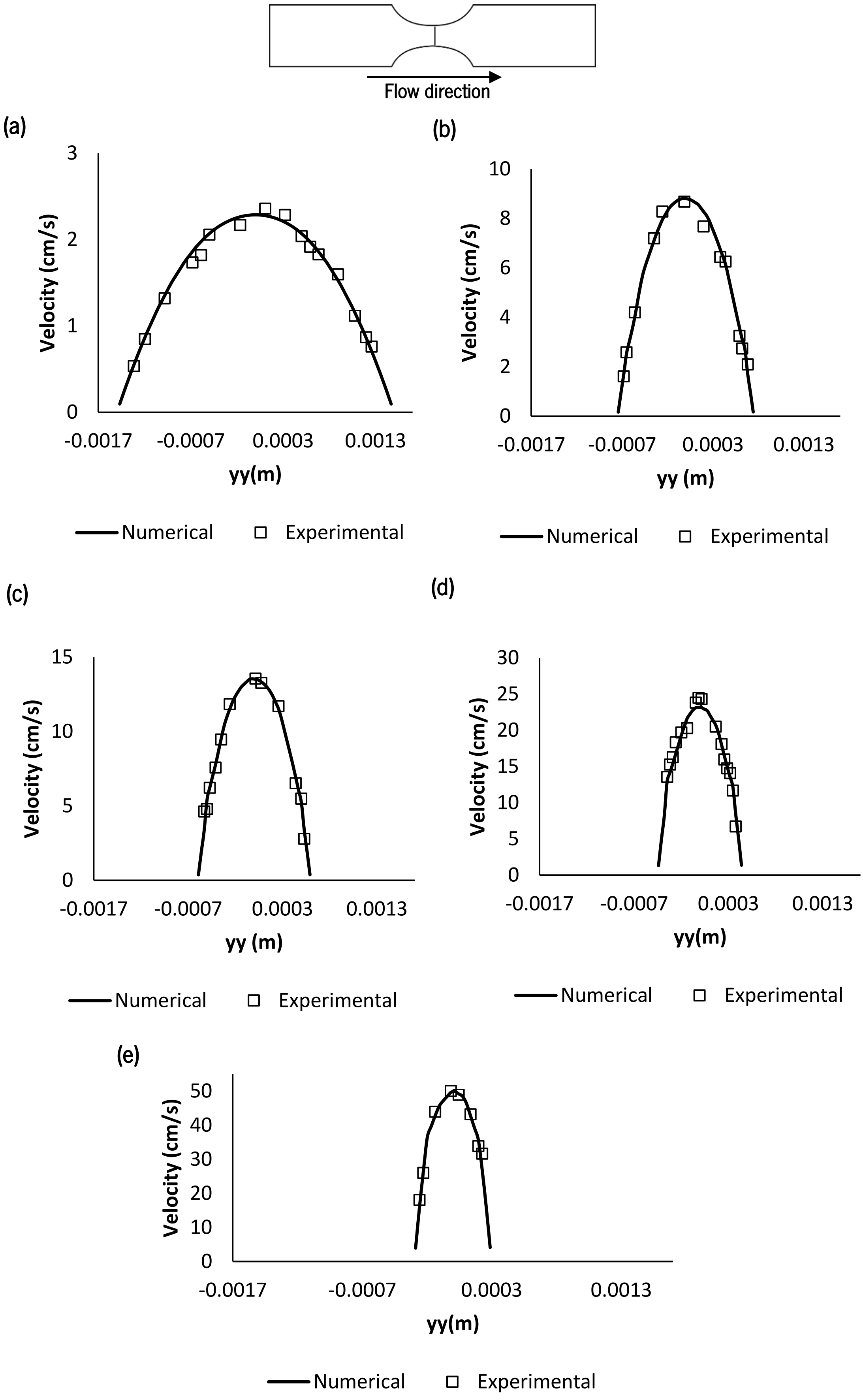

Figure 62.Comparison between numerical and experimental results for each degree of stenosis (a) healthy model (0%); (b) 50%; (c) 60%; (d) 70% and (e) 80%.

10.2. Geometry Effect on Blood Flow

Aiming to understand the effect of different geometries on hemodynamics, normalized vectors for 50 and 70% stenosis were investigated for Model 1 and Model 2, applying the same stationary inlet velocity used to perform the experimental studies (Figure 63).

In terms of velocity magnitude, the results in the stenotic region (maximum value) are practically the same in all cases. This was expected since the diameter reduction is equal. Nevertheless, in the post stenotic region, some differences can be observed. In Model 2 with 50% of stenosis (Figure 63 (a), right) some vectors are in the opposite direction of the flow, while in Model 1 (Figure 63(a), left), all vectors follow the flow direction. This proves that the pointed areas in the Biofabics geometry create instability.

In Figure 63 (b), a well-defined recirculation zone is predicted by both models, however, a longer one can be observed in Model 1 (Figure 63 (b), left). In Model 2, there is a recirculation zone shorter and near the pointed area (Figure 63 (b), right).

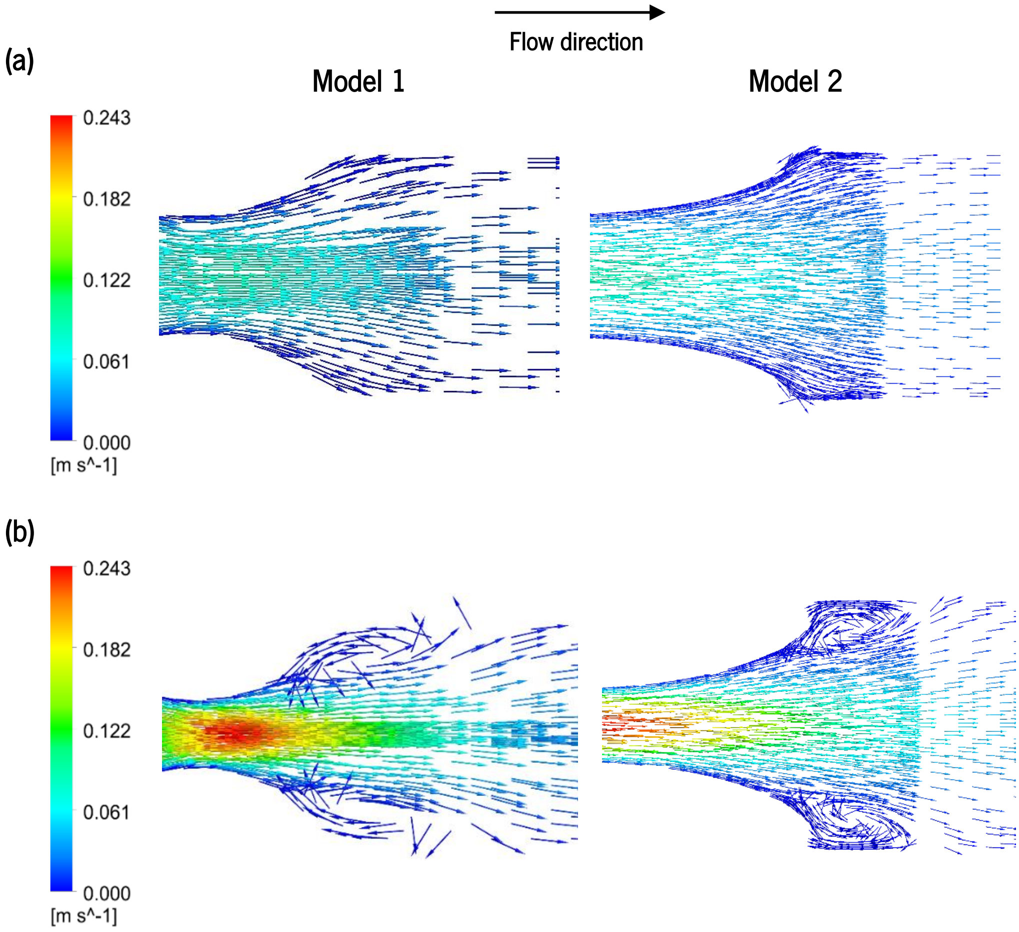

Figure 63.Velocity vectors (a) 50%; (b) 70%. **Left:** Model 1; **Right:** Model 2.

Through the analysis of these results, it can be concluded that effectively the geometry influences the hemodynamic behavior within the arteries. Note that, here very low velocities were studied, so using higher velocities the differences can be more significant.

Moreover, it should be highlighted that the Model 1 (left) is closer to reality since the accumulation of fatty deposits occurs irregularly and does not form sharp areas.

10.3. Pulsatile Nature of Blood Flow

10.3.1. Simulation Stability in Transient Calculations

Based on the study carried out by Doutel et al. [35], an inlet velocity was used in the transient calculations of the present study (Chapter 6). Some of the results presented in Chapter 9, were taken after four consecutive cycles, assuming that the flow has reached a stationary state ([35]). To verify if the present study results follow this trend, the maximum velocities reached in each cycle for the systole and diastole points are represented in Figure 64.

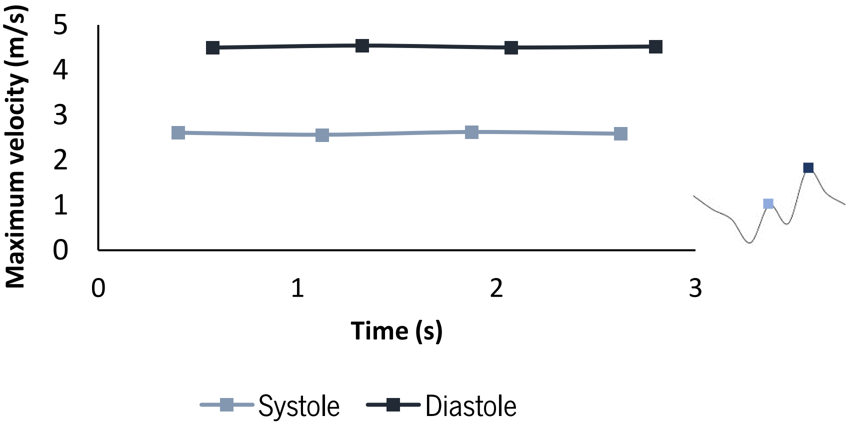

Figure 64. Stability of simulation through the four consecutive cardiac cycles run.

Looking at the results, it is possible to verify that there was stability along the four consecutive transient calculations and only small variations in maximum velocities are visible. This is verified in both phases of the cardiac cycle. Therefore, the assumption of the stability after 4 cycles has been proved, and even along with the different cycles, the maximum velocity seems the same.

10.3.2. Effect of Stenosis Degree in Centerline Velocity and WSS

To evaluate the flow behavior through the stenotic artery in the presence of different degrees of stenosis (0, 50 and 70%), the centerline velocity was plotted, only in Model 1. The plotted data starts near the stenosis center, where x = 0 and follows the blood flow direction until x = - 0.05 m. The results obtained are depicted in Figure 65 (a) and (b), corresponding respectively, to the systolic and diastolic phases of the cardiac cycle.

In both phases of the cardiac cycle, the stenotic models attain their maximum velocity in the center of the geometry (x=0m), and as expected, the healthy model maintains its velocity along axis (approximately 0.3 m/s during systole and 0.6 m/s during diastole). Moreover, both stenotic models present a similar behavior until the stenosis throat. Nevertheless, the differences after the contraction are quite significant.

During systole (Figure 65 (a)), it can be observed that for both models there is a continuous drop in the centerline velocity after stenosis, until afterward occurs a more noticeable drop in velocity, which is more accented in the 70% stenosis case. This marks the end of the recirculation zone predicted by both models. However, the 70% stenotic model presents higher velocities and a recirculation zone longer than the 50% model, due to the greater diameter reduction seen in this model.

Similarly to the systolic phase, during diastole (Figure 65 (b)), the 50% stenotic model shows a recirculation length significatively lower, marked by an earlier and smoother drop in velocity. In turn, the 70% stenotic model presents a gradual reduction in velocity until the end of the artery. This is due to the recirculation zone length, which is higher than the channel length. Regarding this result, a remark must be made. Through the analysis of velocity vectors results, the existence of vectors in the opposite direction to the flow was verified since the end of the artery. To confirm that this was a valid result, a new test was performed using the same geometry with a longer length and, indeed, the end of recirculation was observed. This proves that in the presence of this pathology, changes in blood flow can be huge, especially during diastole, where the highest velocities are reached.

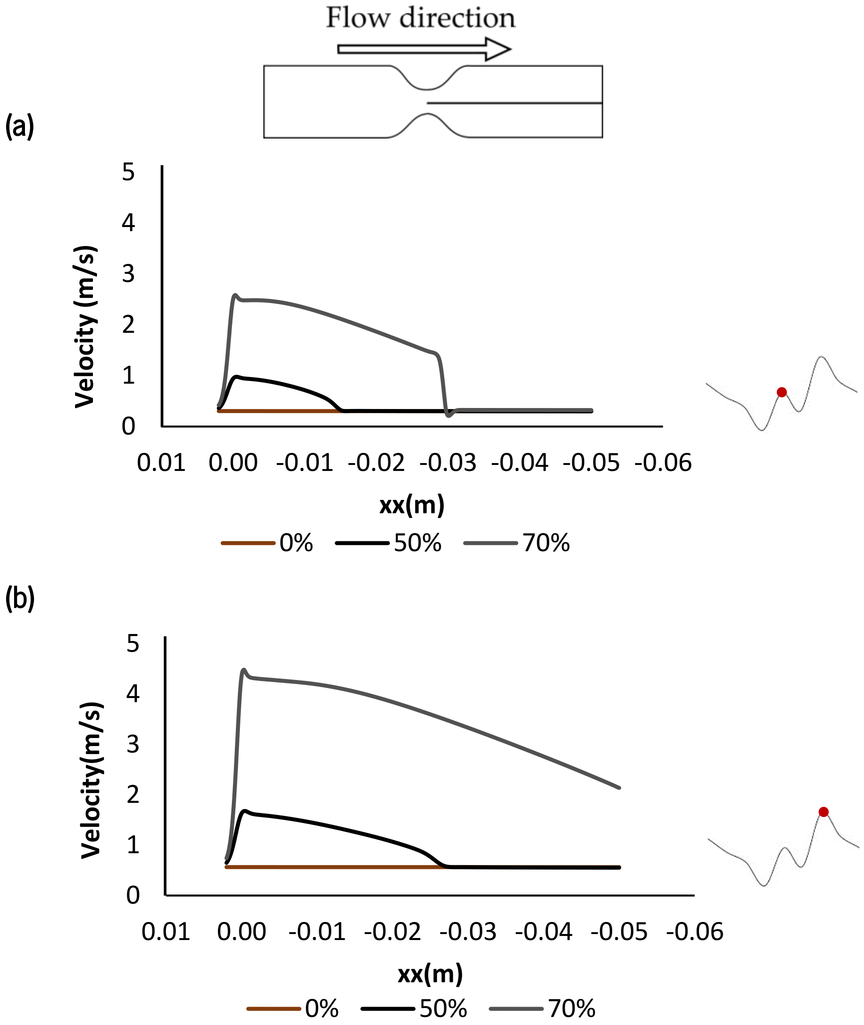

Figure 65.Centerline velocity at the time of the: (a) systolic peak; (b) diastolic peak of the input velocity profile.

Additionally, as WSS is an important factor in the development of atherosclerosis, its evolution along the stenotic artery was also studied in the two main phases of the cardiac cycle, systole and diastole (Figure 66 (a) and (b), respectively).

Regarding the WSS results during systole (Figure 66 (a)), for x≈ -0.03m can be observed a small peak in the grey plot (70%), which represents the end of the recirculation zone for this model and thus, after that, the WSS values decrease and maintain a constant value until the end. Although this behavior is not perceptible for the 50% case, a smoother variation in WSS happens, without any marked peak. This is due to the smoother reduction in velocity (Figure 65 (a)) verified in this model when compared to the 70% case.

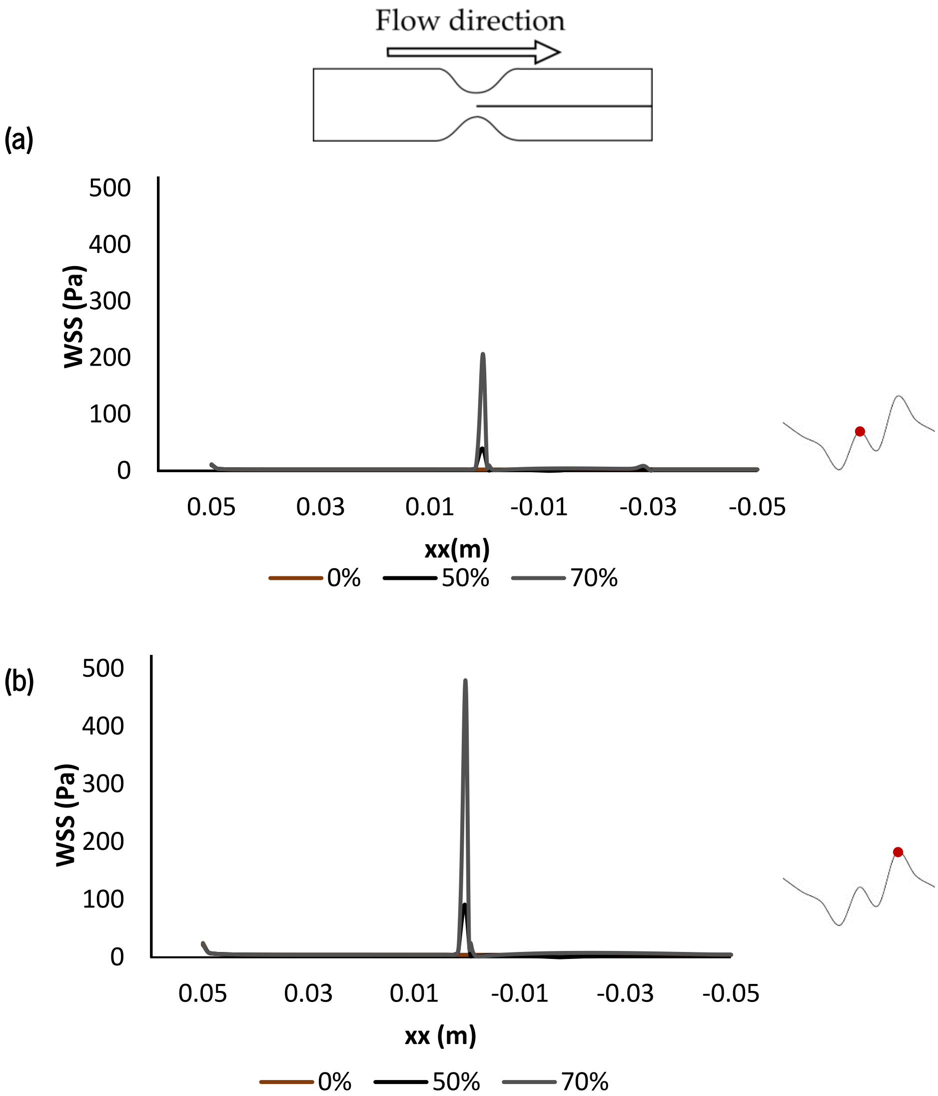

Figure 66. Comparison between the WSS obtained for each degree of stenosis during (a) systole and (b) diastole.

Moreover, the maximum WSS is observed at the stenosis throat and its value increases with the degree of stenosis. For 70% and 50% of stenosis, 207 Pa and 39.6 Pa of WSS are observed, respectively.

During diastole (Figure 66 (b)), there is no peak in the grey plot in the post stenotic section. This is explained by the continuity of the recirculation in the 70% case, as clarified previously. For the 50% model, the behavior is very similar to that obtained during diastole, only presenting lower WSS values. Regarding the healthy model, this presents a constant value of WSS in each phase (approximately 2.3 Pa during systole and 4.3 Pa during diastole) and shows that in a healthy situation the WSS should be much lower than the ones verified, showing the impact of the degree of stenosis on some hemodynamic parameters.

During diastole, the maximum WSS is also observed at the throat stenosis, however, the values are much higher than during systole. For 70% and 50% of stenosis, 480 Pa and 91.3 Pa of WSS are observed respectively.

The results obtained are in agreement with other studies, for instance, Mulani et al. [22] had similar conclusions when comparing a healthy model to stenotic models with a geometry quite similar to those presented in this study. In addition, through the analysis of these results, it can be concluded that effectively the transient condition is extremely important to understand what happens *in vivo* and comparing both phases of the cardiac cycle, significant differences were observed.

Chapter 11

Conclusions and Future Directions

This chapter summarizes the main conclusions of this dissertation and suggests directions for further research.

11.1. Conclusions

In this dissertation, a numerical and experimental study was performed to understand the influence of coronary stenosis severity on hemodynamics. For this purpose, numerical simulations using CFD and experimental flow analysis using a high-speed video microscopy system were carried out.

Initially, simplified numerical simulations were performed applying a stationary and laminar flow, assuming the blood as a Newtonian fluid. These first considerations were validated with the experimental measurements and the results presented are in good agreement. In a posterior phase, the pulsatile nature of blood flow and the effect of turbulence modeling were studied. After data analysis and comparison with the literature, it was concluded that the SST k-ω model is the most adequate model to mimic the realistic blood flow, and thus, it was applied in the remaining simulations. Aside the pulsatile and turbulence conditions, the Carreau non-Newtonian model was implemented to verify its influence on hemodynamic properties, which proved to be of little significance. However, since blood is a non-Newtonian fluid, the subsequent simulations were performed using the SST k- ω and Carreau model. From overall results, it was observed that as the stenosis severity increases, the velocities and WSS increase and a recirculation zone is observed in the post stenotic section when the diameter reduction is greater than 60%.

Regarding the experimental studies, these were performed in parallel to the numerical simulations. Firstly, the printing resolution effect was studied qualitatively through observation in the microscope. Secondly, to support the qualitative results, the roughness associated with each printing resolution was measured. In the end, it was proved that the printing resolution influences the flow visualizations, being directly related to an increase in roughness. Thereby, the Biofabics models proved to be a good alternative to perform accurately *in vitro* studies.

In conclusion, the main objectives proposed at the beginning of this dissertation were fulfilled, in which numerical and experimental models capable of simulating blood flow at stenotic coronary arteries have been developed. Additionally, with more research being conducted on coronary geometry models, it is expected that research findings will improve the understanding of the biomechanical pathophysiology of CAD and its complications, and therefore, the development of new treatments.

11.2. Future Directions

The starting point for future research will lie in performing the experimental studies on the models printed by stereolithography and compare the results obtained with the ones presented in this study.

As an extension of the developed work would be interesting, firstly, to use realistic models based on patient-specific data and verify its impact on hemodynamic results. Secondly, the complexity of the simulation's models should be improved. For instance, considering the effect of elastic walls on hemodynamics and simulate the effect of erythrocytes. The use of a multiphase model would be essential to better understand the interaction between the plasma and the particles.

In addition, despite the CFD work used in this study assumes both Newtonian and non-Newtonian blood flow behavior using stationary and pulsatile conditions, for the *in vitro* study only Newtonian and steady-state blood flow was considered. For this reason, it would be important to experimentally consider the non-Newtonian blood behavior using an adequate blood analogue combined with unsteady flow conditions to mimic the cardiac cycle.

Moreover, image analysis plays a significant role in these studies. Although the methodology used allowed the validation of the numerical data with satisfactory results, improvements on the quality and resolution of the images are needed. Hence, it is extremely important to obtain more reliable and accurate results. Therefore, the use of a more advanced high-speed camera to perform the blood flow measurements would be crucial to obtain better flow visualizations.

Finally, to obtain more accurate roughness results, it would be important to use an optical profilometer. This enables a precise and non-contact surface measurement and characterization, allowing the assessment of the roughness values of the *in vitro* models.

References

[1] World Health Organization (WHO), Cardiovasc. Dis. Fact Sheet No. 317. (2017).

[2] Y. Sun, X. Guan, Autophagy: A new target for the treatment of atherosclerosis, Front. Lab. Med. 2 (2018) 68–71. https://doi.org/10.1016/j.flm.2018.07.002.

[3] A. Haverich, E.C. Boyle, Atherosclerosis Pathogenesis and Microvascular Dysfunction, First, Springer, 2019. https://doi.org/https://doi.org/10.1007/978-3-030-20245-3.

[4] K. Rogers, The cardiovascular System, First, Britannica Educational Publishing, 2011.

[5] E. Fatahian, N. Kordani, H. Fatahian, The application of computational fluid dynamics (CFD) method and several rheological models of blood flow: A review, Gazi Univ. J. Sci. 31 (2018) 1213–1227.

[6] S.G. Yazdi, P.H. Geoghegan, P.D. Docherty, M. Jermy, A. Khanafer, A Review of Arterial Phantom Fabrication Methods for Flow Measurement Using PIV Techniques, Ann. Biomed. Eng. 46 (2018) 1697–1721. https://doi.org/10.1007/s10439-018-2085-8.

[7] L. Sun, Zhongua; Xu, Computational fluid dynamics in coronary artery disease, Comput. Med. Imaging Graph. (2014) 651–663. https://doi.org/10.1016/j.compmedimag.2013.11.002.

[8] S.N. Doost, D. Ghista, B. Su, L. Zhong, Y.S. Morsi, Heart blood flow simulation: A perspective review, Biomed. Eng. Online. 15 (2016) 95025. https://doi.org/10.1186/s12938-016-0224-8.

[9] K. Tu, Jiyuan; Inthavong, Kiao; Wong, Computational Hemodynamics- Theory, Modelling and Applications, Springer, 2015.

[10] S.C.P. Cheung, K.K.L. Wong, G.H. Yeoh, W. Yang, J. Tu, R. Beare, T. Phan, Experimental and numerical study on the hemodynamics of stenosed carotid bifurcation, Australas. Phys. Eng. Sci. Med. 33 (2010) 319–328. https://doi.org/10.1007/s13246-010-0050-4.

[11] E. Doutel, J. Carneiro, J.B.L.M. Campos, J.M. Miranda, Artificial stenoses for computational hemodynamics, Appl. Math. Model. 59 (2018) 427–440. https://doi.org/10.1016/j.apm.2018.01.029.

[12] E.N. Marieb, S.M. Keller, Essentials of Human Anatomy& Physiloogy, Twelfth, Pearson, 2017.

[13] C. VanPutte, J. Regan, A. Russo, B. Manager, A. Reed, Seeley's Essentials of Anatomy & physiology, Ninth, McGraw-Hill Education, 2016.

[14] A. Formaggia, Luca; Quarteroni;Alfio;Veneziani, Cardiovascular Mathematics- Modeling and simulation of the circulatory system, First, Springer, 2009. https://doi.org/10.1017/CBO9781107415324.004.

[15] A.A. Goodman, Understanding the Human Body : An Introduction to Anatomy and Physiology, First, The Great Courses, United States of America, 2004.

[16] W. Susan, P.D.. D.A, M.. Denton A.Cooley, The Human Body How it Works: The Circulatory System, First, Chelsea House Pub, New York, 2009.

[17] R.E. Klabunde, Cardiovascular phisiology concepts, second, 2019. https://doi.org/10.1017/CBO9781107415324.004.

[18] E.F.G. Griggs, Robert; Wing, Cecil essentials of medicine, Ninth, Elsevier, 2016.

[19] A.S. Gupta, A. Marsh, Cardiology and the Cardiovascular System, First, CRC Press, 2015.

[20] T. Chaichana, Z. Sun, J. Jewkes, Computation of hemodynamics in the left coronary artery with variable angulations, J. Biomech. 44 (2011) 1869–1878. https://doi.org/10.1016/j.jbiomech.2011.04.033.

[21] M. Ahmadi, R. Ansari, Computational simulation of an artery narrowed by plaque using 3D FSI method: Influence of the plaque angle, non-Newtonian properties of the blood flow and the hyperelastic artery models, Biomed. Phys. Eng. Express. 5 (2019) 45037. https://doi.org/10.1088/2057-1976/ab323f.

[22] S.S. Mulani, P.I. Jagad, Analysis of the Effects of Plaque Deposits on the Blood Flow through Human Artery, Int. Eng. Res. J. 41 (2015) 2319–3182. http://www.irdindia.in/journal_ijtarme/pdf/vol4_iss1/12.pdf.

[23] R. Lima, Microfluidic Devices Based on Biomechanics, in: Integr. Nano-Biomechanics, Elsevier, 2018: pp. 217–263. https://doi.org/10.1016/b978-0-323-38944-0.00007-3.

[24] G.J. Tortora, B. Derrickson, Principles of Anatomy & Physiology, Fifteenth, Wiley, 2017.

[25] F. Yilmaz, M.Y. Gundogdu, A critical review on blood flow in large arteries; relevance to blood rheology, viscosity models, and physiologic conditions, Korea Aust. Rheol. J. 20 (2008) 197–211.

[26] D.A. Rubenstein, W. Yin, M. Frame, Biofluid Mechanics, Second, Elsevier, 2015.

[27] S. Boujena, N. El Khatib, O. Kafi, Generalized Navier–Stokes equations with non-standard conditions for blood flow in atherosclerotic artery, Appl. Anal. 95 (2016) 1645–1670. https://doi.org/10.1080/00036811.2015.1068297.

[28] P.C. Sousa, F.T. Pinho, M.S.N. Oliveira, M.A. Alves, Extensional flow of blood analog solutions in microfluidic devices, Biomicrofluidics. 5 (2011). https://doi.org/10.1063/1.3567888.

[29] F. Abdolmaleki, S.M. Gheibi Hayat, V. Bianconi, T.P. Johnston, A. Sahebkar, Atherosclerosis and immunity: A perspective, Trends Cardiovasc. Med. 29 (2019) 363–371. https://doi.org/10.1016/j.tcm.2018.09.017.

[30] H. Thomas, J. Diamond, A. Vieco, S. Chaudhuri, E. Shinnar, S. Cromer, P. Perel, G.A. Mensah, J. Narula, C.O. Johnson, G.A. Roth, A.E. Moran, Global Atlas of Cardiovascular Disease Prevention and Control, World Health Organization, 2011. https://doi.org/10.1016/j.gheart.2018.09.511.

[31] S. Beier, J. Ormiston, M. Webster, J. Cater, S. Norris, Vascular Hemodynamics with Computational Modeling and, in: Comput. Vis. Intravasc. Imaging Comput. Stenting, First, Elsevier, 2017: pp. 227–251. https://doi.org/10.1016/B978-0-12-811018-8.00009-6.

[32] A.B. Rabbani, P.M. Grossman, Chronic Coronary Artery Disease, Tenth, Elsevier, 2018. https://doi.org/10.1002/9781118484784.ch9.

[33] P.K. Shah, Inflammation, infection and atherosclerosis, Trends Cardiovasc. Med. 29 (2019) 468–472. https://doi.org/10.1016/j.tcm.2019.01.004.

[34] J.Y. Moon, D.C. Suh, Y.S. Lee, Y.W. Kim, J.S. Lee, Considerations of Blood Properties , Outlet Boundary Conditions and Energy Loss Approaches in Computational Fluid Dynamics Modeling, 9 (2014) 1–8.

[35] E. Doutel, N. Viriato, J. Carneiro, J.B.L.M. Campos, J.M. Miranda, Geometrical effects in the hemodynamics of stenotic and non-stenotic left coronary arteries—numerical and in vitro approaches, Int. j. Numer. Method. Biomed. Eng. 35 (2019) 1–18. https://doi.org/10.1002/cnm.3207.

[36] K.P. Papadopoulos, M. Gavaises, I. Pantos, D.G. Katritsis, N. Mitroglou, A. Euroclinic, Derivation of flow related risk indices for stenosed left anterior descending coronary arteries with the use of computer simulations, Med. Eng. Phys. 38 (2016) 929–939. https://doi.org/10.1016/j.medengphy.2016.05.016.

[37] J. Bronzino, The Biomedical Engineering Handbook- Medical Devices and Systems, Third, 2006. https://doi.org/10.1201/b12938.

[38] D. L.Bhatt, Cardiovascular Intervention: A Companion to Braunwald's Heart Disease, First, Elsevier, 2016.

[39] L. Waite, J. Fine, Applied Biofluid Mechanics, First, McGraw-Hill Companies, 2007.

[40] A.M. Malek, S.L. Alper, Hemodynamic Shear Stress and Its Role in Atherosclerosis, Am. Med. Assoc. 282 (1999) 2035–2042.

[41] F. Gijsen, Y. Katagiri, Expert recommendations on the assessment of wall shear stress in human coronary arteries: Existing methodologies, technical considerations, and clinical applications, Eur. Heart J. 40 (2019) 3421–3433. https://doi.org/10.1093/eurheartj/ehz551.

[42] J. Dong, Development of a Haemodynamic Model for Improving Clinical Treatment of Vascular Disease, PhD thesis, RMIT University, 2015.

[43] D. Ku, Blood flow in arteries, Annu. Rev. Fluid Mech. (1997) 399–434. https://doi.org/10.1146/annurev.fluid.29.1.399.

[44] C.G. Caro, J.M. Fitz-Gerald, R.C. Schroter, Atheroma and arterial wall shear. Observation, correlation and proposal of a shear dependent mass transfer mechanism for atherogenesis., Proc. R. Soc. London. Ser. B. Biol. Sci. 177 (1971) 109–159. https://doi.org/10.1098/rspb.1971.0019.

[45] A.J. Apostolidis, A.N. Beris, P.S. Dhurjati, Introducing CFD through a cardiovascular application in a fluid mechanics course, Chem. Eng. Educ. 48 (2014) 175–184.

[46] S. Kamangar, N.J. Salman Ahmed, I.A. Badruddin, N. Al-Rawahi, A. Husain, K. Govindaraju, T.M. Yunus Khan, Effect of stenosis on hemodynamics in left coronary artery based on patient-specific CT scan, Biomed. Mater. Eng. 30 (2019) 463–473. https://doi.org/10.3233/BME-191067.

[47] T. Chaichana, Z. Sun, J. Jewkes, Computational Fluid Dynamics Analysis of the Effect of Plaques in the Left Coronary Artery, Comput. Math. Methods Med. 2012 (2012) 504367. https://doi.org/10.1155/2012/504367.

[48] F.M. White, Fluid Mechanics, 8th ed., 2016.

[49] B. Koeppen, Bruce; Stanton, Berne & Levy Physiology, Seventh, Elsevier, 2018.

[50] L.T. Gaudio, M. V. Caruso, S. De Rosa, C. Indolfi, G. Fragomeni, Different Blood Flow Models in Coronary Artery Diseases: Effects on hemodynamic parameters, Proc. Annu. Int. Conf. IEEE Eng. Med. Biol. Soc. EMBS. 2018-July (2018) 3185–3188. https://doi.org/10.1109/EMBC.2018.8512917.

[51] R. Fahraeus, T. Lindqvist, The viscosity of blood in narrow capillary tubes, Am. J. Physiol. (1931) 562–568.

[52] N. Sher, S. Nadeem, Carreau fluid model for blood flow through a tapered artery with a stenosis, Ain Shams Eng. J. 5 (2014) 1307–1316. https://doi.org/10.1016/j.asej.2014.05.010.

[53] A. Razavi, E. Shirani, M.R. Sadeghi, Numerical simulation of blood pulsatile flow in a stenosed carotid artery using different rheological models, J. Biomech. 44 (2011) 2021–2030. https://doi.org/10.1016/j.jbiomech.2011.04.023.

[54] M.A. Kabir, M.F. Alam, M.A. Uddin, A numerical study on the effects of reynolds number on blood flow with spiral velocity through regular arterial stenosis, Chiang Mai J. Sci. 45 (2018) 2515–2527.

[55] B. Liu, J. Zheng, R. Bach, D. Tang, Influence of model boundary conditions on blood flow patterns in a patient specific stenotic right coronary artery, Biomed. Eng. Online. 14 (2015) S6. https://doi.org/10.1186/1475-925X-14-S1-S6.

[56] Ansys Inc, ANSYS Fluent User ' s Guide, (2013).

[57] A. Ostadfar, Biofluid Mechanics: Principles and Applications, First, Elsevier, 2016. https://doi.org/10.1016/C2014-0-01583-3.

[58] T. Wang, Pathogenesis of atherosclerosis, Diagnostic Histopathol. 23 (2017) 473–478. https://doi.org/10.1016/j.mpdhp.2017.11.009.

[59] P. Libby, J.E. Buring, L. Badimon, G.K. Hansson, J. Deanfield, M.S. Bittencourt, L. Tokgözoğlu, E.F. Lewis, Atherosclerosis, Nat. Rev. Dis. Prim. 5 (2019) 1–18. https://doi.org/10.1038/s41572-019-0106-z.

[60] C. Moreno, K. Bhaganagar, Modeling of stenotic coronary artery and implications of plaque morphology on blood flow, Model. Simul. Eng. 2013 (2013) 14. https://doi.org/10.1155/2013/390213.

[61] W. Choi, J.H. Park, H. Byeon, S.J. Lee, Flow characteristics around a deformable stenosis under pulsatile flow condition, Phys. Fluids. 30 (2018) 1070–6631. https://doi.org/10.1063/1.5009063.

[62] R.K. Banerjee, K.D. Ashtekar, T.A. Helmy, M.A. Effat, L.H. Back, S.F. Khoury, Hemodynamic diagnostics of epicardial coronary stenoses: In-vitro experimental and computational study, Biomed. Eng. Online. 7 (2008). https://doi.org/10.1186/1475-925X-7-24.

[63] J. Bale-Glickman, K. Selby, D. Saloner, Ö. Savaş, Experimental flow studies in exact-replica phantoms of atherosclerotic carotid bifurcations under steady input conditions, J. Biomech. Eng. 125 (2003) 38–48. https://doi.org/10.1115/1.1537734.

[64] A. Karimi, M. Navidbakhsh, A. Shojaei, K. Hassani, S. Faghihi, Study of plaque vulnerability in coronary artery using Mooney-Rivlin model: A combination of finite element and experimental method, Biomed. Eng. Appl. Basis Commun. 26 (2014) 1–7. https://doi.org/10.4015/S1016237214500136.

[65] A. Karimi, R. Razaghi, Interaction of the blood components and plaque in a stenotic coronary artery, Artery Res. 24 (2018) 47–61. https://doi.org/10.1016/j.artres.2018.11.002.

[66] N. DePaola, M.A. Gimbrone, P.F. Davies, C.F. Dewey, Vascular endothelium responds to fluid

shear stress gradients, Arterioscler. Thromb. 12 (1992) 1254–1257. https://doi.org/10.1161/01.atv.12.11.1254.

[67] A. V. Dokunin, A modification of the method of differential manometry for registration of the volume velocity of the blood flow, Bull. Exp. Biol. Med. 46 (1958) 1414–1417. https://doi.org/10.1007/BF00845194.

[68] K. Stepniak, A. Ursani, N. Paul, H. Naguib, Development of a phantom network for optimization of coronary artery disease imaging using computed tomography, Biomed. Phys. Eng. Express. 5 (2019) 45019. https://doi.org/10.1088/2057-1976/ab2696.

[69] P.J. Brands, A.P.G. Hoeks, L. Hofstra, R.S. Reneman, A noninvasive method to estimate wall shear rate using ultrasound, Ultrasound Med. Biol. 21 (1995) 171–185. https://doi.org/10.1016/S0301-5629(94)00111-1.

[70] B. Dunmire, K.W. Beach, K.H. Labs, M. Plett, D.E. Strandness, Cross-beam vector Doppler ultrasound for angle-independent velocity measurements, Ultrasound Med. Biol. 26 (2000) 1213–1235. https://doi.org/10.1016/S0301-5629(00)00287-8.

[71] S. Sjostrand, A. Widerstrom, A.R. Ahlgren, M. Cinthio, Design and fabrication of a conceptual arterial ultrasound phantom capable of exhibiting longitudinal wall movement, IEEE Trans. Ultrason. Ferroelectr. Freq. Control. 64 (2017) 11–18. https://doi.org/10.1109/TUFFC.2016.2597246.

[72] P. Papathanasopoulou, S. Zhao, U. Köhler, M.B. Robertson, Q. Long, P. Hoskins, X.Y. Xu, I. Marshall, MRI measurement of time-resolved wall shear stress vectors in a carotid bifurcation model, and comparison with CFD predictions, J. Magn. Reson. Imaging. 17 (2003) 153–162. https://doi.org/10.1002/jmri.10243.

[73] R.S. Reneman, T. Arts, A.P.G. Hoeks, Wall shear stress - An important determinant of endothelial cell function and structure - In the arterial system in vivo: Discrepancies with theory, J. Vasc. Res. 43 (2006) 251–269. https://doi.org/10.1159/000091648.

[74] Y. Karnam, Multiscale Fluid-Structure Interaction Models Development and Applications to the 3D Elements of a Human Cardiovascular System Multiscale Fluid-Structure Interaction Models, Kate Gleason College of Engineering Department; Rochester Institute of Technology Kate, 2019.

[75] M.H. Friedman, D.P. Giddens, Blood flow in major blood vessels - Modeling and experiments, Ann. Biomed. Eng. 33 (2005) 1710–1713. https://doi.org/10.1007/s10439-005-8773-1.

[76] B. Chayer, M. Hoven, Cardinal, Marie-Hèlène, L. Hongliang, R. Lopata, G. Cloutier, Atherosclerotic carotid bifurcation phantoms with stenotic soft inclusion for ultrasound flow and vessel wall elastography imaging, Phys. Med. Biol. 64 (2019) 95025.

[77] G. Goudot, J. Poree, O. Pedreira, L. Khider, P. Julia, J. Alsac, E. Laborie, T. Mirault, M. Tanter, E. Messas, M. Pernot, Wall Shear Stress Measurement by Ultrafast Vector Flow Imaging for Atherosclerotic Carotid Stenosis, Eur. Heart J. 40 (2019).

[78] L. Queijo, R. Lima, PDMS Anatomical Realistic Models for Hemodynamic Studies Using Rapid Prototyping Technology, in: Int. Fed. Med. Biol. Eng., Springer, Germany, 2010: pp. 434–437. https://doi.org/10.1007/978-3-642-14515-5.

[79] A. Souza, J. Ribeiro, R. Lima, Manufacturing process of a brain aneurysm biomodel in PDMS using rapid prototyping, in: Comput. Vis. Med. Image Process., Springer, Porto, 2019: pp. 671–676.

[80] S. Einav, H.J. Berman, R.L. Fuhro, P.R. DiGiovanni, S. Fine, J.D. Fridman, Measurement of velocity profiles of red blood cells in the microcirculation by laser Doppler anemometry (LDA), Biorheology. 12 (1975) 207–210. https://doi.org/10.3233/BIR-1975-123-411.

[81] E. Pinto, V. Faustino, R.O. Rodrigues, D. Pinho, V. Garcia, J.M. Miranda, R. Lima, A Rapid and Low-Cost Nonlithographic Method to Fabricate Biomedical Microdevices for Blood Flow Analysis, Micromachines. (2015) 121–135. https://doi.org/10.3390/mi6010121.

[82] F. Kabinejadian, D.N. Ghista, B. Su, M. Kaabi Nezhadian, L.P. Chua, J.H. Yeo, H.L. Leo, In vitro measurements of velocity and wall shear stress in a novel sequential anastomotic graft design model under pulsatile flow conditions, Med. Eng. Phys. 36 (2014) 1233–1245. https://doi.org/10.1016/j.medengphy.2014.06.024.

[83] R.L. Hewlin, J.P. Kizito, Development of an Experimental and Digital Cardiovascular Arterial Model for Transient Hemodynamic and Postural Change Studies: "A Preliminary Framework Analysis," Cardiovasc. Eng. Technol. 9 (2018). https://doi.org/10.1007/s13239-017-0332-z.

[84] S.M. Park, Y.U. Min, M.J. Kang, K.C. Kim, H.S. Ji, In vitro hemodynamic study on the stenotic right coronary artery using experimental and numerical analysis, J. Mech. Med. Biol. 10 (2010) 695–712. https://doi.org/10.1142/S0219519410003812.

[85] D.J. Ravnic, Y.Z. Zhang, A. Tsuda, J.P. Pratt, H.T. Huss, S.J. Mentzer, Multi-image particle tracking velocimetry of the microcirculation using fluorescent nanoparticles, Microvasc. Res. 72 (2006) 27–33. https://doi.org/10.1016/j.mvr.2006.04.006.

[86] M. Büsen, T.A.S. Kaufmann, M. Neidlin, U. Steinseifer, S.J. Sonntag, In vitro flow investigations in the aortic arch during cardiopulmonary bypass with stereo-PIV, J. Biomech. 48 (2015) 2005–2011. https://doi.org/10.1016/j.jbiomech.2015.03.030.

[87] M. Dusinska, E. Rundén-Pran, S.C. Carreira, M. Saunders, Critical Evaluation of Toxicity Tests, Advers. Eff. Eng. Nanomater. (2012) 63–83. https://doi.org/10.1016/B978-0-12-386940-1.00004-0.

[88] A. Rezvan, C.W. Ni, N. Alberts-Grill, H. Jo, Animal, in vitro, and ex vivo models of flow-dependent atherosclerosis: Role of oxidative stress, Antioxidants Redox Signal. 15 (2011) 1433–1448. https://doi.org/10.1089/ars.2010.3365.

[89] W. Santamore, P. Walinsky, A. Bove, R. Cox, R.A. Carey, J.F. Spann, The effects of vasoconstriction on experimental coronary artery stenosis, Am. Heart J. 100 (1980) 852–858.

[90] T. Fukui, H. Asama, M. Kimura, T. Itoi, K. Morinishi, Influence of Geometric Changes in the Thoracic Aorta due to Arterial Switch Operations on the Wall Shear Stress Distribution, Open Biomed. Eng. J. 11 (2017) 9–16. https://doi.org/10.2174/1874120701711010009.

[91] R. Agujetas, M.R. González-Fernández, J.M. Nogales-Asensio, J.M. Montanero, Numerical analysis of the pressure drop across highly-eccentric coronary stenoses: Application to the calculation of the fractional flow reserve, Biomed. Eng. Online. 17 (2018). https://doi.org/10.1186/s12938-018-0503-7.

[92] Y. Imai, T. Omori, Y. Shimogonya, T. Yamaguchi, T. Ishikawa, Numerical methods for simulating blood flow at macro, micro, and multi scales, J. Biomech. 49 (2016) 2221–2228. https://doi.org/10.1016/j.jbiomech.2015.11.047.

[93] B.B. Lieber, M. Siebes, T. Yamaguchi, Correlation of hemodynamic events with clinical and

pathological observations, Ann. Biomed. Eng. 33 (2005) 1695–1703. https://doi.org/10.1007/s10439-005-8760-6.

[94] G. Biglino, P. Verschueren, R. Zegels, A.M. Taylor, S. Schievano, Rapid prototyping compliant arterial phantoms for in-vitro studies and device testing, J. Cardiovasc. Magn. Reson. 15 (2013) 1–7. https://doi.org/10.1186/1532-429X-15-2.

[95] R. Jewkes, H.E. Burton, D.M. Espino, Towards additive manufacture of functional, spline-based morphometric models of healthy and diseased coronary arteries: In vitro proof-of-concept using a porcine template, J. Funct. Biomater. 9 (2018). https://doi.org/10.3390/jfb9010015.

[96] P.F. Costa, H.J. Albers, J.E.A. Linssen, H.H.T. Middelkamp, L. Van Der Hout, R. Passier, A. Van Den Berg, J. Malda, A.D. Van Der Meer, Mimicking arterial thrombosis in a 3D-printed microfluidic: In vitro vascular model based on computed tomography angiography data, Lab Chip. 17 (2017) 2785–2792. https://doi.org/10.1039/c7lc00202e.

[97] J.M. Zhang, L.P. Chua, D.N. Ghista, T.M. Zhou, Y.S. Tan, Validation of numerical simulation with PIV measurements for two anastomosis models, Med. Eng. Phys. 30 (2008) 226–247. https://doi.org/10.1016/j.medengphy.2007.02.004.

[98] M. Sayed Razavi, E. Shirani, Development of a general method for designing microvascular networks using distribution of wall shear stress, J. Biomech. 46 (2013) 2303–2309. https://doi.org/10.1016/j.jbiomech.2013.06.005.

[99] E. Doutel, J. Carneiro, M. Oliveira, Fabrication of 3D milis-scale channels for hemodynamic studies, J. Mech. Med. Biol. 12 (2015) 367–374.

[100] Y. Huo, M. Svendsen, J.S. Choy, Z.D. Zhang, G.S. Kassab, A validated predictive model of coronary fractional flow reserve, J. R. Soc. Interface. 9 (2012) 1325–1338. https://doi.org/10.1098/rsif.2011.0605.

[101] J. Robert, B. Weber, L. Frese, M.Y. Emmert, D. Schmidt, A. Von Eckardstein, L. Rohrer, S.P. Hoerstrup, A three-dimensional engineered artery model for in vitro atherosclerosis research, PLoS One. 8 (2013). https://doi.org/10.1371/journal.pone.0079821.

[102] S. Kefayati, T.L. Poepping, Transitional flow analysis in the carotid artery bifurcation by proper orthogonal decomposition and particle image velocimetry, Med. Eng. Phys. 35 (2013) 898–909. https://doi.org/10.1016/j.medengphy.2012.08.020.

[103] E. Doutel, J. Carneiro, J.B.L.M. Campos, J.M. Miranda, Experimental and numerical methodology to analyze flows in a coronary bifurcation, Eur. J. Mech. B/Fluids. 67 (2018) 341–356. https://doi.org/10.1016/j.euromechflu.2017.09.009.

[104] D. Pinho, D. Bento, J. Ribeiro, R. Lima, M. Vaz, An In Vitro Experimental Evaluation of the Displacement Field in an Intracranial Aneurysm Model, in: New Trends Mech. Mach. Sci., Springer, 2015: pp. 261–268.

[105] R.O. Rodrigues, D. Pinho, D. Bento, R. Lima, J. Ribeiro, Wall expansion assessment of an intracranial aneurysm model by a 3D Digital Image Correlation System, Measurement. 88 (2016) 262–270. https://doi.org/10.1016/j.measurement.2016.03.045.

[106] Y. Shimizu, A. Javadzadegan, T. Hayase, M. Ohta, Flow observations in elastic stenosis biomodel with comparison to rigid-like model, Technol. Heal. Care. 21 (2013) 305–314. https://doi.org/10.3233/THC-130725.

[107] R. Naryan, Rapid Prototyping of Biomaterials, 1st ed., Woodhead Publishing, Limited, 2014.

[108] D.M. Kalaskar, 3D Printing in Medicine, First, Elsevier, 2017.

[109] S.H. Huang, P. Liu, A. Mokasdar, L. Hou, Additive manufacturing and its societal impact: A literature review, Int. J. Adv. Manuf. Technol. 67 (2013) 1191–1203. https://doi.org/10.1007/s00170-012-4558-5.

[110] X. Wang, Q. Ao, X. Tian, J. Fan, Y. Wei, W. Hou, H. Tong, S. Bai, 3D bioprinting technologies for hard tissue and organ engineering, Materials. 9 (2016) 1–23. https://doi.org/10.3390/ma9100802.

[111] F.P.W. Melchels, J. Feijen, D.W. Grijpma, A review on stereolithography and its applications in biomedical engineering, Biomaterials. 31 (2010) 6121–6130. https://doi.org/10.1016/j.biomaterials.2010.04.050.

[112] C.L. Faria, D. Pinho, J. Santos, L.M. Gonçalves, Low cost 3D printed biomodels for biofluid mechanics applications, J. Mech. Eng. Biomech. 3 (2018) 1–7.

[113] L. Hütter, P.H. Geoghegan, P.D. Docherty, M.S. Lazarjan, D. Clucas, M. Jermy, Fabrication of a compliant phantom of the human aortic arch for use in Particle Image Velocimetry (PIV) experimentation, Curr. Dir. Biomed. Eng. 2 (2016) 493–497. https://doi.org/10.1515/cdbme-2016-0109.

[114] B.K. Gu, D.J. Choi, S.J. Park, M.S. Kim, C.M. Kang, C.H. Kim, 3-Dimensional Bioprinting for Tissue Engineering Applications, Biomater. Res. 20 (2016) 1–8. https://doi.org/10.1186/s40824-016-0058-2.

[115] K.I. Aycock, P. Hariharan, B.A. Craven, Particle image velocimetry measurements in an anatomical vascular model fabricated using inkjet 3D printing, Exp. Fluids. 58 (2017) 1–8. https://doi.org/10.1007/s00348-017-2403-1.

[116] J. Brunette, R. Mongrain, J.C. Tardif, A realistic coronary artery phantom for particle image velocimetry: Featuring injection-molded inclusions and multiple layers, J. Vis. 7 (2004) 241–248. https://doi.org/10.1007/BF03181639.

[117] D. Maragiannis, M.S. Jackson, S.R. Igo, R.C. Schutt, P. Connell, J. Grande-Allen, C.M. Barker, S.M. Chang, M.J. Reardon, W.A. Zoghbi, S.H. Little, Replicating Patient-Specific Severe Aortic Valve Stenosis with Functional 3D Modeling, Circ. Cardiovasc. Imaging. 8 (2015) 1–8. https://doi.org/10.1161/CIRCIMAGING.115.003626.

[118] K. Stepniak, A. Ursani, N. Paul, H. Naguib, Novel 3D printing technology for CT phantom coronary arteries with high geometrical accuracy for biomedical imaging applications, Bioprinting. 18 (2020) e00074. https://doi.org/10.1016/j.bprint.2020.e00074.

[119] A. Malone, D. Chari, S. Cournane, I. Naydenova, A. Fagan, J. Browne, Investigation of the assessment of low degree (<50%) renal artery stenosis based on velocity flow profile analysis using Doppler ultrasound: An in-vitro study, Phys. Medica. 65 (2019) 209–218. https://doi.org/10.1016/j.ejmp.2019.08.016.

[120] Y. Asaad, M. Epshtein, A. Yee, N. Korin, The Flow Dependent Adhesion of von Willebrand Factor (VWF)-A1 Functionalized Nanoparticles in an in Vitro Coronary Stenosis Model Yathreb, Molecules. (2019) 1–12.

[121] P.H. Geoghegan, N.A. Buchmann, C.J.T. Spence, S. Moore, M. Jermy, Fabrication of rigid and flexible refractive-index-matched flow phantoms for flow visualisation and optical flow measurements, Exp. Fluids. 52 (2012) 1331–1347. https://doi.org/10.1007/s00348-011-1258-0.

[122] G. Porenta, H. Baumgartner, H. Schima, W. Steffen, D. Moertl, P. Probst, G. Maurer, An in-vitro model of coronary artery stenosis: influence of stenosis morphology on velocity measurements, IEEE. (2002) 721–724. https://doi.org/10.1109/cic.1994.470084.

[123] A.E. Ensley, P. Lynch, Toward Designing the Optimal Total Cavopulmonary Connection : an In Vitro Study, Ann Thorac Surg. (1999). https://doi.org/10.1016/S0003-4975(99)00560-3.

[124] Z.L.. Helgeson, J. Jenkins, J. Abraham, E. Sparrow, Particle Trajectories and Agglomeration/Accumulation in Branching Arteries Subjected to Orbital Atherectom, Open Biomed. Eng. J. 5 (2011) 25–38. https://doi.org/10.2174/1874120701105010025.

[125] M. Siebes, C.S. Campbell, D.Z. D'argenio, Fluid dynamics of a partially collapsible stenosis in a flow model of the coronary circulation, J. Biomech. Eng. 118 (1996) 489–497. https://doi.org/10.1115/1.2796035.

[126] G. Porenta, H. Schima, A. Pentaris, Assessment of cornary stenoses by doppler wires: A validation study using in vitro modeling and computer simulations, Ultrasound Med. Biol. 25 (1999) 793–801.

[127] N. Benard, D. Coisne, E. Donal, R. Perrault, Experimental study of laminar blood flow through an artery treated by a stent implantation: Characterisation of intra-stent wall shear stress, J. Biomech. 36 (2003) 991–998. https://doi.org/10.1016/S0021-9290(03)00068-X.

[128] T.L. Poepping, H.N. Nikolov, R.N. Rankin, M. Lee, D.W. Holdsworth, An in vitro system for Doppler ultrasound flow studies in the stenosed carotid artery bifurcation, Ultrasound Med. Biol. 28 (2002) 495–506. https://doi.org/10.1016/S0301-5629(02)00479-9.

[129] A. Subramaniam, S. Sethuraman, Biomedical Applications of Nondegradable Polymers, Elsevier Inc., 2014. https://doi.org/10.1016/B978-0-12-396983-5.00019-3.

[130] J.M. Chan, K.H.K. Wong, A.M. Richards, C.L. Drum, Microengineering in cardiovascular research: New developments and translational applications, Cardiovasc. Res. 106 (2015) 9–18. https://doi.org/10.1093/cvr/cvv049.

[131] S. Halldorsson, E. Lucumi, R. Gómez-Sjöberg, R.M.T. Fleming, Advantages and challenges of microfluidic cell culture in polydimethylsiloxane devices, Biosens. Bioelectron. 63 (2015) 218–231. https://doi.org/10.1016/j.bios.2014.07.029.

[132] S. Kefayati, D.W. Holdsworth, T.L. Poepping, Turbulence intensity measurements using particle image velocimetry in diseased carotid artery models: Effect of stenosis severity, plaque eccentricity, and ulceration, J. Biomech. 47 (2014) 253–263. https://doi.org/10.1016/j.jbiomech.2013.09.007.

[133] S. Kefayati, J.S. Milner, D.W. Holdsworth, T.L. Poepping, In vitro shear stress measurements using particle image velocimetry in a family of carotid artery models: Effect of stenosis severity, plaque eccentricity, and ulceration, PLOS \ONE. 9 (2014). https://doi.org/10.1371/journal.pone.0098209.

[134] T.L. Poepping, R.N. Rankin, D.W. Holdsworth, Flow patterns in carotid bifurcation models using

pulsed doppler ultrasound: Effect of concentric vs. eccentric stenosis on turbulence and recirculation, Ultrasound Med. Biol. 36 (2010) 1125–1134. https://doi.org/10.1016/j.ultrasmedbio.2010.02.005.

[135] A.L. Dicarlo, T. Poepping, A.F. Set-up, Investigation of flow and turbulence in carotid artery models of varying compliance using particle image velocimetry, in: World Congr. Med. Phys. Biomed. Eng., Springer, 2015: pp. 1743–1744. https://doi.org/10.1007/978-3-319-19387-8.

[136] A.L. DiCarlo, D.W. Holdsworth, T.L. Poepping, Study of the effect of stenosis severity and non-Newtonian viscosity on multidirectional wall shear stress and flow disturbances in the carotid artery using particle image velocimetry, Med. Eng. Phys. 65 (2018) 8–23. https://doi.org/10.1016/j.medengphy.2018.12.023.

[137] M.D. Griffith, T. Leweke, M.C. Thompson, K. Hourigan, Pulsatile flow in stenotic geometries: Flow behaviour and stability, J. Fluid Mech. 622 (2009) 291–320. https://doi.org/10.1017/S0022112008005338.

[138] Y. Yang, X. Liu, Y. Xia, W. Wu, H. Xiong, H. Zhang, L. Xu, K.K.L. Wong, H. Ouyang, W. Huang, Impact of spatial characteristics in the left stenotic coronary artery on the hemodynamics and visualization of 3D replica models, Sci. Rep. 7 (2017) 1–13. https://doi.org/10.1038/s41598-017-15620-1.

[139] E. Westein, S. De Witt, M. Lamers, J.M.E.M. Cosemans, J.W.M. Heemskerk, Monitoring in vitro thrombus formation with novel microfluidic devices, Platelets. 23 (2012) 501–509. https://doi.org/10.3109/09537104.2012.709653.

[140] E. Westein, A.D. Van Der Meer, M.J.E. Kuijpers, J.P. Frimat, A. Van Den Berg, J.W.M. Heemskerk, Atherosclerotic geometries exacerbate pathological thrombus formation poststenosis in a von Willebrand factor-dependent manner, Proc. Natl. Acad. Sci. U. S. A. 110 (2013) 1357–1362. https://doi.org/10.1073/pnas.1209905110.

[141] Y. Zheng, J. Chen, M. Craven, N.W. Choi, S. Totorica, A. Diaz-Santana, P. Kermani, B. Hempstead, C. Fischbach-Teschl, J.A. López, A.D. Stroock, In vitro microvessels for the study of angiogenesis and thrombosis, Proc. Natl. Acad. Sci. U. S. A. 109 (2012) 9342–9347. https://doi.org/10.1073/pnas.1201240109.

[142] R.G. Mannino, D.R. Myers, B. Ahn, Y. Wang, Margo Rollins, H. Gole, A.S. Lin, R.E. Guldberg, D.P. Giddens, L.H. Timmins, W.A. Lam, Do-it-yourself in vitro vasculature that recapitulates in vivo geometries for investigating endothelial-blood cell interactions, Sci. Rep. 5 (2015) 1–12. https://doi.org/10.1038/srep12401.

[143] P.C. Sousa, F.T. Pinho, M.A. Alves, M.S.N. Oliveira, A review of hemorheology: Measuring techniques and recent advances, Korea Aust. Rheol. J. 28 (2016) 1–22. https://doi.org/10.1007/s13367-016-0001-z.

[144] O. Maruyama, T. Yamane, N. Tsunemoto, M. Nishida, T. Tsutsui, T. Jikuya, A preliminary study of microcapsule suspension for hemolysis evaluation of artificial organs, Artif. Organs. 23 (1999) 274–279. https://doi.org/10.1046/j.1525-1594.1999.06316.x.

[145] S. V. Jansen, I. Müller, M. Nachtsheim, T. Schmitz-Rode, U. Steinseifer, Ghost Cell Suspensions as Blood Analogue Fluid for Macroscopic Particle Image Velocimetry Measurements, Artif. Organs. 40 (2016) 207–212. https://doi.org/10.1111/aor.12511.

[146] J. Calejo, D. Pinho, F. Galindo-Rosales, R. Lima, L. Campo-Deaño, Particulate Blood Analogues Reproducing the Erythrocytes Cell-Free Layer in a Microfluidic Device Containing a Hyperbolic Contraction, Micromachines. 7 (2016) 4. https://doi.org/10.3390/mi7010004.

[147] B.N. Muñoz-Sánchez, S.F. Silva, D. Pinho, E.J. Vega, R. Lima, Generation of micro-sized PDMS particles by a flow focusing technique for biomicrofluidics applications, Biomicrofluidics. 10 (2016) 14122. https://doi.org/10.1063/1.4943007.

[148] C.F. Anes, D. Pinho, B.N. Muñoz-Sánchez, E.J. Vega, R. Lima, Shrinkage and colour in the production of micro-sized {PDMS} particles for microfluidic applications, J. Micromechanics Microengineering. 28 (2018) 75002. https://doi.org/10.1088/1361-6439/aab7b9.

[149] T.T. Nguyen, Y. Biadillah, R. Mongrain, J. Brunette, J.-C. Tardif, O.F. Bertrand, A Method for Matching the Refractive Index and Kinematic Viscosity of a Blood Analog for Flow Visualization in Hydraulic Cardiovascular Models, J. Biomech. Eng. 126 (2004) 529–535. https://doi.org/10.1115/1.1785812.

[150] J.D. Gray, I. Owen, M.P. Escudier, Dynamic scaling of unsteady shear-thinning non-Newtonian fluid flows in a large-scale model of a distal anastomosis, Exp. Fluids. 43 (2007) 535–546. https://doi.org/10.1007/s00348-007-0317-z.

[151] E. Akagawa, H. Lee, E. Tatsumi, A. Homma, T. Tsukiya, Y. Taenaka, Flow visualization for different port angles of a pulsatile ventricular assist device, J. Artif. Organs. 15 (2012) 119–127. https://doi.org/10.1007/s10047-011-0614-4.

[152] V. Deplano, Y. Knapp, L. Bailly, E. Bertrand, Flow of a blood analogue fluid in a compliant abdominal aortic aneurysm model: Experimental modelling, J. Biomech. 47 (2014) 1262–1269. https://doi.org/10.1016/j.jbiomech.2014.02.026.

[153] A.D. Anastasiou, A.S. Spyrogianni, K.C. Koskinas, G.D. Giannoglou, S. V. Paras, Experimental investigation of the flow of a blood analogue fluid in a replica of a bifurcated small artery, Med. Eng. Phys. 34 (2012) 211–218. https://doi.org/10.1016/j.medengphy.2011.07.012.

[154] F.J.H. Gijsen, E. Allanic, F.N. Van De Vosse, J.D. Janssen, The influence of the non-Newtonian properties of blood on the flow in large arteries: Unsteady flow in a 90°curved tube, J. Biomech. 32 (1999) 705–713. https://doi.org/10.1016/S0021-9290(99)00014-7.

[155] G. Vlastos, D. Lerche, B. Koch, The superposition of steady on oscillatory shear and its effect on the viscoelasticity of human blood and a blood-like model fluid, Biorheology. 34 (1997) 19–36. https://doi.org/10.1016/S0006-355X(97)00002-4.

[156] G. Vlastos, D. Lerche, B. Koch, O. Samba, M. Pohl, The effect of parallel combined steady and oscillatory shear flows on blood and polymer solutions, Rheol. Acta. 36 (1997) 160–172. https://doi.org/10.1007/BF00366822.

[157] D. Bento, C.S. Fernandes, J.M. Miranda, R. Lima, In vitro blood flow visualizations and cell-free layer (CFL) measurements in a microchannel network, Exp. Therm. Fluid Sci. 109 (2019) 109847. https://doi.org/10.1016/j.expthermflusci.2019.109847.

[158] H. Sun, M. Björnmalm, J. Cui, E.H.H. Wong, Y. Dai, Q. Dai, G.G. Qiao, F. Caruso, Structure Governs the Deformability of Polymer Particles in a Microfluidic Blood Capillary Model, ACS Macro Lett. 4 (2015) 1205–1209. https://doi.org/10.1021/acsmacrolett.5b00591.

[159] T.W. Secomb, A.R. Pries, Blood viscosity in microvessels: experiment and theory, Comptes Rendus

Phys. 14 (2013) 470–478. https://doi.org/10.1016/j.crhy.2013.04.002.

[160] R. Lima, T. Ishikawa, Y. Imai, T. Yamaguchi, Blood flow behavior in microchannels: Past, current and future trends, Single Two-Phase Flows Chem. Biomed. Eng. (2012) 513–547. https://doi.org/10.2174/978160805295011201010513.

[161] N. Maeda, Erythrocyte Rheology in Microcirculation., Jpn. J. Physiol. 46 (1996) 1–14. https://doi.org/10.2170/jjphysiol.46.1.

[162] S.O. Catarino, R.O. Rodrigues, D. Pinho, M. Miranda, G. Minas, R. Lima, Blood Cells Separation and Sorting Techniques of Passive Microfluidic Devices : From Fabrication to Applications, Micromachines. 10 (2019) 593.

[163] D. Pinho, R.O. Rodrigues, V. Faustino, T. Yaginuma, J. Exposto, R. Lima, Red blood cells radial dispersion in blood flowing through microchannels : The role of temperature, J. Biomech. 49 (2016) 2293–2298. https://doi.org/10.1016/j.jbiomech.2015.11.037.

[164] R. Lima, T. Ishikawa, Y. Imai, M. Takeda, S. Wada, T. Yamaguchi, Radial dispersion of red blood cells in blood flowing through glass capillaries: The role of hematocrit and geometry, J. Biomech. 41 (2008) 2188–2196. https://doi.org/10.1016/j.jbiomech.2008.04.033.

[165] R. Lima, T. Ishikawa, Y. Imai, M. Takeda, S. Wada, T. Yamaguchi, Measurement of individual red blood cell motions under high hematocrit conditions using a confocal micro-PTV system, Ann. Biomed. Eng. 37 (2009) 1546–1559. https://doi.org/10.1007/s10439-009-9732-z.

[166] N. Doshi, A.S. Zahr, S. Bhaskar, J. Lahann, S. Mitragotri, Red blood cell-mimicking synthetic biomaterial particles, Proc. Natl. Acad. Sci. U. S. A. 106 (2009) 21495–21499. https://doi.org/10.1073/pnas.0907127106.

[167] S. She, Q. Li, B. Shan, W. Tong, C. Gao, Fabrication of Red-Blood-Cell-Like Polyelectrolyte Microcapsules and Their Deformation and Recovery Behavior Through a Microcapillary, Adv. Mater. 25 (2013) 5814–5818. https://doi.org/10.1002/adma.201302875.

[168] X. Ju, X. Wang, Z. Liu, R. Xie, W. Wang, L. Chu, Red-blood-cell-shaped chitosan microparticles prepared by electrospraying, Particuology. 30 (2017) 151–157. https://doi.org/10.1016/j.partic.2016.05.011.

[169] D. Pinho, L. Campo-Deaño, R. Lima, F.T. Pinho, In vitro particulate analogue fluids for experimental studies of rheological and hemorheological behavior of glucose-rich RBC suspensions, Biomicrofluidics. 11 (2017) 54105. https://doi.org/10.1063/1.4998190.

[170] K. Chen, T.J. Merkel, A. Pandya, M.E. Napier, J.C. Luft, W. Daniel, S. Sheiko, J.M. DeSimone, Low modulus biomimetic microgel particles with high loading of hemoglobin, Biomacromolecules. 13 (2012) 2748–2759. https://doi.org/10.1021/bm3007242.

[171] J. Cui, M. Björnmalm, K. Liang, C. Xu, J.P. Best, X. Zhang, F. Caruso, Super-Soft Hydrogel Particles with Tunable Elasticity in a Microfluidic Blood Capillary Model, Adv. Mater. 26 (2014) 7295–7299. https://doi.org/10.1002/adma.201402753.

[172] A.C. Anselmo, M. Zhang, S. Kumar, D.R. Vogus, S. Menegatti, M.E. Helgeson, S. Mitragotri, Elasticity of nanoparticles influences their blood circulation, phagocytosis, endocytosis, and targeting, ACS Nano. 9 (2015) 3169–3177. https://doi.org/10.1021/acsnano.5b00147.

[173] L. Zhang, Z. Cao, Y. Li, J.-R. Ella-Menye, T. Bai, S. Jiang, Softer Zwitterionic Nanogels for Longer

Circulation and Lower Splenic Accumulation, ACS Nano. 6 (2012) 6681–6686. https://doi.org/10.1021/nn301159a.

[174] O. Maruyama, T. Yamane, M. Nishida, A. Aouidef, T. Tsutsui, T. Jikuya, T. Masuzawa, Fractural characteristic evaluation of a microcapsule suspension using a rotational shear stressor, ASAIO J. 48 (2002) 365–373. https://doi.org/10.1097/00002480-200207000-00007.

[175] T.T. Nguyen, R. Mongrain, S. Prakash, Development of a Blood Analog for the Hemodynamic Efficiency Evaluation of Cardiovascular Devices, in: Proc. Can. Des. Eng. Netw. Conf., Montreal, 2004: pp. 1–10.

[176] D.A.M. Carvalho, A.R.O. Rodrigues, V. Faustino, D. Pinho, E.M.S. Castanheira, R. Lima, Microfluidic deformability study of an innovative blood analogue fluid based on giant unilamellar vesicles, J. Funct. Biomater. 9 (2018) 1–11. https://doi.org/10.3390/jfb9040070.

[177] Y. Tamba, H. Terashima, M. Yamazaki, A membrane filtering method for the purification of giant unilamellar vesicles, Chem. Phys. Lipids. 164 (2011) 351–358. https://doi.org/10.1016/j.chemphyslip.2011.04.003.

[178] T.J. Merkel, S.W. Jones, K.P. Herlihy, F.R. Kersey, A.R. Shields, M.E. Napier, J.C. Luft, H. Wu, W.C. Zamboni, A.Z. Wang, J.E. Bear, J.M. DeSimone, Using mechanobiological mimicry of red blood cells to extend circulation times of hydrogel microparticles, Proc. Natl. Acad. Sci. U. S. A. 108 (2011) 586–591. https://doi.org/10.1073/pnas.1010013108.

[179] N. Vilanova, C. Rodríguez-Abreu, A. Fernández-Nieves, C. Solans, Fabrication of Novel Silicone Capsules with Tunable Mechanical Properties by Microfluidic Techniques, ACS Appl. Mater. Interfaces. 5 (2013) 5247–5252. https://doi.org/10.1021/am4010896.

[180] Y.H. Choi, K.H. Chung, H.B. Hong, W.S. Lee, Production of PDMS microparticles by emulsification of two phases and their potential biological application, Int. J. Polym. Mater. Polym. Biomater. 67 (2017) 686–692. https://doi.org/10.1080/00914037.2017.1375494.

[181] D. Pinho, B.N. Muñoz-Sánchez, C.F. Anes, E.J. Vega, R. Lima, Flexible PDMS microparticles to mimic RBCs in blood particulate analogue fluids, Mech. Res. Commun. 100 (2019) 18–20. https://doi.org/10.1016/j.mechrescom.2019.103399.

[182] S. Peltola, D. Grijpam, A review of rapid prototyping techniques for tissue engineering purposes, Ann. Med. 40 (2008) 268–280. https://doi.org/10.1080/07853890701881788.

[183] B. Micó-Vicent, E. Perales, K. Huraibat, F. Martínez-Verdú, V. Viqueira, Maximization of FDM-3D-objects gonio-appearance effects using PLA and ABS filaments and combining several printing parameters: "A case study," Materials. 12 (2019) 1423. https://doi.org/10.3390/ma12091423.

[184] S. Singh, C. Prakash, S. Ramakrishna, 3D printing of polyether-ether-ketone for biomedical applications, Eur. Polym. J. 114 (2019) 234–248. https://doi.org/10.1016/j.eurpolymj.2019.02.035.

[185] L. Jyothish Kumar, P.M. Pandey, D.I. Wimpenny, 3D printing and additive manufacturing technologies, Springer, 2019. https://doi.org/10.1007/978-981-13-0305-0.

[186] M. Maniruzzaman, 3D and 4D Printing in Biomedical Applications, First, Wiley, 2019.

[187] D.G. Tamay, T.D. Usal, A.S. Alagoz, D. Yucel, N. Hasirci, V. Hasirci, 3D and 4D printing of polymers

for tissue engineering applications, Front. Bioeng. Biotechnol. 7 (2019) 164. https://doi.org/10.3389/fbioe.2019.00164.

[188] E. Enno, S. Fachhochschule, Fabrication of FDM 3D objects with ABS and PLA and determination of their mechanical properties, RTejournal. 2014 (2014) 1–9. https://www.rtejournal.de/ausgabe11/3872.

[189] M. Lay, N.L.N. Thajudin, Z.A.A. Hamid, A. Rusli, M.K. Abdullah, R.K. Shuib, Comparison of physical and mechanical properties of PLA, ABS and nylon 6 fabricated using fused deposition modeling and injection molding, Compos. Part B Eng. 176 (2019) 107341. https://doi.org/10.1016/j.compositesb.2019.107341.

[190] P.R. Martinez, A. Goyanes, A.W. Basit, S. Gaisford, Fabrication of drug-loaded hydrogels with stereolithographic 3D printing, Int. J. Pharm. 532 (2017) 313–317. https://doi.org/10.1016/j.ijpharm.2017.09.003.

[191] O. Abouelatta, 3D Surface Roughness Measurement Using a Light Sectioning Vision System, in: Proc. World Congr. Eng., London, 2014.

[192] B. Bhushan, The Nature of Surfaces, in: Mod. Tribol. Handb., CRC Press, 2001.

[193] O. Maruyama, Y. Numata, M. Nishida, D.T. Yamane, I. Oshima, D.Y. Adachi, Hemolysis caused by surface roughness under shear flow, Japanese Soc. Artif. Organs. (2005) 228–236. https://doi.org/10.1007/s10047-005-0316-x.

[194] S. Manuel, O. Tavares, Analysis of surface roughness and models of mechanical contacts, University of Porto, 2005.

[195] OLYMPUS, Introduction to Surface Roughness Measurement, (2018).

[196] L. Campo-Deaño, R.P.A. Dullens, D.G.A.L. Aarts, F.T. Pinho, M.S.N. Oliveira, Viscoelasticity of blood and viscoelastic blood analogues for use in polydymethylsiloxane in vitro models of the circulatory system, Biomicrofluidics. 7 (2013) 1–11. https://doi.org/10.1063/1.4804649.

[197] S. AV, 3D Manufacturing of Intracranial aneurysm biomodels for flow visualizations: a low cost fabrication process, J. Mech. Behav. Biomed. Mater. (2020).

[198] M. Versluis, High-speed imaging in fluids, Exp Fluids. 54 (2013) 1458. https://doi.org/10.1007/s00348-013-1458-x.

[199] J. Honour, A brief history of principles used in high speed cameras, IMAG H2. 57 (2009) 303–317. https://doi.org/10.1179/136821909X12490307953035.

[200] M.D. Abràmoff, P.J. Magalhães, S.J. Ram, Image processing with imageJ, Biophotonics Int. 11 (2004) 36–41. https://doi.org/10.1201/9781420005615.ax4.

[201] E. Meijering, O. Dzyubachyk, I. Smal, Methods for cell and particle tracking, in: Methods Enzymol., 1st ed., Elsevier Inc., 2012: pp. 183–200. https://doi.org/10.1016/B978-0-12-391857-4.00009-4.

[202] Y. Feng, J. Goree, B. Liu, Errors in particle tracking velocimetry with high-speed cameras, Rev. Sci. Instrum. 82 (2011). https://doi.org/10.1063/1.3589267.

[203] G. Kissas, Y. Yang, E. Hwuang, W.R. Witschey, J.A. Detre, P. Perdikaris, Machine learning in cardiovascular flows modeling: Predicting arterial blood pressure from non-invasive 4D flow MRI

data using physics-informed neural networks, Comput. Methods Appl. Mech. Eng. 358 (2020) 112623. https://doi.org/10.1016/j.cma.2019.112623.

[204] J. Lee, Y. Fung, Flow in Locally Constricted Tubes At Low Reynolds Numbers, J. Appl. Mech. 37 (1970) 9–16.

[205] D.N. Ku, D.P. Giddens, C.K. Zarins, S. Glagov, Pulsatile flow and atherosclerosis in the human carotid bifurcation. Positive correlation between plaque location and low and oscillating shear stress, Arterioscler. Thromb. Vasc. Biol. 5 (1985) 293–302. https://doi.org/10.1161/01.atv.5.3.293.

[206] S. Glagov, C.K. Zarins, D.P. Giddens, D.N. Ku, Mechanical Factors in the Pathogenesis, Localization and Evolution of Atherosclerotic Plaques, Dis. Arter. Wall. (1989) 217–239. https://doi.org/10.1007/978-1-4471-1464-2_15.

[207] S. Sriyab, Mathematical analysis of non-Newtonian blood flow in stenosis narrow arteries, Comput. Math. Methods Med. 2014 (2014) 479152. https://doi.org/10.1155/2014/479152.

[208] C.X. Chen, Y. Ding, J.A. Gear, Numerical simulation of atherosclerotic plaque growth using two-way fluid-structural interaction, ANZIAM J. 53 (2012) 277. https://doi.org/10.21914/anziamj.v53i0.5668.

[209] A. Razavi, E. Shirani, M.R. Sadeghi, Numerical simulation of blood pulsatile flow in a stenosed carotid artery using different rheological models, J. Biomech. 44 (2011) 2021–2030. https://doi.org/10.1016/j.jbiomech.2011.04.023.

[210] J. Wu, G. Liu, W. Huang, D.N. Ghista, K.K.L. Wong, Transient blood flow in elastic coronary arteries with varying degrees of stenosis and dilatations: CFD modelling and parametric study, Comput. Methods Biomech. Biomed. Engin. 18 (2015) 1835–1845. https://doi.org/10.1080/10255842.2014.976812.

[211] S.K. Shanmugavelayudam, D.A. Rubenstein, W. Yin, Effect of geometrical assumptions on numerical modeling of coronary blood flow under normal and disease conditions, J. Biomech. Eng. 132 (2010) 1–8. https://doi.org/10.1115/1.4001033.

[212] T. Chaichana, Z. Sun, J. Jewkes, Hemodynamic impacts of various types of stenosis inthe left coronary artery bifurcation: A patient-specific analysis, Phys. Medica. 29 (2013) 447–452. https://doi.org/10.1016/j.ejmp.2013.02.001.

[213] M. Dabagh, W. Takabe, P. Jalali, S. White, H. Jo, Hemodynamic features in stenosed coronary arteries: CFD analysis based on histological images, J. Appl. Math. 2013 (2013) 11. https://doi.org/10.1155/2013/715407.

[214] J.M. Zhang, L. Zhong, T. Luo, Y. Huo, S.Y. Tan, A.S.L. Wong, B. Su, M. Wan, X. Zhao, G.S. Kassab, H.P. Lee, B.C. Khoo, C.W. Kang, T. Ba, R.S. Tan, Numerical simulation and clinical implications of stenosis in coronary blood flow, Biomed Res. Int. 2014 (2014). https://doi.org/10.1155/2014/514729.

[215] M. Biglarian, M. Momeni, H. Hassanzadeh, A. Moshfegh, D. Toghraie, A. Javadzadegan, S. Rostami, Computational investigation of stenosis in curvature of coronary artery within both dynamic and static models, Comput. Methods Programs Biomed. 185 (2019) 105170. https://doi.org/10.1016/j.cmpb.2019.105170.

[216] A. Mahalingam, U.U. Gawandalkar, G. Kini, A. Buradi, T. Araki, N. Ikeda, A. Nicolaides, J.R. Laird,

L. Saba, J.S. Suri, Numerical analysis of the effect of turbulence transition on the hemodynamic parameters in human coronary arteries, Cardiovasc. Diagnosis Ther. 6 (2016) 208–220. https://doi.org/10.21037/cdt.2016.03.08.

[217] X. Torii, Ryo and Wood, Nigel; Hadjiloizou, Nearchos; Dowsey, Andrew; Wright, Andrew; Hughes, Alun;Davies, Justin; Francis, Darrel; Mayet, Jamil; Yang, Guang;Thom, Simon; Xu, Fluid–structure interaction analysis of a patient-specific right coronary artery with physiological velocity and pressure waveforms, Commun. Numer. Methods Eng. 25 (2009) 565–580. https://doi.org/10.1002/cnm.

[218] P.K. Siogkas, M.I. Papafaklis, A.I. Sakellarios, K.A. Stefanou, C. V. Bourantas, L.S. Athanasiou, T.P. Exarchos, K.K. Naka, L.K. Michalis, O. Parodi, D.I. Fotiadis, Patient-specific simulation of coronary artery pressure measurements: An in vivo three-dimensional validation study in humans, Biomed Res. Int. 2015 (2014) 628416. https://doi.org/10.1155/2015/628416.

[219] F. Moukalled, L. Mangani, The Finite Volume Method in Computational Fluid Dynamics, An Advanced Introduction with OpenFOAM and Matlab, First, Springer, 2016.

[220] W. Versteeg, H K ; Malalasekera, An Introduction to Computational Fluid Dynamics, The finite volume method, Second, Prentice Hall, 2007.

[221] C.A.J. Fletcher, Computational Techniques for Fluid Dynamics. Volume 1, Second, Springer, 1991. https://doi.org/10.1016/0010-4655(84)90059-6.

[222] M. Schäfer, Computational Engineering – Introduction to Numerical Methods, First, Springer, 2006.

[223] B.K. Lee, Computational fluid dynamics in cardiovascular disease, Korean Circ. J. 41 (2011) 423–430. https://doi.org/10.4070/kcj.2011.41.8.423.

[224] J.H. Ferziger, M. Peric, Computational Methods for Fluid Dynamics, Third, Springer, 2002. https://doi.org/10.1017/CBO9781107415324.004.

[225] J. Banks, Turbulence Modeling in Three-Dimensional Stenosed Arterial Bifurcations, J. Biomech. Eng. 129 (2007) 40–50. https://doi.org/10.1115/1.2401182.

[226] A.G. Straatman, J. Ryval, Two-equation Turbulence Modeling of Pulsatile Flow in a, J. Biomech. Eng. 126 (2016) 625–635. https://doi.org/10.1115/1.1798055.

[227] S. George, Paul-Louis; Frey, Mesh generation, Wiley, 2008.

[228] F.-F. Zhou, Coronary Artery Diameter is Inversely Associated with the Severity of Coronary Lesions in Patients Undergoing Coronary Angiography, Cell. Physiol. Biochem. 43 (2017) 1247–1257. https://doi.org/10.1159/000481765.

[229] J.A. Ambrose, S.L. Winters, A. Stern, A. Eng, L.E. Teichholz, R. Gorlin, V. Fuster, Angiographic morphology and the pathogenesis of unstable angina pectoris, J. Am. Coll. Cardiol. 5 (1985) 609–616. https://doi.org/10.1016/S0735-1097(85)80384-3.

[230] M.G. Rabby, A. Razzak, M. Molla, Pulsatile non-Newtonian blood flow through a model of arterial stenosis, Procedia Eng. 56 (2013) 225–231. https://doi.org/10.1016/j.proeng.2013.03.111.

[231] A. Buradi, A. Mahalingam, Effect of stenosis severity on wall shear stress based hemodynamic descriptors using multiphase mixture theory, J. Appl. Fluid Mech. 11 (2018) 1497–1509. https://doi.org/10.29252/jafm.11.06.29062.

[232] M.X. Li, J.J. Beech-Brandt, L.R. John, Numerical analysis of pulsatile blood flow and vessel wall mechanics in different degrees of stenoses, J. Biomech. 40 (2007) 3715–3724. https://doi.org/10.1016/j.jbiomech.2007.06.023.

[233] H. Mohammadi, F. Bahramian, Boundary conditions in simulation of stenosed coronary arteries, Cardiovasc. Eng. 9 (2009) 83–91. https://doi.org/10.1007/s10558-009-9078-z.

[234] D. Zipes, P. Libby, M. Tomaselli, Braunwald's heart disease: A textbook of cardiovascular medicine., Eleventh, Elsevier, 2018.

[235] J. Milde, R. Hrušecký, R. Zaujec, L. Morovic, A. Görög, Research of ABS and PLA materials in the process of fused deposition modeling method, Ann. DAAAM Proc. Int. DAAAM Symp. 114 (2017) 812–820. https://doi.org/10.2507/28th.daaam.proceedings.114.

[236] R.V.N. Santosh, J. Sarojini, K.A. Vikram, V.V.K. Lakshmi, Evaluating the Mechanical Properties of Commonly Used 3d Printed ABS and PLA Polymers with Multi Layered Polymers, Int. J. Eng. Adv. Technol. 8 (2019) 2351–2356. https://doi.org/10.35940/ijeat.f8646.088619.

[237] Ultimaker, Cura 15.4 - Instructions, (2017).

[238] P.H. Geoghegan, M.C. Jermy, D.S. Nobes, A PIV comparison of the flow field and wall shear stress in rigid and compliant models of healthy carotid arteries, J. Mech. Med. Biol. 17 (2017) 1–16. https://doi.org/10.1142/S0219519417500415.

[239] D. Bento, R.O. Rodrigues, V. Faustino, D. Pinho, C.S. Fernandes, A.I. Pereira, V. Garcia, M. Miranda, Deformation of Red Blood Cells , Air Bubbles , and Droplets in Microfluidic Devices : Flow Visualizations and Measurements, Micromachines. 9 (2018). https://doi.org/10.3390/mi9040151.

[240] K. Wang, C.C. Ho, C. Zhang, B. Wang, A Review on the 3D Printing of Functional Structures for Medical Phantoms and Regenerated Tissue and Organ Applications, Engineering. 3 (2017) 653–662. https://doi.org/10.1016/J.ENG.2017.05.013.

[241] S.S.M. Lai, B.Y.S. Yiu, A.K.K. Poon, A.C.H. Yu, Design of anthropomorphic flow phantoms based on rapid prototyping of compliant vessel geometries, Ultrasound Med. Biol. 39 (2013) 1654–1664. https://doi.org/10.1016/j.ultrasmedbio.2013.03.015.

[242] A. Srivani, M.A. Xavior, Investigation of Surface Texture Using Image Processing Techniques, Procedia Eng. 97 (2014) 1943–1947. https://doi.org/10.1016/j.proeng.2014.12.348.

[243] D.F. Young, Effect of a time-dependent stenosis on flow through a tube, J. Manuf. Sci. Eng. Trans. ASME. 90 (1968) 248–254. https://doi.org/10.1115/1.3604621.

[244] K. Pielhop, M. Klaas, W. Schröder, Analysis of the unsteady flow in an elastic stenotic vessel, Eur. J. Mech. B/Fluids. 35 (2012) 102–110. https://doi.org/10.1016/j.euromechflu.2012.01.010.

[245] E. Silva, S. Teixeira, P. Lobarinhas, Computational Fluid Dynamics Simulations: an Approach to Evaluate Cardiovascular Dysfunction, in: G.R. Rey, L.M. Muneta (Eds.), Model. Simul. Optim., IntechOpen, Rijeka, 2010: pp. 26–46. https://doi.org/10.5772/7680.

[246] C.W. Tsao, Polymer microfluidics: Simple, low-cost fabrication process bridging academic lab research to commercialized production, Micromachines. 7 (2016). https://doi.org/10.3390/mi7120225.

[247] H. Liu, H. Zhou, H. Lan, T. Liu, X. Liu, H. Yu, 3D printing of artificial blood vessel: study on multi-

parameter optimization design for vascular molding effect in alginate and gelatin, Micromachines. 8 (2017) 1–10. https://doi.org/10.3390/mi8080237.

[248] R. Lima, S. Wada, S. Tanaka, M. Takeda, T. Ishikawa, K.I. Tsubota, Y. Imai, T. Yamaguchi, In vitro blood flow in a rectangular PDMS microchannel: Experimental observations using a confocal micro-PIV system, Biomed. Microdevices. 10 (2008) 153–167. https://doi.org/10.1007/s10544-007-9121-z.

[249] P.C. Sousa, J. Carneiro, R. Vaz, A. Cerejo, F.T. Pinho, M.A. Alves, Shear viscosity and nonlinear behavior of whole blood under large amplitude oscillatory shear, Biorheology. 50 (2013) 269–282. https://doi.org/10.3233/BIR-130643.

[250] M. Brust, C. Schaefer, Rheology of Human Blood Plasma : Viscoelastic Versus Newtonian Behavior, Phys. Rev. Lett. 078305 (2013) 6–10. https://doi.org/10.1103/PhysRevLett.110.078305.

[251] L. Tonietto, L. Gonzaga Jr., New Method for Evaluating Surface Roughness Parameters Acquired by Laser Scanning, Sci. Rep. 9 (2019) 1–16. https://doi.org/10.1038/s41598-019-51545-7.

[252] M.S. Alsoufi, A.E. Elsayed, Surface Roughness Quality and Dimensional Accuracy—A Comprehensive Analysis of 100% Infill Printed Parts Fabricated by a Personal/Desktop Cost-Effective FDM 3D Printer, Mater. Sci. Appl. 09 (2018) 11–40. https://doi.org/10.4236/msa.2018.91002.

[253] T. Yamaguchi, T. Ishikawa, K. Tsubota, Y. Imai, M. Nakamura, T. Fukui, Computational Blood Flow Analysis —New Trends and Methods, J. Biomech. Sci. Eng. 1 (2006) 29–50. https://doi.org/10.1299/jbse.1.29.

[254] S.H. Frankel, S. Varghese, Numerical Modeling of Pulsatile Turbulent Flow in Stenotic, J. Biomech. Eng. 125 (2003) 445–460. https://doi.org/10.1115/1.1589774.

[255] R. Tabe, F. Ghalichi, S. Hossainpour, K. Ghasemzadeh, Laminar-to-turbulence and relaminarization zones detection by simulation of low Reynolds number turbulent blood flow in large stenosed arteries, Biomed. Mater. Eng. 27 (2016) 119–129. https://doi.org/10.3233/BME-161574.

[256] S.A. Ahmed, D.P. Giddens, Pulsatile poststenotic flow studies with laser Doppler anemometry, J. Biomech. 17 (1984) 695–705. https://doi.org/10.1016/0021-9290(84)90123-4.

Appendix A

Manufacturing Process of the Stenotic Coronary Models in PDMS

The procedure used to manufacture the biomodel to perform *in vitro* studies is explained in this appendix. After obtained the 3D printed models, they were and cast in PDMS by a soft-lithography technique. Once obtained the printed physical models, it was prepared PDMS, a silicon-based organic polymer (Sylgard® 184), with a ratio of 10:1, where, 10 grams of the base polymer corresponds to 1 gram of its curing agent (Dow Corning Canada, Inc.). For this purpose, a balance to weigh precisely the amounts of material required was used and both were mixed with the aid of a spatula, until the mixture was homogenized. After performing the mixture, it appeared air bubbles, so a vacuum pump was used to remove them and subsequently the liquid was poured into the mold. Thereafter, the curing process was performed placing the models in an incubator varying its temperature between 38°C and 40°C. After this process, the 3D printed stenotic coronary arteries were removed from the mold, with alcohol help. In the end, were obtained the final PDMS biomodels for the experimental tests as illustrated in Figure 67.

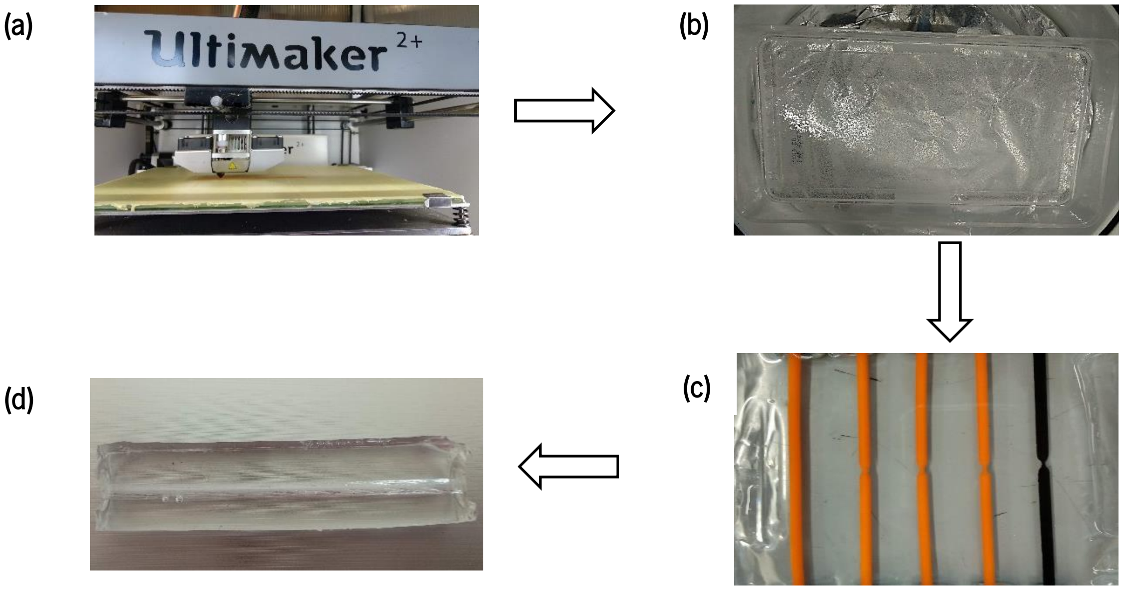

Figure 67. Main steps of the biomodels fabrication procedure: (a) fabrication of the biomodels by means of 3D printing; (b) preparation of the PDMS; (c) pouring the polymer PDMS over the printed biomodels; (d) remove the printed biomodels of the cured PDMS.

Appendix B

List of Publications

From the development of this dissertation, the following papers have resulted in international peer-reviewed journals, papers in international conference proceedings, and poster presentations.

Articles in international journals

Carvalho, V.,Rodrigues, N., Ribeiro,R., Costa, P., Teixeira, S., Lima, R., 2020. 3D Printed Biomodels for Flow Visualization in Stenotic Vessels: An Experimental and Numerical study. Micromachines Journal, under review.

Carvalho, V. et al. , 2020. *In vitro* stenotic arteries to perform blood analogues flow visualizations and measurements: a Review. Paper in The Open Biomedical Engineering Journal, under review.

Papers in proceedings of international conferences

Carvalho, V., Ribeiro,R., Costa, P., Teixeira, S., Lima, R., 2020. Hemodynamic studies in coronary artery models manufactured by 3D printing, International Conference Innovation in Engineering (ICIE), 2021, Guimarães, Portugal.

Carvalho, V., Rodrigues, N., Lima, R., Teixeira, S., 2020. Numerical simulation of blood pulsatile flow in stenotic coronary arteries: The effect of turbulence modeling and non-Newtonian assumptions, International Conference on Applied Mathematics and Computer Science (ICAMCS), 2020, Athens, Greece.

Poster presentations (Best poster award)

Carvalho, V.,Rodrigues, N., Ribeiro,R., Costa, P., Teixeira, S., Lima, R., 2020. 3D Printed Biomodels for Flow Visualization in Stenotic Vessels: An Experimental and Numerical study. In National Meeting of Biomedical Engineers (ENEEB), Aveiro, Portugal.